EM Simulations of Large Platforms with Antennas: RCS, Antenna Placement, and Radiation Hazard

by

İhsan Ozan YILDIRIM

A Thesis Submitted to the
Graduate School of Engineering
in Partial Fulfillment of the Requirements for
the Degree of

Master of Science

in

Electrical & Electronics Engineering

Koç University

January, 2013

Koç University

Graduate School of Sciences and Engineering

This is to certify that I have examined this copy of a master's thesis by

İhsan Ozan YILDIRIM

and have found that it is complete and satisfactory in all respects,
and that any and all revisions required by the final
examining committee have been made.

Committee Members:

Prof. Dr. M. İrşadi AKSUN (Advisor)

Assoc. Prof. Dr. Alper Tunga ERDOĞAN

Dr. İbrahim TÜRER

Date: _____

To my grandfather

Abstract

The main purpose of this work is to study and investigate the electromagnetic properties of large platforms with and without antennas. Radar cross section (RCS), antenna patterns, mutual coupling and radiation hazard are the topics of interest. In this work, the concept of Radar Cross Section is studied by analyzing several canonical geometries and two vessels. Followed by this initial study, RCS simulations of a tank as a large platform, for a frequency range involving radar frequency bands up to Ka band have been performed by using the implementation of the Physical Optics (PO) Method by FEKO (A commercial software by EM Software & Systems-S.A. Ltd. (EMSS-SA).). Moreover, some approaches to reduce RCS of large platforms have been investigated and applied to the tank. After RCS analysis, a linear antenna has been modeled with simulation software EMSS-SA FEKO, ANSYS Inc. HFSS, and Computer Simulation Technology AG. MICROWAVE STUDIO. The antenna model has been analyzed with Method of Moments (MoM), Multilevel Fast Multipole Method (MLFMM), and Finite Integration Technique (FIT) for antenna parameters. A placement scenario on a large platform for a pair of the antenna of interest has been offered. Lastly, a large platform with antennas has been investigated for Hazards of Electromagnetic Radiation to Personnel (HERP).

Keywords: RCS, Physical Optics, Method of Moments, Multilevel Fast Multipole Method, Antennas on Large Platforms, Mutual Coupling, Radiation Hazard, HERP

ÖZETÇE

Çalışmanın ana amacı, büyük platformların (antenlerle ve antenler olmadan) elektromanyetik özelliklerinin incelenmesidir. Radar kesit alanı (RKA), anten örüntüleri, karşılıklı kuplaj ve radyasyon riski ilgilenilen konu başlıklarıdır. Bu çalışmada Radar Kesit Alanı konsepti çeşitli kanonik geometriler ve iki gemi analiz edilerek çalışılmıştır. Bu öncül çalışmanın ardından, büyük bir platform örneği olarak bir tankın RKA simulasyonları, FEKO'nun (EM Software & Systems-S.A. Ltd. (EMSS-SA) şirketinin ticari yazilimidir.) Fiziksel Optik (PO) Yöntemi implementasyonu kullanılarak, Ka bandına kadarki radar frekans bantlarında yapılmıştır. Buna ek olarak büyük platformlarda RKA düşürmek için bazı yaklaşımlar incelenmiş ve tanka uygulanmıştır. RKA analizi sonrasında, bir lineer anten EMSS-SA FEKO, ANSYS Inc. HFSS ve Computer Simulation Technology AG. MICROWAVE STUDIO yazılımları kullanılarak modellenmiştir. Anten modeli Moment Metodu (MoM), Çok Katmanlı Hızlı Çok Kutup Yöntemi (MLFMM) ve Sonlu İntegrasyon Tekniği (FIT) kullanılarak anten parametreleri için analiz edilmiştir. İncelenen antenin iki adeti için bir büyük platform üstüne yerleşim senaryosu önerilmiştir. Son olarak, üzerinde antenler olan bir büyük platform , Elektromanyetik Radyasyonun Personele Etkisi (HERP) için incelenmiştir.

Anahtar Kelimeler: RKA, Fiziksel Optik, Moment Metodu, Çok Katmanlı Hızlı Çok Kutup Yöntemi, Anten, Karşılıklı Kuplaj, Radyasyon Riski, HERP

Acknowledgments

Foremost, I would like to express my sincere gratitude to my advisor Dr. M. İrşadi Aksun for the continuous support of my M.Sc. study and research, for his patience, incredible motivation, enthusiasm, and immense knowledge. During my thesis study, he shared his valuable experience and provided me a perfect work environment, flawless advise and inspiration.

Besides my advisor, I would like to thank the rest of my thesis committee: Dr. Alper Tunga Erdoğan and Dr. İbrahim Türer for their encouragement, sincere interest, and insightful comments.

I would like to thank RMK Marine and OTOKAR AŞ for providing me to work at Altay Project and supporting me. I would like to thank Pertev Cinalioğlu who is the Vice President and Dilara Bağdat who was a Senior RF Systems Engineer at RMK Marine. I would like to thank Murat Uysal who is the Manager of EMI/EMC Section and Celal Akmehmet who is an EMI/EMC Engineer at OTOKAR AŞ.

I would send my deepest gratitude to my parents for their endless trust and support throughout my life. I would like to thank my grandfather for teaching me to be a honest person that I hope I am.

My thanks also go to my colleagues and friends Dr. Pınar Karabulut, Gökçen Mahmutoğlu, Seda Ünal, Umay Kayaalp, Onur Korbek, İbrahim Şahin, Philipp Heck, Erkan Yaldız and Demet Kara for their valuable support.

Last but not the least, I heartedly wish to thank Sinem Genç for making me a hopeful person who clings to life strongly.

Table of Contents

List of Tables

List of Figures

Nomenclature

CAD	Computer Aided Design
FIT	Finite Integration Technique
HERP	Hazards of Electromagnetic Radiation to Personnel
MLFMM	Multilevel Fast Multipole Method
MoM	Method of Moments
MPE	Maximum Permissible Exposure
PEC	Perfect Electric Conductor
PO	Physical Optics
RADAR	Radio Detection and Ranging
RADHAZ	Radiation Hazard
RCS	Radar Cross Section
RCWS	Remote Control Weapon System
RF	Radio Frequency
OTH	Over the Horizon
UHF	Ultra High Frequency
VHF	Very High Frequency

Chapter 1

Introduction

Modern land and shipboard platforms are usually equipped with many antennas for a wide variety of communication, detection, tracking, and surveillance purposes; ranging from simple Over the Horizon Radar (OTH) ($3 - 45MHz$) antennas through complex radar and high-frequency antennas (such as milimeter-wave cameras operating at $94GHz$), whose performances are quite critical for the success of the mission of the platform. However, the limited space available on the vehicle/ship leads to challenges for optimal antenna placement, as placing these antennas on such a complex platform usually results in distortion in their radiation patterns and mutual coupling. Note that, to elucidate the adverse effects of these problems, the distortion in the radiation patterns may reduce the desired coverage for effective communications and compromise accuracy of isolating and locating targets, while mutual coupling, caused by space waves, surface waves, and scattering by the platform, reduces the electromagnetic isolation between the antennas and consequently makes it difficult to operate the antennas simultaneously. Therefore, it is important to develop accurate numerical prediction tools to characterize the radiation patterns and mutual coupling of the antennas mounted on complex large platforms, in order for the performance of these antennas be optimized to reduce antenna coupling and interference, pattern

distortion of high frequency antennas due to shielding by adjacent structures, and Near-fields from radiation hazard (personnel, fuel, explosives).

Since antenna manufacturers normally test their products as stand alone units and provide the data accordingly, it is usually inadequate for applications that involve large metal platforms, on which the antenna induces currents and part of the vehicle becomes part of the effective antenna. As a result, there can be significant changes in antenna pattern performance that may prevent coverage in several directions. In addition, due to stringent requirements and specifications of the military systems, the antennas usually operate over a wide frequency range allowing multiple Radio Frequency (RF) systems to use the same antenna. Given the high complexity of the environment, strict specifications on the radiation performances of the antennas, and conflicting requirements of the other instruments and structures on the platform, the problem of reducing unwanted coupling, interference and distortions in the radiation patterns of the antennas is quite complex and may not be possible to achieve simultaneously. Hence, it leads to a natural question of how one can design such a complex system with satisfactory performance and repeatable design procedure. There are mainly two approaches to tackle for such a complex problem:

- a rigorous approach - developing a custom made simulator that would answer all of the above questions;

- a practical approach - using currently available commercial simulators on a cluster environment, with additional codes to fix some issues that may not be resolved by the available simulators.

The former approach would be more appealing for academics but less practical and possibly would take longer to complete, the later would be more practical, take less time to develop, but could require hands-on experience with the simulators and may require new fixes and modifications for every new geometry, structure and antenna. For this work, it would be more appropriate to start with the latter approach and get acquainted with currently the most popular EM based simulators, EMSS-SA FEKO,

Ansoft HFSS, and CST MICROWAVE STUDIO (MWS). Then, depending upon the geometry and requirements of the system, a hybrid approach may be developed, combining the versatility of commercial software with the flexibility of in-house codes.

1.1. Study Description

The aim of this study was to develop an efficient, accurate and practical framework for the combined analysis of antennas and platform, which requires incorporation of interferences due to multiple antennas and metal platform into the analysis, optimization of the location of antennas and judicious choice of antennas. Although it seems to be quite involved, considering our rather practical approach as briefly stated above, the main engines of the project has been the three commercial software, EMSS-SA FEKO, Ansoft HFSS, and CST MWS. As a result, the first phase of the project was dedicated to learning and using them in workstation and in a cluster environment for some canonical problems of interest. Meanwhile, all possible antenna types that are widely used in military and civilian land/ shipboard platforms were studied, initially employing the coarse models of the platforms, as examplified in Figure 1.1. Once the background information had been gathered, it was be followed by the analysis of more advanced structures including more realistic platform models, antenna couplings and near-field effects.

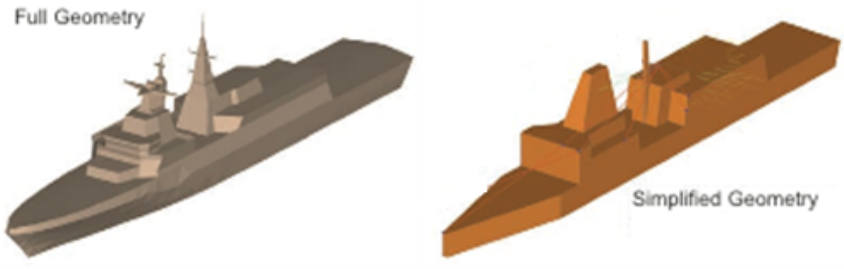

Figure 1.1: An example real platform and its simplified version from [3].

The following brief outline of the work would provide a good overview of this study:

Simulation Software and Training

- Acquiring suitable EM-based simulators (HFSS, FEKO, and CST MWS) and getting them installed on workstations and cluster environment: This is an important step to learn the software and its pros and cons on different platforms. Note that the software has to have suitable import capability in order for the platform models of varying complexities, which are to be generated by other software, be utilized seamlessly.

- Learning and training period for the software: During this phase, the details of how to use the software effectively were discussed, and the learning experience were shared as applied to different antennas with and without platforms.

- Modeling platforms and antennas: Real platforms and all possible antennas that could be employed on the platforms of interest were modelled and made ready to be analyzed by the simulators separately and together.

Radar Cross Section Analyses (Chapter 2) The radar cross section (RCS) of a target is an angle and frequency dependent measure of its scattering behavior, and therefore, for how properly the object is detectable with a radar operating at a certain frequency. RCS is of main interest in military applications, and is an important parameter, for target recognition. Especially for complex large platforms made out of metal parts mostly, the RCS behavior and its minimization are of great practical importance. Therefore, the analyses in this chapter cover the following steps:

- Generating proper models for the RCS calculations of canonical objects and platforms. Note that some complex platforms of interest require different models depending on the operation frequencies, (Sections 2.4 and 2.5.1).

- Verifying accuracy of the simulation software via comparing the obtained results with already known results from literature. This step requires determining the most suitable method that provides reliable results in reasonable simulation times, (Sections 2.3, 2.4, and 2.6).

- Calculation the RCS of the generated models and the assessment of the results. This step requires comparing the RCS behaviors with similar canonical objects or platforms, and determining the parts that cause excessive reflections, (Sections 2.5.2 and 2.6).

- Optimization of the platform for the RCS reduction, and determining the possible approaches to reduce the RCS, such as modification on the geometry and coating with radar absorber materials, (Section 2.7).

Antenna Analyses (Chapter 3) An antenna system operates on a quite complex platform, made out of metal in most part. In addition, over the last decades, there has been a tremendous increase of wireless on-board units independently whether the vehicle is supposed to be for civilian or military use. Consequently, there can be easily somewhere over a hundred different antennas distributed across a whole platform. In order to guarantee their intended performances, all possible antennas to be used on the platform are analyzed over the frequency band of interest. The analysis includes the radiation patterns of the antennas in free-space and on the realistic platform, and diagnoses of potential interference problems that might lead to a compromise in expected performance. Here are the steps:

- Analysis of antennas in free-space over the frequency band of interest: Since it is important to assess the influence of a platform or other antenna systems on the radiation patterns, gains, directivities and input impedances of an antenna, its performance in free-space sets the standard working performance, and helps to diagnose the adverse effects of the environment, (Sections 3.3.1 and 3.3.4).

- Analysis of antennas on a realistic platform over the frequency band of interest: Once the standard performances of the antennas have been compiled, their characteristics, such as radiation pattern, gain, directivity etc., need to be investigated on the real platform and under real operating conditions, (Sections 3.3.1, 3.3.2, and 3.3.4).

- Computation and assessment of antenna couplings and interference: Since the general trend is to build integrated and centralized antenna systems, with possibly broadband radiating elements for spread spectrum applications, coupling effects have to be carefully considered and analyzed beforehand. Once the necessary information on the radiation characteristics of the antennas, both standalone and together with the other antennas and platform, are gathered, the source of interference and couplings are determined with a view to gain valuable knowledge that would help optimize antenna locations. Note that there can be significant changes in antenna pattern performance caused by the platform resulting in undesirable nulls that prevent coverage in several directions, (Sections 3.3.2 and 3.3.3).

Antenna Placement Upon collecting all possible information about the field strengths (near- and far-fields) due to both the individual antennas and the combination of antennas over all platform, they have to be compiled and used for the optimization of the locations of all antennas employed on the platform. This is a rather difficult task as it definitely involves some sort of trade-offs that may not be resolved by a quantitative reasoning, (Section 3.3.5).

Radiation Hazard Analyses (Chapter 4) Radiation Hazard (RADHAZ) describes the hazards of electromagnetic radiation to fuels (HERF), electronic hardware and ordnance (HERO), and personnel (HERP). During the design of spatially restricted civilian or military platforms, a delicate balance must be observed between maintaining operational specifications and ensuring that RF and microwave systems comply

with the restrictions of the EM radiation level. In many instances, especially in military applications, sensitive communication systems and armaments must function reliably next to high-power radar and electronic warfare antennas, while maintaining strict safety standards regarding personnel, equipment, fuel, etc. Since these platforms are usually electrically large and represent very large and complex electromagnetic systems at RF frequencies, assessment of radiation hazard is quite complex and difficult. Therefore, it is important to explore some of the specific techniques and methods most applicable to RF radiation hazard analysis, and to demonstrate their capabilities by application to realistic problems. There are mainly two steps during this phase of the study:

- Antenna Near-Field Calculations: It is possible to consider all interaction between mounted antennas and the entire platform in great detail by calculating all near- and far-field strengths over the model of the operational environment, (Section 4.1).

- Diagnosis: Once all the necessary field strengths and visual aides are compiled accurately, they have to be analyzed according to the accepted standards, which could be set by the civilian or military authorities. Of course, such an analysis has to be coupled with the diagnosis of the possible problems and their possible remedies, including the re-placement optimization of some of the antennas, (Section 4.1.2).

Chapter 2

Radar Cross Section Analyses

2.1. The Nature of Radar

Radar is an electromagnetic system for the detection and location of objects [10]. A basic radar system works by transmitting a certain type of waveform, detects the reflected wave, interpret the echoed signal to try to determine the location and the type of possible objects in sight. Radars are not replacement instruments for human eye. More than this, basically, radars are used to see what human eye can not see or sense. For instance, because radar waves suffer much less attenuation through the atmosphere than light waves, and signals in the lower frequency ranges actually propagate over the visible horizon, it is possible to detect targets long before they are visible optically.

The acronym '*Radar*' is a contraction of the words '*Radio Detection and Ranging*'. An elementary radar system contains a transmitting antenna with a signal generator, and a receiving antenna with a signal detector. Some fragment of the transmitted signal is intercepted by a reflecting object, and is re-radiated in all directions. The reflected wave in a particular direction (same direction for mono-static radars and a different particular direction for bi-static radars) is the main concern for the radar. The receiving antenna intercepts the reflected wave and the signal detector process it

to detect an object and calculates the location and the relative velocity of the object. [10] Also as a result of emitting its own energy (a train of narrow, rectangular-shape pulses modulating a sine wave carrier as an example) a radar does not rely on the illumination of the target by other sources.

The distance of the object from the radar is calculated using the time T_R taken for the travel of the signal to the object and back. The radar uses the known velocity of propagation of an electromagnetic wave $c \cong 3 \times 10^8 m/s$ to determine the distance to the target. With these informations, one can easily calculate the distance R to the target

$$R = \frac{cT_R}{2} \tag{2.1}$$

with the factor 2 in the denominator because of the two-way propagation of radar.

Once the transmitted pulse emitted by the radar, a sufficient length of time must elapse to allow any echo signals to return and be detected before the next pulse may be transmitted. Therefore, the rate which pulses may be transmitted is determined by the largest range at which targets are expected. If the pulse repetition frequency is too high, echo signals from some targets might arrive after transmission of the next pulse, and ambiguities in measuring range might result. The maximum unambiguous range depending on the pulse repetition frequency f_p is

$$R_{unamb} = \frac{c}{2f_p} \tag{2.2}$$

The shift in the carrier frequency of the reflected wave can be used to distinguish the state of object, if it is moving or static. Also some other properties of object of interest can be determined with radars (like shape, color etc.) But in this study our main concern is to understand the detectability level of some specific objects.

If we define a radar as a device that transmits an electromagnetic wave and detects objects by virtue of the energy scattered from them in the direction of the receiver, one may say that a radar can operate in any frequency. In practice there are several limitations from availability of components to international regulations on frequency

spectrum. Common radars operate at frequencies from $3MHz$ to $300GHz$. The standard radar frequency bands and nomenclature by IEEE [1] can be seen in Table 2.1.

Table 2.1: Standard Radar-Frequency Letter-Band Nomenclature from IEEE Standard Radar Definitions [1]

Band Designation	Frequency Range
HF	$3 - 30MHz$
VHF	$30 - 300MHz$
UHF	$300 - 1000MHz$
L	$1000 - 2000MHz$
S	$2000 - 4000MHz$
C	$4000 - 8000MHz$
X	$8000 - 12000MHz$
K_u	$12 - 18GHz$
K	$18 - 27GHz$
K_a	$27 - 40GHz$
mm	$40 - 300GHz$

2.2. The Radar Equation

In this section, to provide a basis to the radar cross section calculations, the simple form of the radar equation will be derived assuming the reader is familiar with basic antenna parameters. The radar equation colligates target, environment, and characteristics of radar components.

Assuming the radar antenna is directive, let we denote power of the transmitter P_t. The power density (W/m^2) at a distance R from a directive antenna is

$$\frac{P_t G(\theta, \phi)}{4\pi R^2} \tag{2.3}$$

where $G(\theta, \phi)$ is the realized gain of the antenna in direction of interest. As expected, the target intercepts a portion of the incident power and re-radiates it in various directions. The measure of the amount of incident power intercepted by the target and re-radiated back in the direction of the radar is denoted as the radar cross section (σ) [10], and is defined using the power received by the radar P_r

$$P_r = \frac{P_t G(\theta, \phi)}{4\pi R^2} \frac{\sigma}{4\pi R^2} A_e \tag{2.4}$$

where A_e is the effective area of the receiving antenna. If we denote the minimum detectable signal as S_{min}, we can calculate the maximum range of a radar R_{max}

$$R_{max} = \sqrt[4]{\frac{P_t G(\theta, \phi) A_e \sigma}{(4\pi)^2 S_{min}}} \tag{2.5}$$

The Equation (2.5) is also known as the fundamental form of the radar equation.

2.3. Radar Cross Section of Targets and Physical Optics Method

The radar cross section (RCS) of any object is an angle and frequency dependent measure of its scattering behavior for electromagnetic waves and thus for how well the objects is detectable with radar from a certain direction at a certain frequency [11].

As it was mentioned before, the radar cross section σ is the property of a scattering object, or target, that is included in the radar equation to represent the magnitude of the echo signal returned to the radar by the target. In the derivation of the simple form of the radar equation in Section 2.2 the radar cross section was defined in terms of Equation 2.4. A definition of the radar cross section found in some texts on electromagnetic scattering is

$$\sigma = \lim_{R\to\infty} 4\pi R^2 \frac{|E^s|^2}{|E^i|^2} \tag{2.6}$$

where E^i stands for the incident electromagnetic field and E^s stands for the scattered field at the distance R. In realistic experimental setups. the requirement that the distance of the scatterer from the receiver R approaches infinity can never be fully accomplished [11]. Therefore, for practical work, Equation 2.6 is reduced to

$$\sigma = 4\pi R^2 \frac{|E^s|^2}{|E^i|^2} \tag{2.7}$$

There are several numerical methods to calculate RCS of objects such as Geometrical Optics (GO), Physical Optics (PO), the Uniform Theory of Diffraction, Finite-Difference Time-Domain (FDTD) etc. In this study Physical Optics Method will be used for RCS calculations of large platforms. In Figure 2.1 the reference coordinate system and angles used throughout this study can be found.

Physical Optics provides an analytic tool for the calculation of RCS for a variety of targets and circumstances. It is an improvement over the well-known simple geometric optics treatment of ray tracing, and provides many standard expressions for the RCS of simple shapes. It combines an expression for electromagnetic fields in terms of surface integrals, with a simplifying assumption for the surface fields. The fields, and thus RCS, at any point in space are expressed in terms of an integral over the surface of the reflecting target [12]. Further information about Physical Optics Theory of RCS and the mathematical development of it can be found in [13].

2.4. Canonical Setups for Radar Cross Section Simulations

In ongoing sections, in order to verify the integrity of the simulation software FEKO -which will be used for the simulations on big platforms- and obtain some know-how information several publications have been investigated. From Section 2.4.1 to

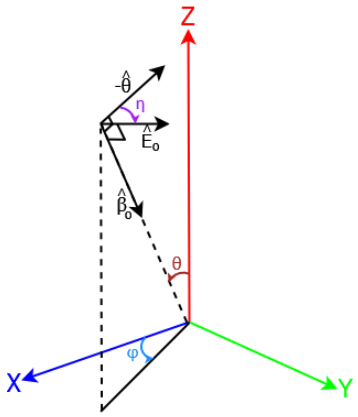

Figure 2.1: The Reference Coordinate System and Angles used throughout this study.

Section 2.4.5 six different canonical geometries have been reconstructed using FEKO's CAD interface CADFEKO and expecting same results from the publications CITE radar cross section simulations using FEKO's solver have been done. In Sections 2.4.6 and 2.4.7 similar simulations for a vessel and a cargo freighter have been done to examine the problems possible to be encountered when working with larger and more complex geometries on FEKO.

For the first six canonical geometries Method of Moment (which is also FEKO's default method for RCS calculations) has been used in simulations. But for ships it has been seen that MoM became too slow and needed too much computational resources than available and PO Method has been used in these simulations and the rest of radar cross section simulations.

In all of these simulations both for small canonical geometries and big ones like ships FEKO's integrity in RCS calculations have been verified comparing the results for both of the methods used. Also, coherence of the MoM and PO methods is investigated and verified in Section 2.4.1

2.4.1. A Perfect Electric Conductor Flat Plate

In this section, publication [4] has been reviewed and RCS simulations of a $10cmx10cm$ perfect electric conductor plate lying along the x-z plane have been done for three different cases. The first one is the bistatic RCS with normal illumination case at a single operating frequency and in the second case illumination is shifted 30° with respect to y-axis. And the last case is the monostatic version of the first case in a frequency range between $1 - 16GHz$. Besides the simulations, for the first case the analytical solution is derived and results from the analytical solution and from FEKO are compared.

Case 1: Bistatic RCS of the Plate with Normal Illumination

In this first case a square, $10cm \times 10cm$ perfect electric conductor plate with illumination at normal direction will be analyzed. Firstly, analytical solution for a rectangular plate will be introduced,values of bistatic RCS in normal incidence case will be calculated. After simulations, results from FEKO and analytical solution will be compared. Solution and simulation parameters can be seen in table 2.2, and the model created using CADFEKO with illumination direction in Figure 2.4.1

Table 2.2: Bistatic Radar Cross Section Solution and Simulation Parameters for Analytical Solution and FEKO Simulation of a Normally Illuminated $10cm \times 10cm$ PEC Plate

Parameter	Values
Operating Frequency	$6GHz$
Wavelength	$5cm$
Edge Length of Plate	$2\lambda = 10cm$
Excitation	$\theta = 90°, \phi = 90°$
Triangle Edge Length [1]	$\lambda/16$
Calculations	$\theta = 90°, \phi = 0° : 2° : 360°$

The triangle edge length in Table 2.2 which is the value provided to FEKO is not the certain value for all the triangles of the mesh, FEKO meshes the geometry using values around given one.

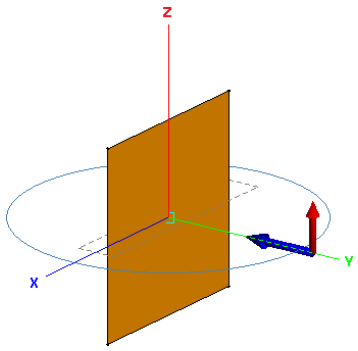

Figure 2.2: Case: 1, A Normally Illuminated $10cm \times 10cm$ PEC plate model created using CADFEKO, the blue and red arrows represents propagation and electric field vectors respectively. The surrounding circle represents the observation angles.

Analytical Solution Analytical solution with Physical Optics method for bistatic radar cross section of a rectangular flat plate illuminated normally (from [12])is

$$\sigma = 4\pi \frac{A^2}{\lambda^2} \left| \frac{\sin k(l/2)\cos\phi}{k(l/2)\cos\phi} \right|^2 \tag{2.8}$$

where A, k, l, and ϕ are area of the rectangular flat plate, wavenumber, length of the rectangular flat plat, and the observation angle with respect to $-x$ axis, respectively. It is also stated in [12] that for $\phi \ll 1$ or $\cos\phi \simeq 1$, Equation 2.8 reduces to

$$\sigma = 4\pi \frac{A^2}{\lambda^2} \left| sin\phi \frac{\sin kl\cos\phi}{kl\cos\phi} \right|^2 \tag{2.9}$$

In Figure 2.4.1 $2D$ illustration of the rectangular flat plate indicating the observation angle and axes can be seen.

[1]Detailed information about non-uniform meshing can be found in Section 2.5.2.

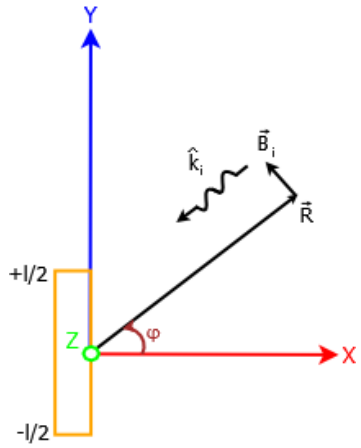

Figure 2.3: Case: 1, Illustration of the the rectangular flat plate indicating the observation angle and axes.

Results In Figures 2.4 and 2.5 the angular bistatic radar cross section patterns from [4] and same patterns obtained using analytical solution and FEKO's solver can be seen respectively.

As it can be seen in figures, patterns from different solvers and analytical solution overlap perfectly. These results verify the integrity of analytical solution using PO Method for simple shapes and more importantly FEKO's solver.

Case 2: Illumination with Angle to the Plate

In this second case, the same geometry and settings from the first case with a different illumination angle will be analyzed. For this case illumination is shifted 30° with respect to y-axis, see Figure 2.6. Considering that the reflector plate is perfect electric conductor, one can expect to observe the highest RCS values at the supplementary angle of the shift angle of the illumination. The similar solution parameters with the first case can be seen in Table 2.3.

Results In Figures 2.7 and 2.8 the angular bistatic radar cross section patterns from the publication [4] and obtained using FEKO's solver can be seen respectively.

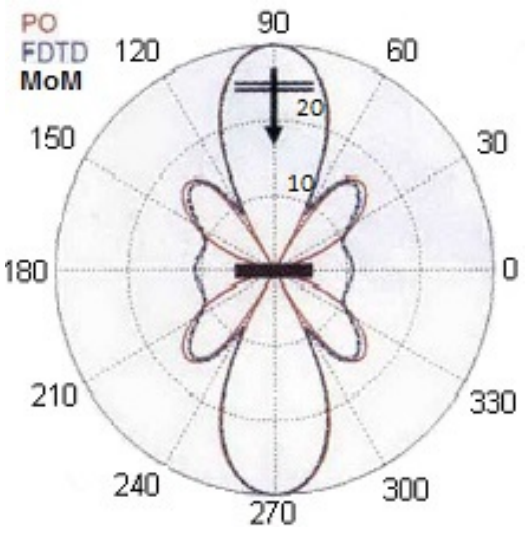

Figure 2.4: The angular bistatic RCS pattern of a $10cm \times 10cm$ PEC plate with normal illumination at $6GHz$ operating frequency from[4]. Values are normalized to $30dB$.

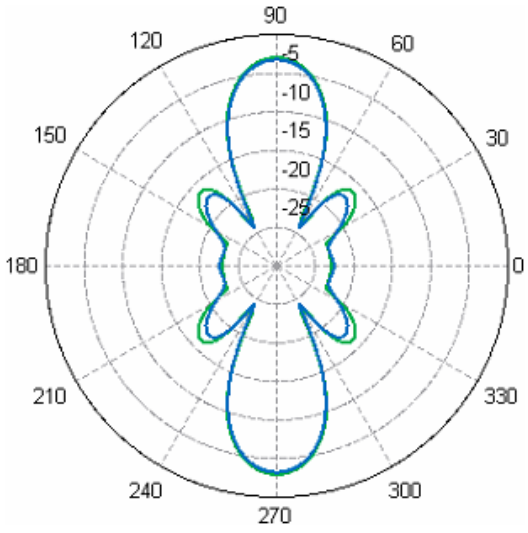

Figure 2.5: The angular bistatic RCS pattern of a $10cm \times 10cm$ PEC plate with normal illumination at $6GHz$ operating frequency obtained using analytical PO solution and FEKO's solver with PO Method. Blue and green lines represent results from FEKO's PO implementation and analytical PO solution, respectively

Table 2.3: Bistatic Radar Cross Section Simulation Parameters for FEKO Simulation of an Obliquely Illuminated $10cm \times 10cm$ PEC Plate

Parameter	Values
Operating Frequency	$6GHz$
Wavelength	$5cm$
Edge Length of Plate	$2\lambda = 10cm$
Excitation	$\theta = 90°, \phi = 60°$
Triangle Edge Length	$\lambda/16$
Calculations	$\theta = 90°, \phi = 0° : 2° : 360°$

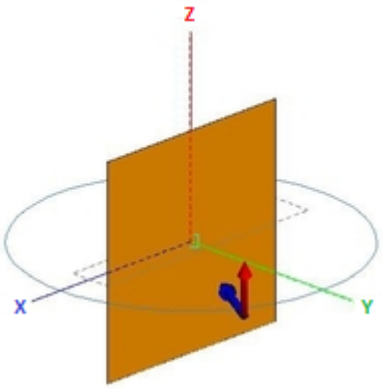

Figure 2.6: Case: 2, A Obliquely Illuminated $10cm \times 10cm$ PEC plate model created using CADFEKO, the blue and red arrows represents propagation and electric field vectors respectively. The surrounding circle represents the observation angles.

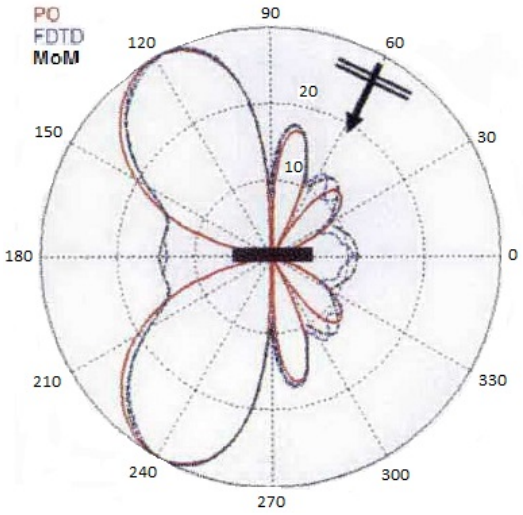

Figure 2.7: The angular bistatic RCS pattern of a $10cm \times 10cm$ PEC plate with oblique illumination at $6GHz$ operating frequency from[4]. Values are normalized to $30dB$.

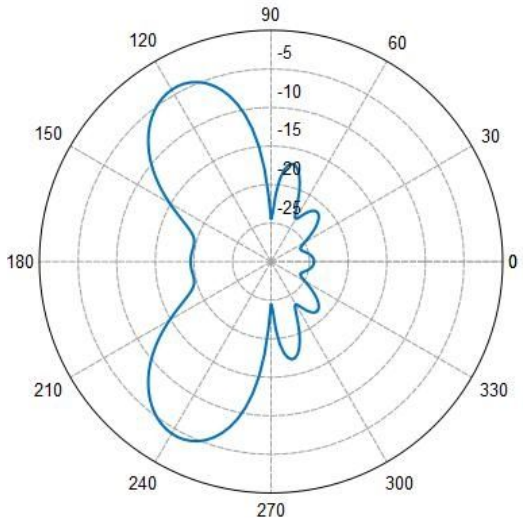

Figure 2.8: The angular bistatic RCS pattern of a $10cm \times 10cm$ PEC plate with oblique illumination at $6GHz$ operating frequency obtained using FEKO's solver.

As expected the biggest lobe corresponding the highest RCS values have been obtained at 120° with respect to y-axis. Besides verifying the integrity of FEKO's solver, these results provide practical information about the relation between the illumination and the radar cross section behavior of flat plates.

Case 3: RCS as a Function of Frequency

The third case of interest is the monostatic version of the first one (normally illuminated) in a frequency range from 1 to $16GHz$. For this case it can easily expected to observe a curve with increasing fashion with frequency considering the analytical solution from Section 2.4.1 and Equation 2.8. It is important to note that the bistatic RCS at $\theta = 0$ is identical to monostatic RCS at this observation angle and RCS values inversely proportional with wavelength or obviously proportional with frequency. The solution parameters similar to the ones in first two cases can be seen in Table 2.4.

Table 2.4: Monostatic Radar Cross Section Parameters for FEKO Simulation of a Normally Illuminated $10cm \times 10cm$ PEC Plate

Parameter	Values
Operating Frequency	$1to16GHz$
Edge Length of Plate	$2\lambda = 10cm$
Excitation	$\theta = 90°, \phi = 90°$
Triangle Edge Length	$\lambda/16$
Calculations	$\theta = 90°, \phi = 90°$

Results In Figures 2.9 and 2.10 the monostatic radar cross section curves from [4] and obtained using FEKO's solver can be seen respectively.

As it was mentioned and verified with the simulation results before, for a normally illuminated flat plate the higher frequencies result higher radar cross section values. These results also verify the integrity of FEKO's solver once again and provide prac-

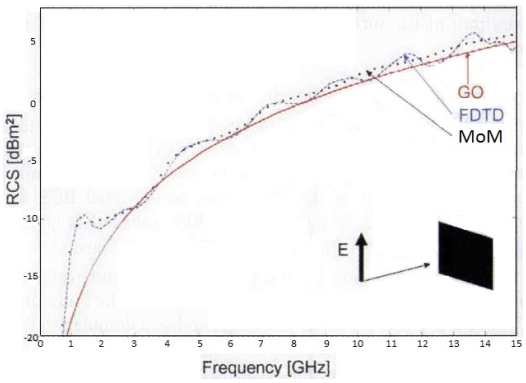

Figure 2.9: A plot of the monostatic RCS of a Normally Illuminated $10cm \times 10cm$ PEC Plate as a function of frequency from[4].

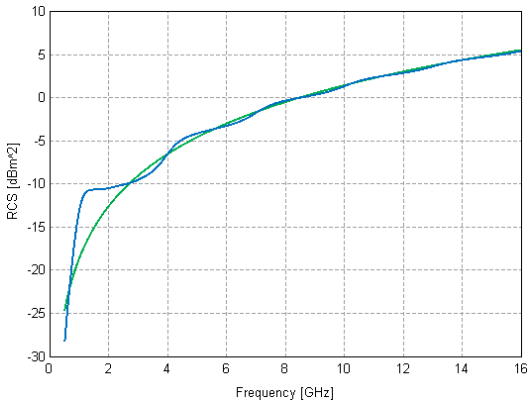

Figure 2.10: A plot of the monostatic RCS of a Normally Illuminated $10cm \times 10cm$ PEC Plate as a function of frequency obtained using FEKO's solver. Green and Blue lines represent Physical Optis Method and Method of Moments, respectively.

tical information about the relation between the operation frequency and the radar cross section behavior of flat plates.

Conclusion

A square, perfectly electric conductor plate was investigated in this section for its radar cross section behavior. Even thought a square, perfectly electric conductor plate is the most basic geometry for the radar cross section analysis, understanding its behavior, in different simulation scenarios, provides fundamental know-how about radar cross section analysis. The first two cases explain the effects of changes in the illumination to RCS and the last case states the proportional nature of frequency and radar cross section. And lastly, the concurrency of results from [4] and FEKO yields the integrity and reliability of using FEKO for radar cross sections simulations with both Method of Moments and Physical Optics Method.

2.4.2. A Thin Dielectric Sheet

In this section a $2m \times 1m$ rectangular electrically thin dielectric plate lying on $x-y$ plane illuminated from an oblique direction will be analyzed for its bistatic radar cross section behavior. The plate has $d = 0.004m$ of thickness, $\epsilon_r = 7$ of relative permittivity and, $\tan\delta = 0.03$ of loss tangent. The purpose of repeating this canonical example from [14] is to compare its results with a perfect electric conductor in same size for which the radar cross section behavior is predictable from Section 2.4.1. It is also predictable to obtain lower RCS values than perfect electric conductor plate considering using a lossy dielectric sheet.

More information about simulation parameters can be found in Table 2.5 and the model showing the direction and polarization of illumination can be seen in Figure 2.11.

Table 2.5: Bistatic Radar Cross Section Parameters for FEKO Simulations of an Obliquely Illuminated $2m \times 1m$ Electrically Thin Dielectric Sheet.

Parameter	Values
Operating Frequency	$100MHz$
Wavelength in Dielectric Sheet	$\lambda \cong 1.13m$
Sheet Thickness	$0.004m$
Length of Sheet	$2m$
Width of Sheet	$1m$
Relative Permittivity of Dielectric Material	$\epsilon_r = 7$
Loss Tangent of Dielectric Material	$tan\delta = 0.03$
Excitation Angles	$\theta = 20°, \phi = 50°$
Polarization Angle[2]	$\eta = 60°$
Triangle Edge Length	$\lambda/8$
Calculations	$\theta = -180° : 1° : 180°, \phi = 0°$

Model created using CADFEKO with illumination direction and observation angle can be seen in Figure 2.11.

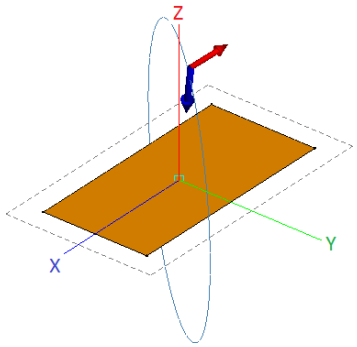

Figure 2.11: An Obliquely Illuminated $2m \times 1m$ Dielectric Sheet Model created using CADFEKO, the blue and red arrows represent propagation and electric field vectors respectively. The surrounding circle represents the observation angles.

Results As it was expected from physical interpretation or the definition of RCS 2.6, RCS values of dielectric sheet is lower than RCS values of PEC plate, see Figures 2.12 and 2.13. But in both cases the highest values are observed at $\theta = -20°$ and $\phi = 50°$ angles as these are the angles that excessive reflection occurs.

Conclusion A rectangular, dielectric sheet has been investigated in this section in terms of its radar cross section behavior with comparing its behavior with a perfect electric conductor of same size. The radar cross section behavior of a dielectric sheet will be a subject of interest in Section 2.7.2 when coating big objects with dielectric materials for radar cross section optimization.

[2]Polarization angle η represents the shift of the electric field vector from $-\widehat{\theta}$ direction. See Figure 2.1.

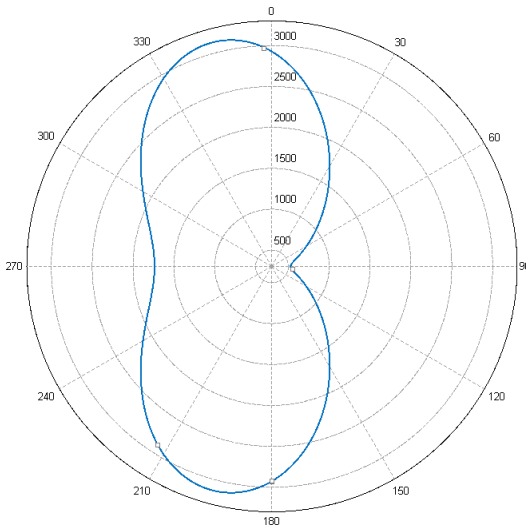

Figure 2.12: The angular bistatic RCS pattern of a $2m \times 1m$ dielectric sheet (at $\phi = 50°$ and θ is the independent axis) with obliquely illuminated from $\theta = 20°$, $\phi = 50°$ and $\eta = 60°$ at $100MHz$ operating frequency. Unit of RCS values is m^2.

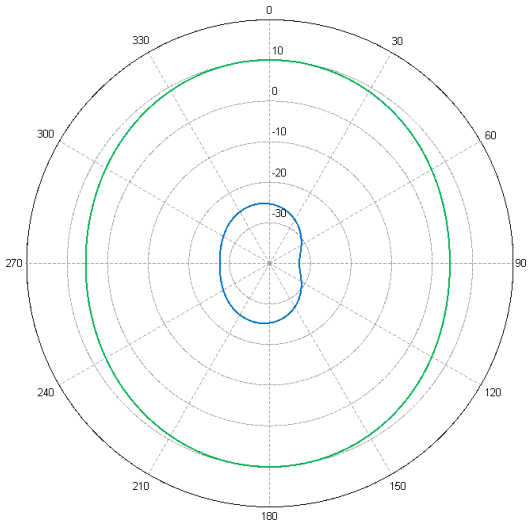

Figure 2.13: The angular bistatic RCS patterns of a $2m \times 1m$ dielectric sheet and a PEC plate of same size (at $\phi = 50°$ and θ is the independent axis) with obliquely illuminated from $\theta = 20°$, $\phi = 50°$ and $\eta = 60°$ at $100MHz$ operating frequency. Unit of RCS values is $dBsm$. Blue and green curves represent Dielectric Sheet and PEC Plate respectively. Unit of RCS values is $dBsm$.

2.4.3. A Dielectric Sphere

In this section a dielectric sphere with $1m$ radius which is placed at the origin of the coordinate system illuminated from the bottom of it will be analyzed for its bistatic radar behavior. In order to perform this besides the sphere; a disc, a cylinder and a cone will be investigated for same illumination setup. Also to see the effect of using a lossless dielectric material instead of perfect electric conductor, perfect electric conductor objects in same dimensions with dielectric ones will be simulated. The aim of this section is to understand the radar cross section behavior of curly dielectric objects. Simulation parameters and models used can be found in Table 2.6 and Figures 2.14(a) to 2.14(d) respectively.

Table 2.6: Bistatic Radar Cross Section Parameters for FEKO Simulations of a Dielectric Disc, Cylinder, Cone and Sphere of $1m$ radius illuminated from the bottom.

Parameter	Values
Wavelength	$\lambda = 0.3m$
Operating Frequency	$f \cong 1GHz$
Radius of Disc Sphere and Cylinder	$1m$
Cylinder and Cone Height	$1m$
Lower Radius of Cone	$0.5m$
Higher Radius of Cone	$1m$
Disc Thickness	$1cm$
Relative Permittivity of Dielectric Material	$\epsilon_r = 36$
Excitation	$\theta = 180°, \phi = 0°$
Triangle Edge Length	$\lambda/8$
Calculations	$\theta = 0° : 1° : 360°, \phi = 0°$

Results In this section to understand the effects of curly surfaces on reflection, a set of objects from a flat disc to a sphere is investigated. In Figure 2.15 the variation of

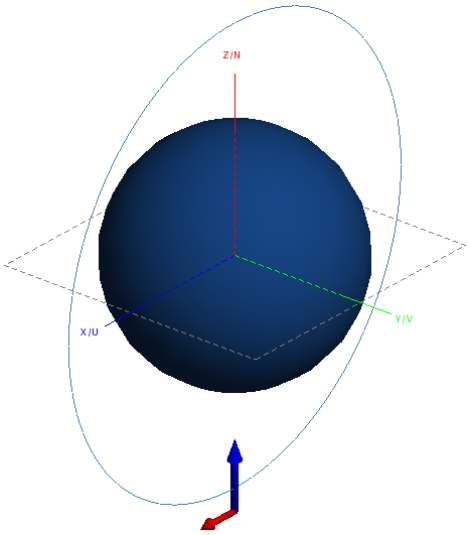

(a) A dielectric sphere of $1m$ radius.

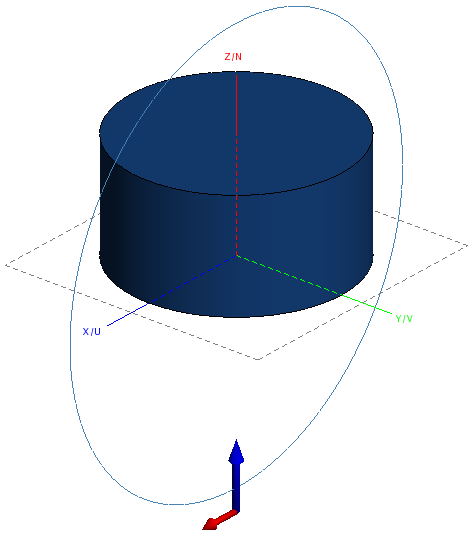

(b) A dielectric cylinder of $1m$ radius and height.

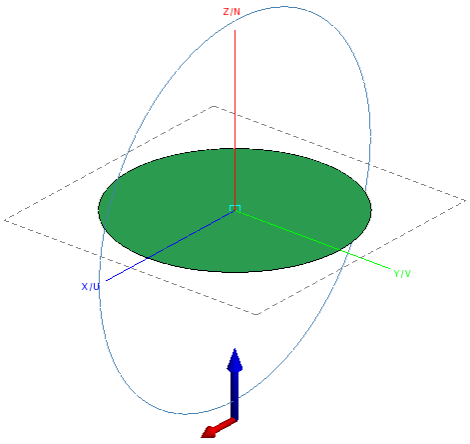

(c) A dielectric disc of $1m$ radius and $1cm$ thickness.

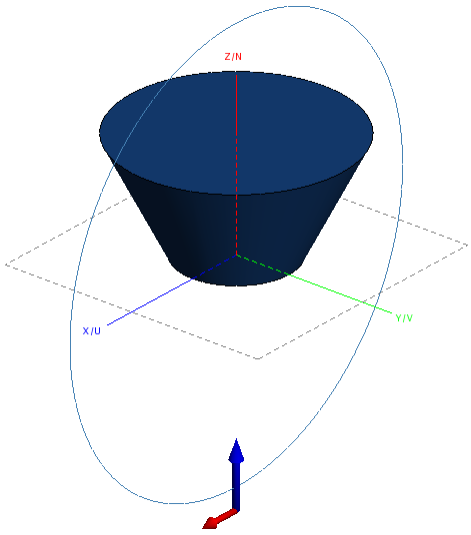

(d) A dielectric cone of $0.5m$ lower radius, $1m$ higher radius and $1m$ height.

Figure 2.14: The CADFEKO models of a dielectric sphere, a dielectric clylinder, a dielectric disc and dielectric cone illuminated from the bottom. The blue and red arrows represent propagation and electric field vectors respectively and the surrounding circles for observation angles.

radar cross section for perfectly electric conductor objects can be seen. And in Figure 2.16 radar cross section values for the dielectric objects of same shapes can be seen. For dielectric shapes unlike the PEC case refraction of incident waves occurs along with reflection and this is the reason for obtaining bigger lobes on upper side of the objects with the increase of curviness of the objects.

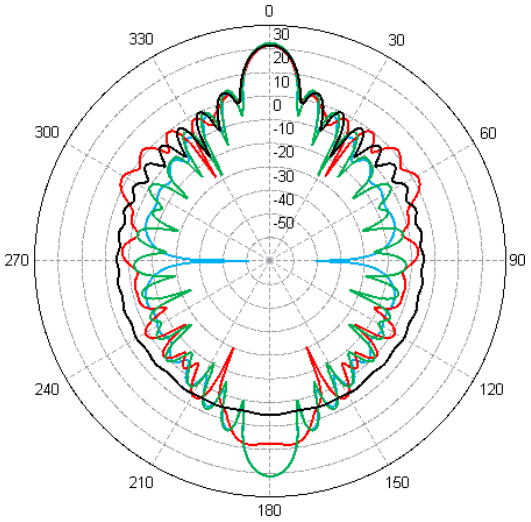

Figure 2.15: An Angular Plot of the radar cross section values ($dBsm$) of a Perfect Electric Conductor Objects. Blue, Red, Green and, Black Lines represents Disc, Cone, Cylinder and, Sphere respectively.

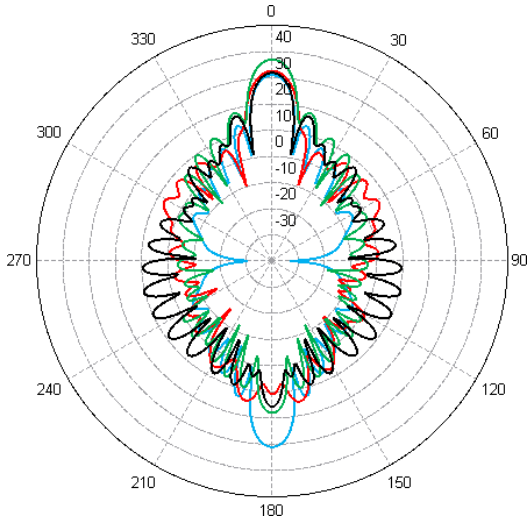

Figure 2.16: An Angular Plot of the radar cross section values ($dBsm$) of Lossless Dielectric Objects ($\epsilon_r = 36$). Blue, Red, Green and, Black Lines represents Disc, Cone, Cylinder and, Sphere respectively

Conclusion In this section based on the canonical example from [14] radar cross section simulations have been made for several geometries to reveal the radar cross section behavior of a dielectric sphere. Besides the experience about radar cross section behavior of several objects, this section was also helpful to practice FEKO's graphical user interface and editing input files. More information about FEKO can be found in [15].

2.4.4. A Perfect Electric Conductor Cuboid

Before analyzing big objects, it is a good practice to investigate FEKO's reliability for an object like a cuboid and see the pros and cons of the software and available solution methods. Also working with a cuboid provides valuable information considering that bigger objects will be constructing using small objects like this. In this section a $10cm \times 80cm \times 20cm$ cuboid placed at $x - y$ plane on one of its big faces, and illuminated normally to one of smaller faces of it, see Figure 2.17. In ongoing sections Physical Optics Method will be used for large objects and to see possible problems, a cuboid in same sizes with the one from [4] will be analyzed to be able to compare results from several methods to calculate radar cross section. The analysis will be for monostatic case in a frequency range from $100MHz$ to $3GHz$. All simulation parameters can be found in Table 2.7

Table 2.7: Monostatic Radar Cross Section Parameters for FEKO Simulations of a $10 \times 80cm \times 20cm$ Perfect Electric Conductor Cuboid Illuminated Normally to one of its $10cm \times 80cm$ faces.

Parameter	Values
Operating Frequency	$100MHz : 100MHz : 3GHz$
Dimensions of Cuboid	10 cm x 80 cm x 20 cm
Excitation	$\theta = 90°, \phi = 0°$
Triangle Edge Length	$0.02m$
Calculations	$\theta = 90°, \phi = 0°$
Solution Methods	PO and MoM for all faces

Results In Figures 2.18 and 2.19 results from [4] and FEKO' solver can be found for the perfect electric conductor cuboid. As expected results from Geometrical Optics Method and Physical Optics Method fit quite perfectly. Considering all of the results from different methods, using Physical Optics Method in ongoing simulations seems

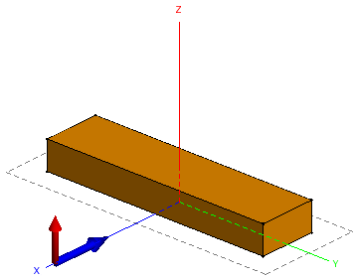

Figure 2.17: A Perfectly Electric Conductor Cuboid Model for Monostatic Radar Cross Section Simulations with Physical Optics Method and Method of Moments. The blue and red arrows represent propagation and electric field vectors respectively.

to be enough for our purpose, for large objects like a vessel or a tank an error of $5dB$ can be considered acceptable.

Conclusion In this section a canonical geometry, a perfect electric conductor cuboid from [4] has been analyzed for its radar cross section behavior. Convincing results were obtained from FEKO using the Physical Optics Method. After this point for simulations of large objects, Physical Optics Method implementation of FEKO will be used in Sections 2.4.6 and 2.4.7. Also in Section 2.4.5 a perfect electric conductor plate coated with a lossy dielectric will be analyzed. Therefore, the solution methods would be in use and possible problems will be revealed for the main problem of this chapter: radar cross section analysis of a tank, and radar cross section optimization alternatives.

2.4.5. A Wedge-Cylinder Plate

In this section with the intention of investigating FEKO's integrity on objects coated with lossy materials, a canonical example, a perfect electric conductor 60° wedge-cylinder plate (See Figure 2.20 and 2.21) will be analyzed for its radar cross section behavior. Then, to see the effect, a lossy coating material will be applied on the plate. The coating material of interest, which is $0.04inch \cong 0.101cm$ thick, is lossy in both

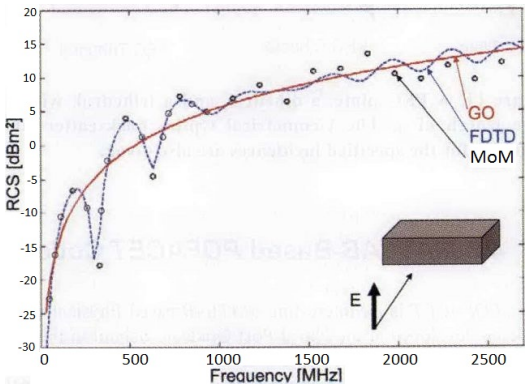

Figure 2.18: A plot of the Monostatic Radar Cross Section of a $10cm \times 80cm \times 20cm$ Perfect Electric Conductor Cuboid, Illuminated Normally to one of its $10cm \times 80cm$ faces, as a function of frequency from[4].

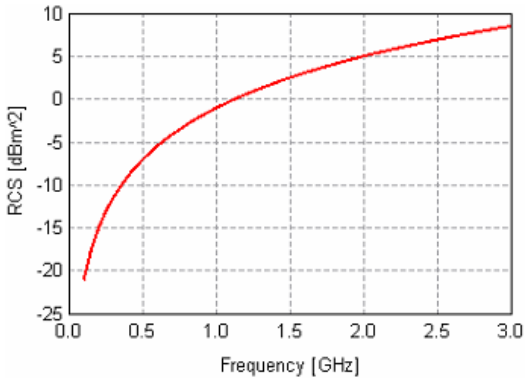

Figure 2.19: A plot of the Monostatic Radar Cross Section of a $10cm \times 80cm \times 20cm$ Perfect Electric Conductor Cuboid, Illuminated Normally to one of its $10cm \times 80cm$ faces, as a function of frequency obtained using FEKO's PO implementation.

dielectric and ferromagnetic way with $\epsilon = 20 - j1.4$ and $\mu = 1.7 - j2.0$. Also, in this section monostatic radar cross section in multiple illumination directions with a 10° of elevation is the concerned calculation.

Until now, in analyses illuminations were horizontal (the polarization parallel to the plate's plane), but for this setup both horizontal and vertical illumination cases will be investigated. Simulation parameters for both cases can be found in Table 2.8.

Results In this section a 60° wedge-cylinder plate coated with a lossy material was selected as a canonical example to analyze. In Figures 2.22(a) and 2.22(b) results for a perfect electric conductor wedge-cylinder plate from [16] and FEKO's solver can be found respectively. For horizontal polarization case results fit quite perfectly. But for

[3]For horizontal polarization case.

[4]For vertical polarization case, in this case it is not possible to create an illumination exactly vertical to the plate, this is the most appropriate case.

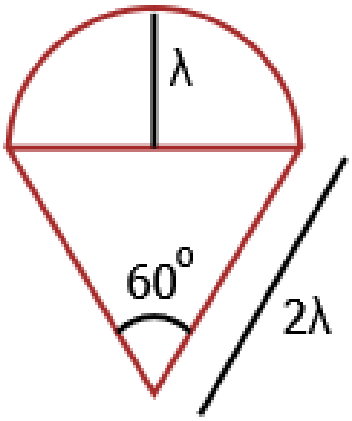

Figure 2.20: Wedge-cylinder plate geometry dimensions.

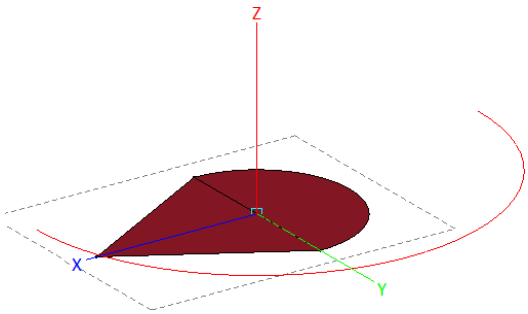

Figure 2.21: A Wedge-Cylinder Plate Model created using CADFEKO for radar cross section analysis of coated objects. Red line represents multiple illumination directions.

Table 2.8: Monostatic Radar Cross Section Parameters for FEKO Simulations of a Perfect Electric Conductor 60° Wedge-Cylinder Plate.

Parameter	Values
Operating Frequency	$5.9GHz$
Wavelength	$\lambda \cong 0.05m$
Complex Permittivity of Coating Material	$\epsilon = 20 - j1.4$
Complex Permeability of Coating Material	$\mu = 1.7 - j2.0$
Excitation	$\theta = 80°, \phi = 0° : 0.5° : 180°$
Polarization Angle	$\eta = 90°$ [3],$0°$ [4]
Triangle Edge Length	$\lambda/10$
Calculations	$\theta = 80°, \phi = 0° : 0.5° : 180°$

vertical polarization, results are slightly different because it is not possible to setup the exact same illumination with FEKO. Despite this difference, results are similar enough to verify FEKO's integrity.

In Figures 2.22(c) and 2.22(d) the effect of lossy material on radar cross section levels can be seen. For horizontal polarization, reduction of radar cross section is around $10dB$ and for vertical case it is even higher than $15dB$ for some angles.

Conclusion In this section a wedge-cylinder plate geometry from [16] was investigated for its radar cross section behavior. Using a lossy material coating, one of the radar cross section reduction methods was observed, and FEKO's integrity on such simulations was validated.

With this section besides gaining necessary experience, FEKO's integrity for several canonical setups is validated. After this point two large objects (a vessel and a cargo freighter) with already known radar cross section information will be analyzed to verify FEKO environment for last time, and a tank which is unknown for its radar cross section behavior will be analyzed.

2.4.6. Teleost Vessel

The CCGS Teleost is a Canadian Coast Guard research vessel. CCGS Teleost is a Canadian coastguard ship which was built in 1988 in Norway and commissioned into the CCG [17]. In this section based on the work from [5], CCGS Teleost Vessel will be investigated for its radar cross section behavior. The length and breadth of the ship are $63m$ and $14.2m$, respectively. In this report a base model (see Figure 2.24) similar to the one from [5] with basic antenna structures will be in use. Other simulation parameters for FEKO simulations and dimensions of the ship can be found in Table 2.9 and Figure 2.25, respectively.

Results FEKO's integrity on radar cross section simulations of large objects is critical for this study. Until this section, several geometries with various illumination

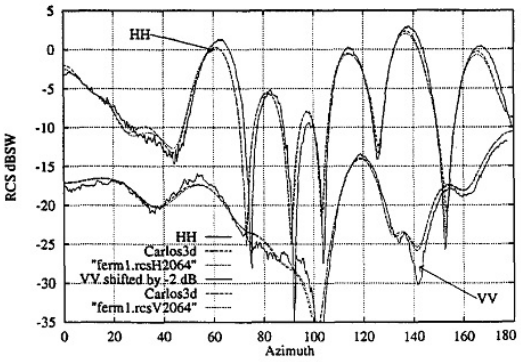

(a) Perfect Electric Conductor, results from [16].

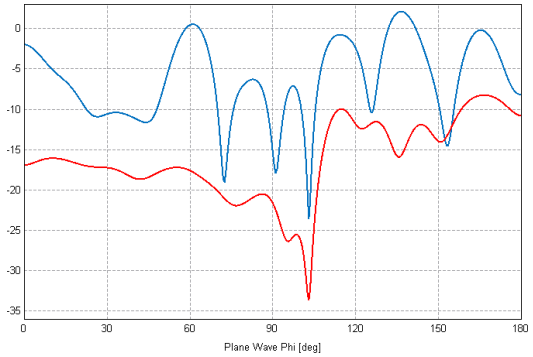

(b) Perfect Electric Conductor, results from FEKO's solver. Blue and red lines represent Horizontal and Vertical polarizations, respectively

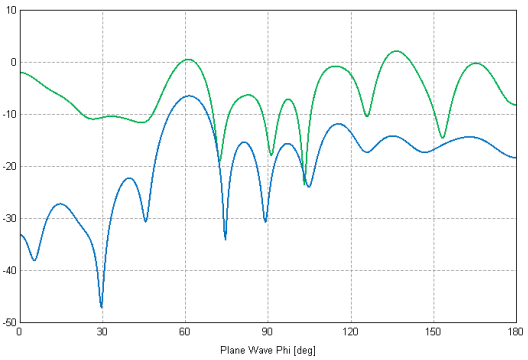

(c) Perfect Electric Conductor coated with a 0.04*inch* Lossy Material,results from FEKO's solver. Green and Blue lines represent non-coated and coated cases respectively.

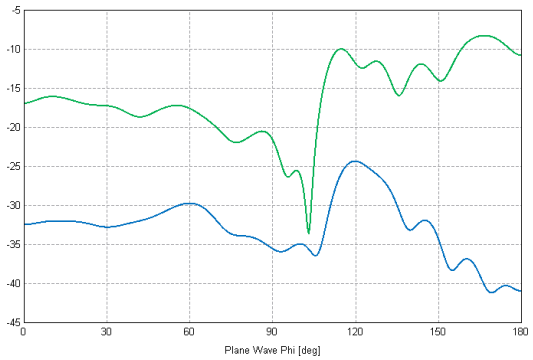

(d) Perfect Electric Conductor Coated with a 0.04*inch* Lossy Material, Green and Blue lines represent non-coated and coated cases respectively.

Figure 2.22: A plot of Monostatic Radar Cross Section of 60° Wedge-Cylinder Plate, Illuminated with Horizontal and Vertical Polarizations with 10° elevation (See Figure 2.21). The vertical scales are in units of dB with respect to a square wavelength (dBSW).

Figure 2.23: Photograph of a CCGS Teleost vessel used in Canadian Coast Guard.

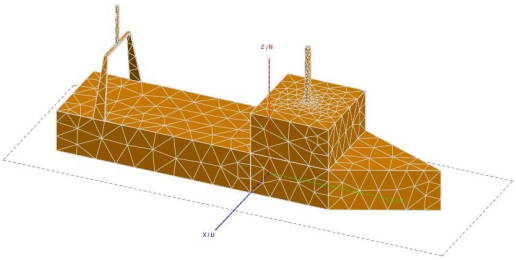

Figure 2.24: Base model of CCGS Teleost Vessel for FEKO simulations with basic antenna structures.

Table 2.9: Monostatic Radar Cross Section Parameters for FEKO Simulations of CCGS Teleost Vessel.

Parameter	Values
Operating Frequency	$4.1MHz$
Excitation	$\theta = 90°, \phi = -90° : 0.5° : 270°$
Mesh Size	$\lambda/20$ ($\lambda/100$ for antennas)
Calculations	$\theta = 90°, \phi = -90° : 0.5° : 270°$ (monostatic)

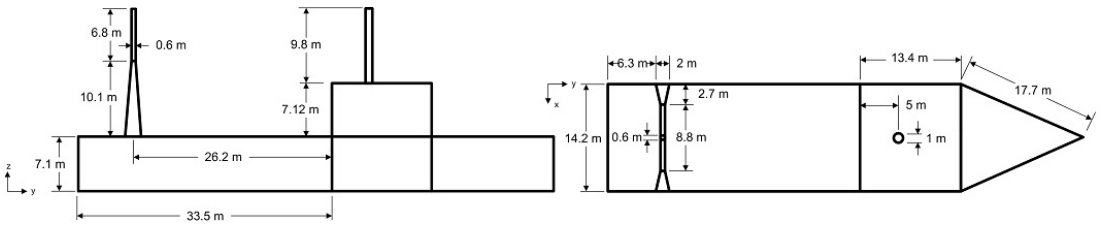

Figure 2.25: Top view and side view of the modeled Teleost vessel.

scenarios have been investigated and in this section a relatively larger geometry was examined. In Figures 2.26 and 2.27 results from [5] and FEKO's solver can be found. Considering the operation frequency (and wavelength) and dimensions, the difference between the results (nearly $6dB$) is acceptable. Besides the slight difference, the patterns of the lines from both sources are very similar. It is also important to note that the solution method used in this section was Method of Moments and if Physical Optics method was used, considering the operation frequency results would be erroneous. Physical Optics Method implementation of FEKO has already been validated in Sections 2.4.1 and 2.4.4 and its weakness in lower frequencies has been observed.

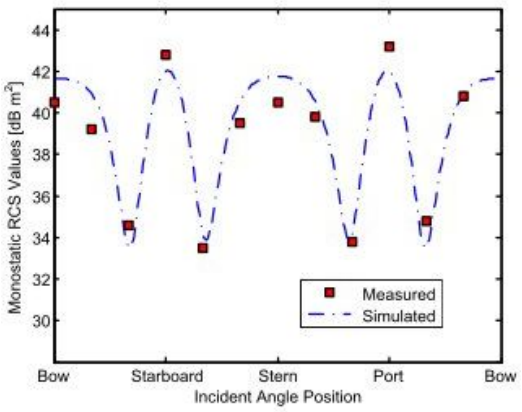

Figure 2.26: A plot of the Monostatic Radar Cross Section of CCGS Teleost Vessel from [5]. Illumination information is available in Table 2.9.

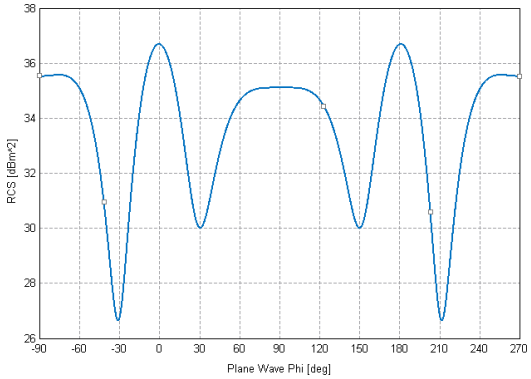

Figure 2.27: A plot of the Monostatic Radar Cross Section of CCGS Teleost Vessel obtained using FEKO's solver. Illumination information is available in Table 2.9.

Conclusion Before simulating the tank geometry of interest for its radar cross section calculations; it is valuable to analyze CCGS Teleost Vessel as an known large object. With this section FEKO's integrity is verified once again (this time for a large object). Also more information about meshing complex geometries can be found in Section 2.5.2.

2.4.7. Bonn Express Cargo Freighter

Bonn Express is a cargo freighter vessel which was built in 1989. In this section based on the work from [5], Bonn Express Vessel will be investigated for its radar cross section behavior. The length and breadth of the vessel are $236m$ and $32m$, respectively. In this section a base model (see Figure 2.29) similar to the one from [5] with basic antenna structures will be in use. Other simulation parameters for FEKO simulations and dimensions of the ship can be found in Table 2.10 and 2.30, respectively.

Figure 2.28: Photograph of Bonn Express cargo freighter vessel.

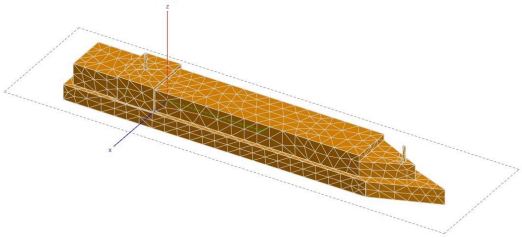

Figure 2.29: Base model of Bonn Express Cargo Freighter Vessel for FEKO Simulations with basic antenna structures.

Table 2.10: Monostatic Radar Cross Section Parameters for FEKO Simulations of Bonn Express Cargo Freighter Vessel.

Parameter	Values
Operating Frequency	$4.1MHz$
Excitation	$\theta = 90°, \phi = -90° : 0.5° : 270°$
Mesh Size	$\lambda/8$ ($\lambda/100$ for antennas)
Calculations	$\theta = 90°, \phi = -90° : 0.5° : 270°$ (monostatic)

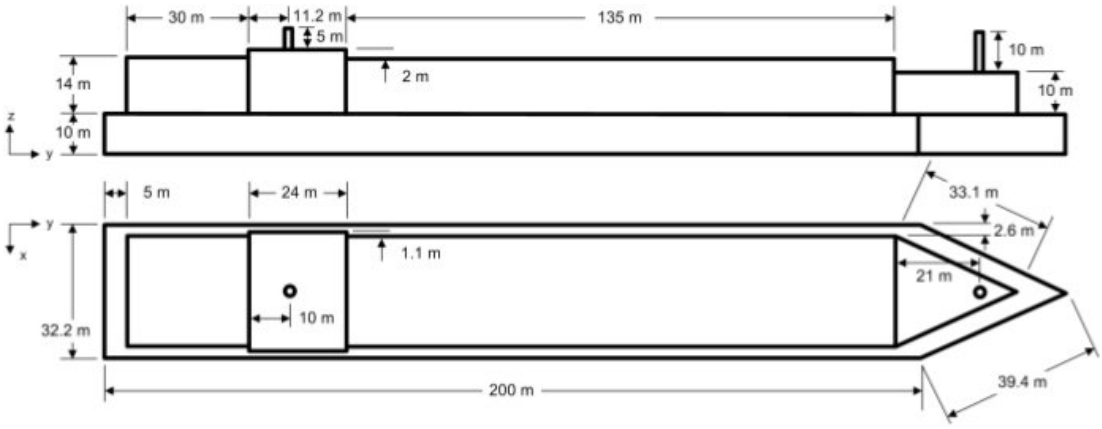

Figure 2.30: Top view and side view of the modeled Bonn Express cargo freighter.

Results In this section a larger geometry than previous section was investigated for its radar cross section behavior and a good agreement between the data from [5] and FEKO's solver was observed, see Figures 2.31 and 2.32. The solution method in use was Method of Moments as in Section 2.4.6. Considering the dimensions of the Bonn Express Vessel (larger nearly four times in length and two times in breadth than CCGS Teleost Vessel), if Physical Optics method was used, besides the effect of operation frequency, results would still be erroneous but less than the ones from Section 2.4.6.

Conclusion Bonn Express Cargo Freighter Vessel was the last canonical setup to investigate for its radar cross section. The results obtained using FEKO and from [5] have a good agreement. In proceeding sections with experience gained before, a tank geometry will be analyzed for its radar cross section behavior.

2.5. Radar Cross Section Analyses of a Tank

Until now, several canonical setups and two vessels have been investigated in terms of their radar cross section behaviors. Method of Moments and Physical Optics Method implementations of FEKO have been tested for radar cross section calculations and

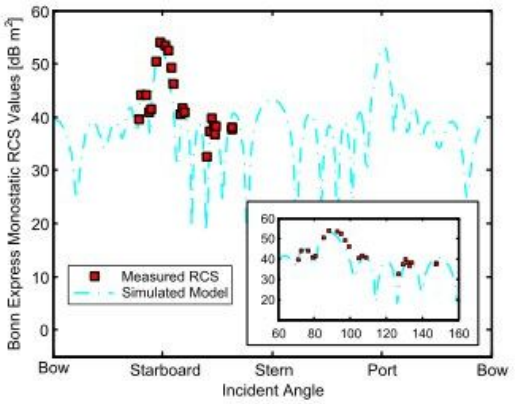

Figure 2.31: A plot of the Monostatic Radar Cross Section of Bonn Express Cargo Freighter Vessel from [5]. Illumination information is available in Table 2.10.

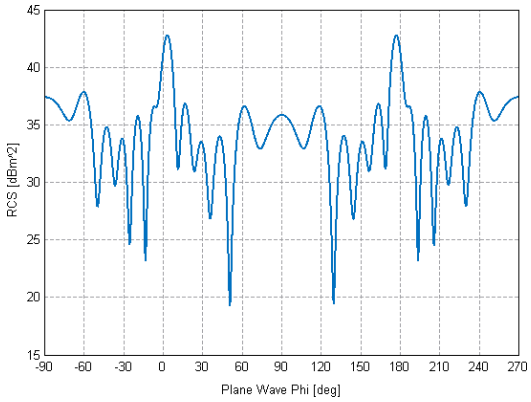

Figure 2.32: A plot of the Monostatic Radar Cross Section of Bonn Express Cargo Freighter Vessel obtained using FEKO's solver. Illumination information is available in Table 2.10.

valuable know-how information has been gained. Besides verifying FEKO's integrity, weaknesses and strengths of these two methods have been observed.

In proceeding sections a tank geometry will be analyzed for its radar cross section within a wide frequency range ($100MHz$ to $35GHz$). To obtain the most reliable results possible with available computational resources, three different models of the tank will be used. Detailed information about the models will be introduced in Section 2.5.1. For all these three models, when running radar cross section simulations Physical Optics Method which reliability in this frequency range has already been proved in preceding sections will be used.

2.5.1. Tank Models

In this section three different models of the tank will be introduced from the most detailed one to the most simple one. The first model is the realistic model of the tank which has been created during mechanical design of the tank. It includes every

physical detail of the tank such as chain wheels or hatches and lids. The second model is the base model of the tank which covers main parts of the tank with very less details than the realistic model. The last model is the simplified model of the tank and consists of just two cuboides for main body parts and one cylinder for the barrel.

In radar cross section simulations of large objects, the most restrictive simulation parameter is triangle edge lengths of meshes. Obviously in higher frequencies to mesh the geometry smaller triangles are needed and the smaller triangles mean the more computational resources. The purpose of using these three different models is to be able to mimic original geometry as accurate as possible in high frequencies. The effects of using simpler geometries will be investigated and results from the base adn the simplified model will be compared for some operation frequencies in proceeding sections.

It is important to note that for all of the models, model bodies were modeled as perfect electric conductors, in frequency range of interest it can be considered as a good assumption [18].

Realistic Model

The realistic tank model as mentioned before the most detailed one which has been created during mechanical design of the tank. FEKO's mesh creation algorithm expects one main triangle edge length from the user and creates the mesh from lots of triangles with edge length around the one user entered. Considering the elaborateness of the realistic model, creating mesh for this model requires more triangles than the other models in number and smaller triangles than the others in size. More information about this non-uniform mesh creation, and possible user intervention can be found in Section 2.5.2.The realistic model of the tank from two different points of view can be seen Figure 2.33.

This model will be used for simulations in the frequency range between $100MHz$ to $8GHz$.

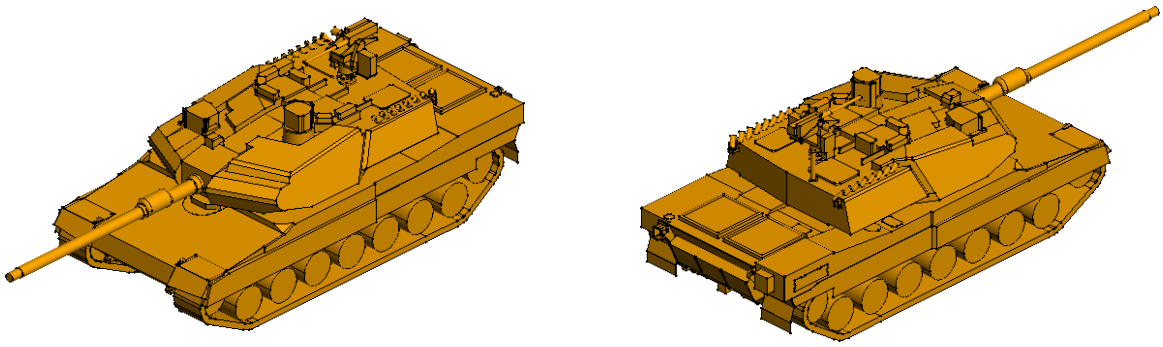

Figure 2.33: The Realistic Model of the tank from left-front corner (on left) and right-back corner (on right).

Base Model

The base model of the tank is a simplified version of the realistic model by removing lots of small parts and replacing them with plates as large as possible. Most likely this base model requires less number of triangles with larger edge lengths. Therefore, simulating base model requires less computational resources than the realistic model. However, reducing complexity of the geometry by replacing little details with flat plates may cause more reflection than the original state. This effect has to be considered when evaluating radar cross section simulation results.

The dimensions of the base model of the tank is nearly the same with the realistic model. The base model of the tank from two different points of view can be seen Figure 2.34.

This model will be used for simulations in the frequency range between $9GHz$ to $18GHz$.

Simplified Model

The simplified model of the tank is created to be able make radar cross section simulations of the tank for frequencies higher than $18GHz$ which was not feasible and/or possible using the base model with available computational resources. As mentioned before the simplified model consists of two cuboids for main body parts

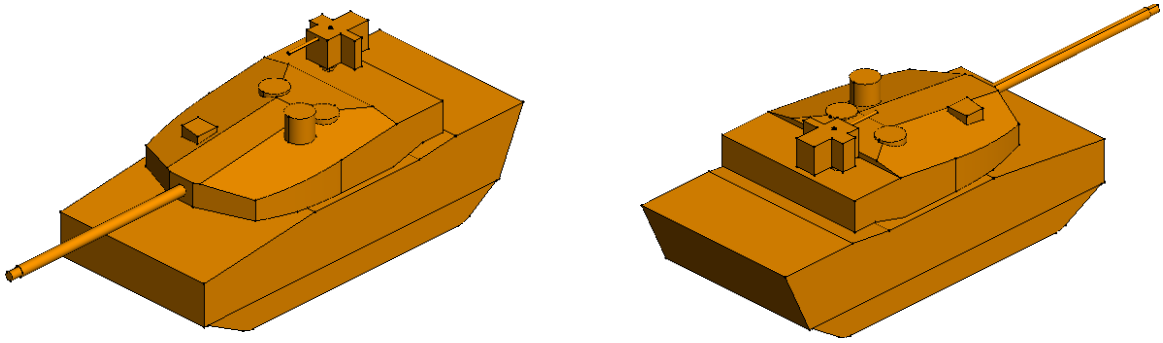

Figure 2.34: The Base Model of the tank from left-front corner (on left) and right-back corner (on right).

and one cylinder for the barrel.

The base model was generated from the realistic model just by simplifying it. However, the simplified model is a new model which was created by sticking to the original dimensions to the utmost. In Figures 2.35 and 2.36 the dimensions of the models can be seen.

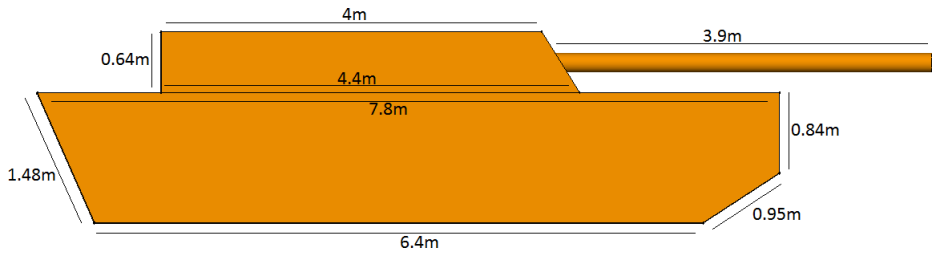

Figure 2.35: Dimensions of the simplified model of the tank from side view.

The realistic model and the base model of the tank have fine details. However, because the simplified model was created for high frequencies as $35GHz$, the simplified model is very coarse and does not have fine details. Since the wavelength at $f = 35GHz$ is very short ($\simeq 8.57 \times 10^{-3}m$), the effects of fine details can be ignored. So that we would expect getting lower RCS values than the other models.

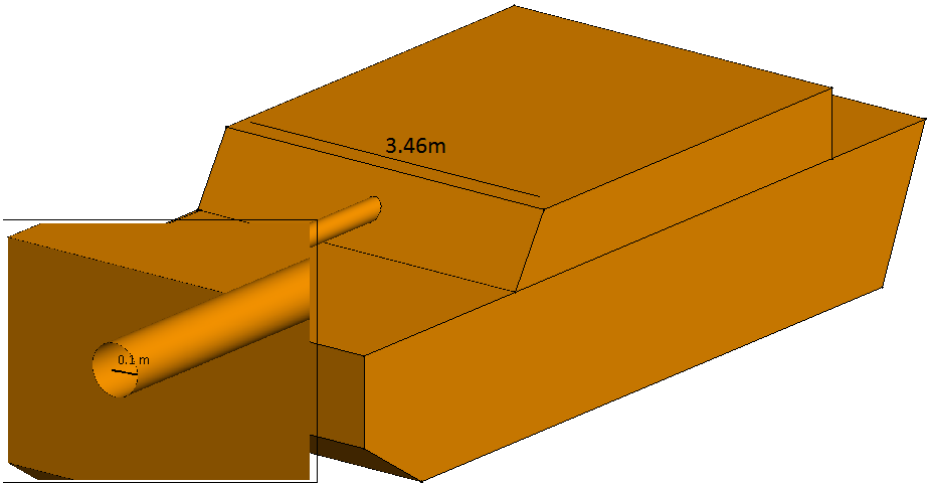

Figure 2.36: Dimensions of the simplified model of the tank from perspective view.

2.5.2. Radar Cross Section Simulations of the Tank Models

In Section 2.5.1 models of the tank will be used in radar cross section simulations were introduced. In proceeding sections monostatic radar cross section behaviors of these models will be analyzed for associated frequency ranges. In all simulations, models will be placed and illuminated as it is shown in Figure 2.37. Besides the illumination case shown in Figure 2.37, illumination with a 10° elevation case will also be investigated for the realistic model.

The realistic model of the tank will be analyzed at the frequency range between $100MHz$ to $8GHz$. For the realistic model FEKO's meshing algorithm will be investigated for practical purposes and user manipulated non-uniform meshing will be discussed.

The associated frequency range for the base model is between $9GHz$ to $18GHz$ as it was mentioned before in Section 2.5.1. Besides the associated range, the base model was simulated for its radar cross section in the frequency range associated with the realistic model to compare the results and to observe the concordance with the realistic model.

The simplified model has been created in order to simulate the tank for its radar

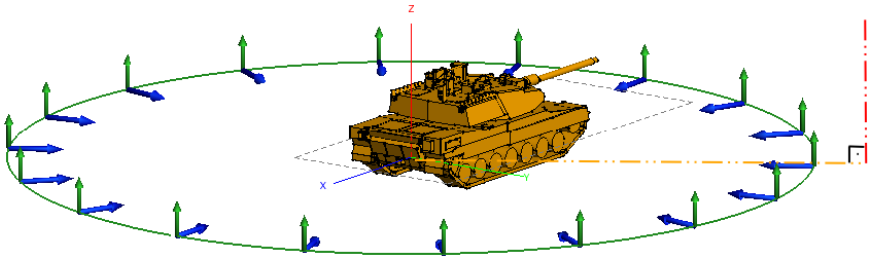

Figure 2.37: Settlement of the models in coordinate system with illumination information. The surrounding circle represents the illumination angles. Each of green and blue arrows represents the electric field vector and the propagation vector at corresponding angle, respectively. For a proper demonstration of the polarization, angular resolution has been taken 20° for these figure, the real angular resolution for simulations can be found at corresponding tables of simulation parameters for models.

cross section in higher frequencies than $18GHz$ and like the base model it was also analyzed the frequency range associated with other models. Because the requested radar cross section of the tank after $18GHz$ was just for $35GHz$, the simplified model has been simulated for this operation frequency only.

Realistic Model

In this section, the realistic model of the tank will be investigated for its radar cross section at the frequency range between $100MHz$ to $8GHz$. The placement of the model and the first illumination case can be seen in Figure 2.37 and the second illumination case can be seen in Figure 2.38. The simulation parameters for both illumination cases can found in Table 2.11.

User-Manipulated Non-Uniform Mesh Creation FEKO's default algorithm for mesh creation demands a user supplied center triangle edge length and creates triangles with edge lengths around this center value. For any geometry, user has the option to assign different center triangle edge lengths for any surface of interest. As

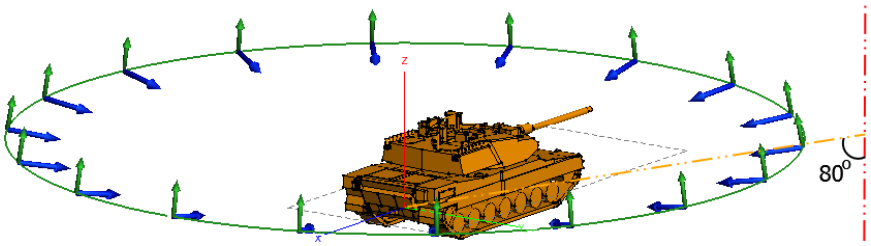

Figure 2.38: Settlement of the models in coordinate system illuminated with 10° elevation from the first case in theta direction. The surrounding circle represents the illumination angles. Each of green and blue arrows represents the electric field vector and the propagation vector at corresponding angle, respectively. For a proper demonstration of the polarization, angular resolution has been taken 20° for these figure, the real angular resolution for the second illumination case is 1°.

Table 2.11: Monostatic Radar Cross Section Parameters for FEKO Simulations of the realistic tank model for two illumination cases.

Parameter	Values
Operating Frequency	$100MHz : 200MHz : 500MHz, 500MHz : 500MHz : 8GHz$
Excitation 1st Case	$\theta = 90°, \phi = 0° : 0.5° : 360°$
Excitation 2nd Case	$\theta = 80°, \phi = 0° : 0.5° : 360°$
Triangle Edge Length	see Section 2.5.2
Calculations 1st Case	$\theta = 90°, \phi = 0° : 0.5° : 360°$ (monostatic)
Calculations 2nd Case	$\theta = 80°, \phi = 0° : 0.5° : 360°$ (monostatic)

it might be expected, these manipulations effect the simulation time and required computational resources.

In this section the effects of user-manipulated non-uniform mesh creation will be explained on simulations of the realistic model. Three different meshes will be created for each operation frequency ($300MHz$, $1GHz$, $2GHz$, $3GHz$, and $4GHz$). The center triangle edge length for the first and the second cases are $\lambda/4$ and $\lambda/8$ (FEKO's default), respectively, where λ is free-space wavelength. For the third case, some selected surfaces (as shown in Figure 2.39) will be meshed with center triangle edge length as $\lambda/4$ and the rest will be meshed with center triangle edge length as $\lambda/8$. The selected surfaces are relatively larger ones, the purpose of this selection is to reduce the memory requirement with reducing number of the triangles.

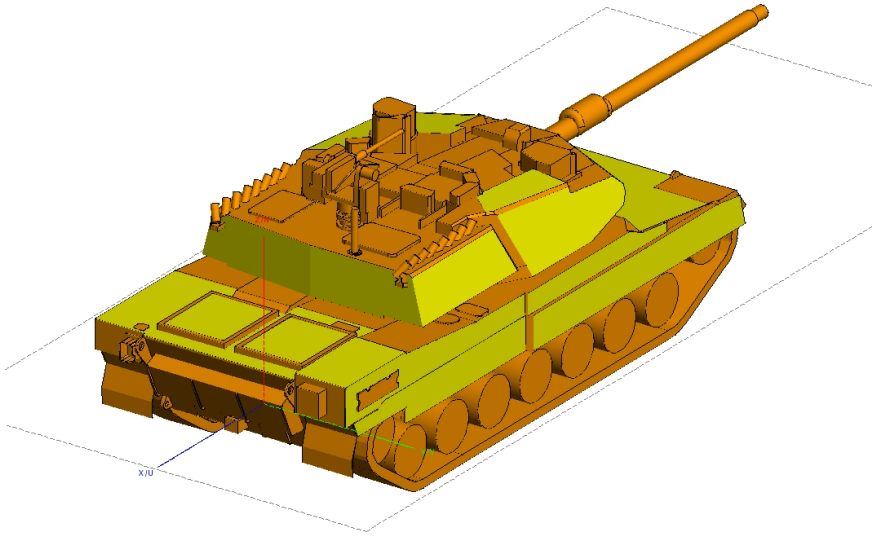

Figure 2.39: The realistic model showing selected large surfaces (light yellow ones) for user-manipulated non-uniform mesh creation.

In Figure 2.40 the effects of user-manipulated non-uniform mesh creation on simulation time and memory requirement can be seen. As it is expected, number of triangles is proportional to memory usage. Besides being a quite straightforward way to reduce the memory requirement, making the mesh coarser is a reliable method for

FEKO simulations.

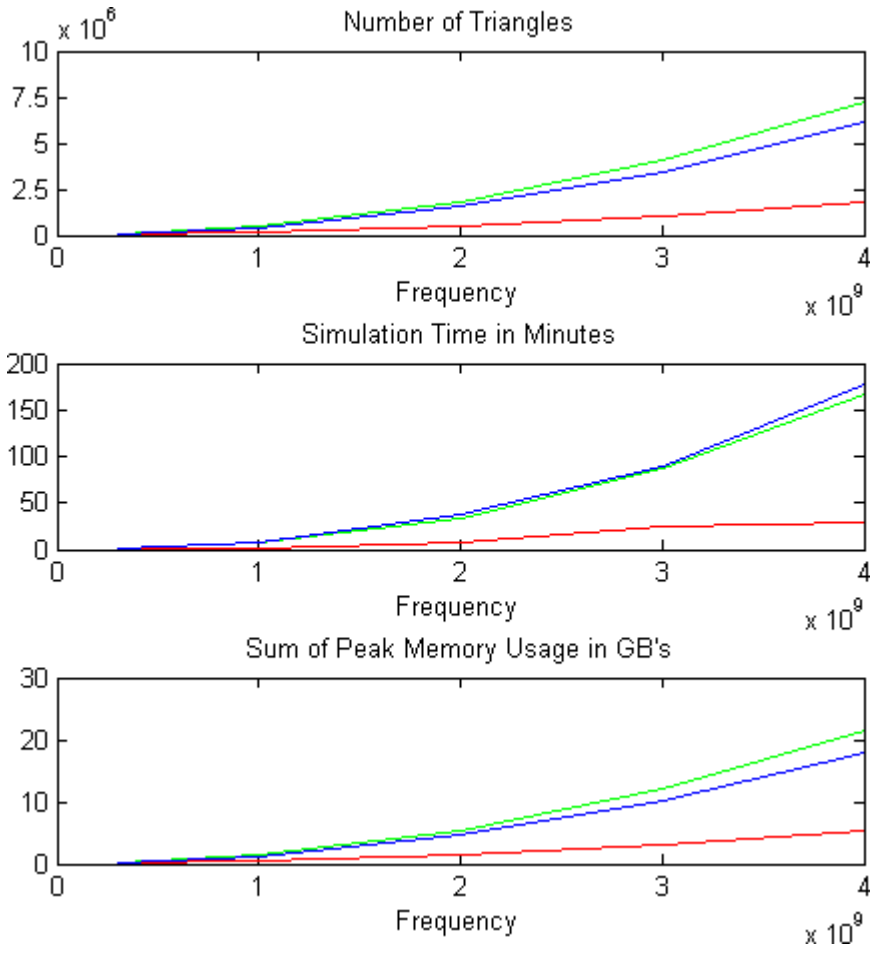

Figure 2.40: User-Manipulated Non-Uniform Mesh Creation. Red and Green Lines represent center triangle edge length as wavelength over 4 and 8, respectively. Blue lines represent mixed center triangle edge lengths. The exact same amount of computational resources provided to solver for all three cases.

As long as FEKO's solver allows using the mesh provided despite how coarse it is, solver provides reliable results. When the computational resources are limited, despite the trade-off in simulation time, it becomes only way to run simulations. Also this trade-off is generally in an acceptable level.

Results In this section the realistic model of the tank has been investigated for its radar cross section at the frequency range between $100MHz$ to $8GHz$.

When the realistic model illuminated with a 10° of elevation ($\theta = 80^\circ$) than the first case, there is a significant reduction on radar cross section values which is consistent with the canonical setups.

Base Model

In this section, the base model of the tank will be investigated for its radar cross section behavior at frequencies 9, 12, 15, and $18GHz$. Besides these frequencies, to understand the reliability level of the base model, its radar cross section will also be calculated at the same frequency range with the realistic model. For the simulations the same illumination setup will be used and monostatic radar cross section values will be calculated. Parameters for FEKO simulations can be found in Table 2.12

The base model of the tank has more flat surfaces than the realistic model. Therefore, higher radar section values might be expected especially at the angles which excessive reflection occurs (as $\theta = 90^\circ$ or $\theta = 0^\circ$. But when average values of the radar cross section or polar plot of radar section values considered, the base model would be reliable.

Table 2.12: Monostatic Radar Cross Section Parameters for FEKO Simulations of the base model of the tank for two illumination cases.

Parameter	Values
Operating Frequency	$100MHz$ to $18GHz$
Excitation 1st Case	$\theta = 90^\circ, \phi = 0^\circ : 0.5^\circ : 360^\circ$
Excitation 2nd Case	$\theta = 80^\circ, \phi = 0^\circ : 0.5^\circ : 360^\circ$
Triangle Edge Length	$\lambda/4$
Calculations 1st Case	$\theta = 90^\circ, \phi = 0^\circ : 0.5^\circ : 360^\circ$ (monostatic)
Calculations 2nd Case	$\theta = 80^\circ, \phi = 0^\circ : 0.5^\circ : 360^\circ$ (monostatic)

Realistic Model vs. Base Model When we compare all of the obtained results, radar cross section of the base model is quite consistent with the radar cross section of the realistic model. As it might be expected, for the illumination angles where excessive reflection occurs, relatively higher radar cross section values observed. But, even though these angles, the base model is very reliable for radar cross section simulations of the tank.

Results In Figures 2.41(a) to 2.41(d) radar cross section values of the base model of the tank at frequencies of interest for the first illumination case can be found.

It is important to mention once again that the base model has more flat surfaces than the realistic model and this causes excessive reflection at illumination angles like $\phi = 90$ (where normal illumination occurs for majority if illuminated surfaces). Therefore, while interpreting the results of the base model of the tank, considering this and ignoring unusual peaks at the mentioned angles would be a good practice.

Simplified Model

The base model was generated from the realistic model just by simplifying it. However, the simplified model is a new model which was created by sticking to the original dimensions to the utmost. In Section 2.5.1 the models can be found.

Detailed triangle edge length information of the realistic model can be found in the previous sections. For the calculations of the simplified model, default length that FEKO recommends ($\lambda/8$) is used in simulations which have been made to verify the compatibility of the models. The lowest possible length for the simulation at $35GHz$ is $\lambda/5$. An example nonuniform mesh which is created with FEKO's default settings is shown in Figure 2.42.

Compatibility of the Models The models that have been used before the simplified model had fine details. However, because the simplified model was created for high frequencies like $35GHz$, it is very coarse and does not have fine details. Since the wavelength at $f = 35GHz$ is very short, the effects of fine details can be ignored.

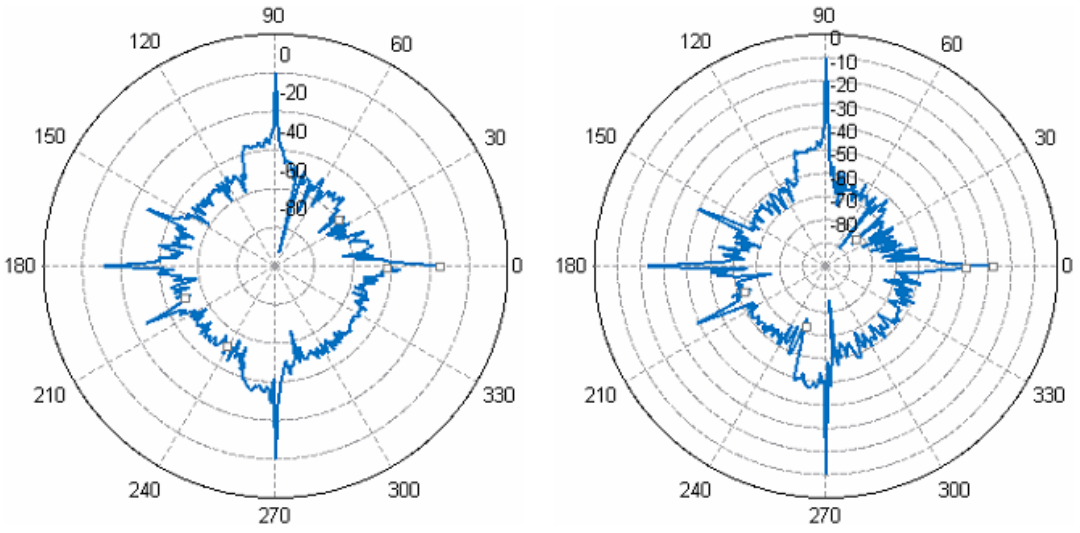

(a) $f = 9GHz$

(b) $f = 12GHz$

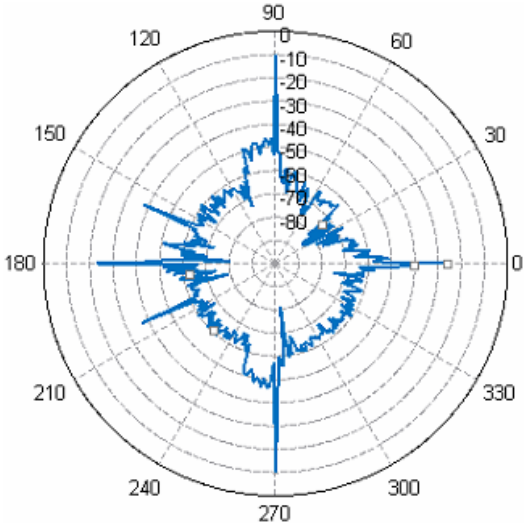

(c) $f = 15GHz$

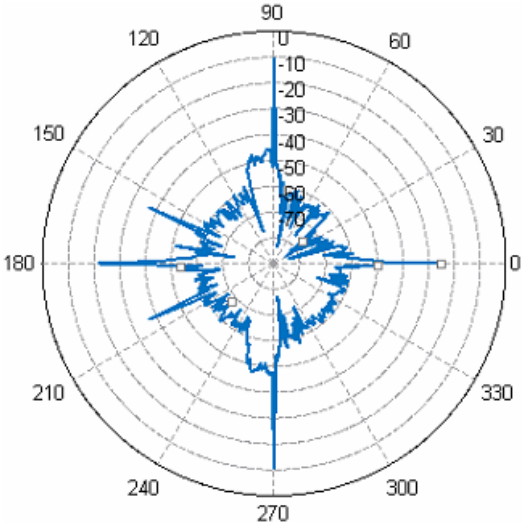

(d) $f = 18GHz$

Figure 2.41: Normalized Polar Plots of monostatic radar cross section values ($dBsm$) of the the base model illuminated from $\theta = 90°$ and $\phi = 0 : 2 : 360$.

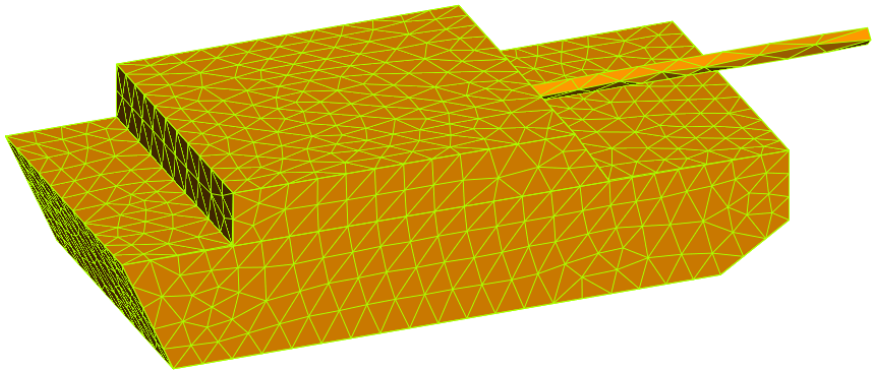

Figure 2.42: Mesh used in radar cross section simulations of the simplified model at 100 MHz (Meshes at higher frequencies are not visible without zoom).

So that we would expect getting lower radar cross section values than models before if the simplified model is simulated at lower frequencies. This section compares the radar cross section values of the base model and the simplified model at a relatively lower frequency range $(300MHz, 5GHz)$ to show their concordance. To show the concordance of the models, polar plots of the results are plotted together at the frequency range between $300MHz$ to $5GHz$ for all three models. From Figure 2.43(a) to 2.43(d) blue and green lines indicates results of the base model and the simplified model, respectively.

The average radar cross section values of realistic model is nearly slightly higher than the simplified model, not including the highest values at the angles normal to the surfaces. At the normal angles, because we used single large plates instead of several fine detailed parts, radar cross section values of the simplified model (similar to the base model) are higher than the values of the realistic model. Considering the differences between the values of the base model, the simplified model can be accepted as a reliable model.

Results Even though the simplified model is a quite simplified version of the realistic model, because of the very short triangle edge length (and a very big mesh size) it was not possible to make calculations with the whole model. So the model is divided

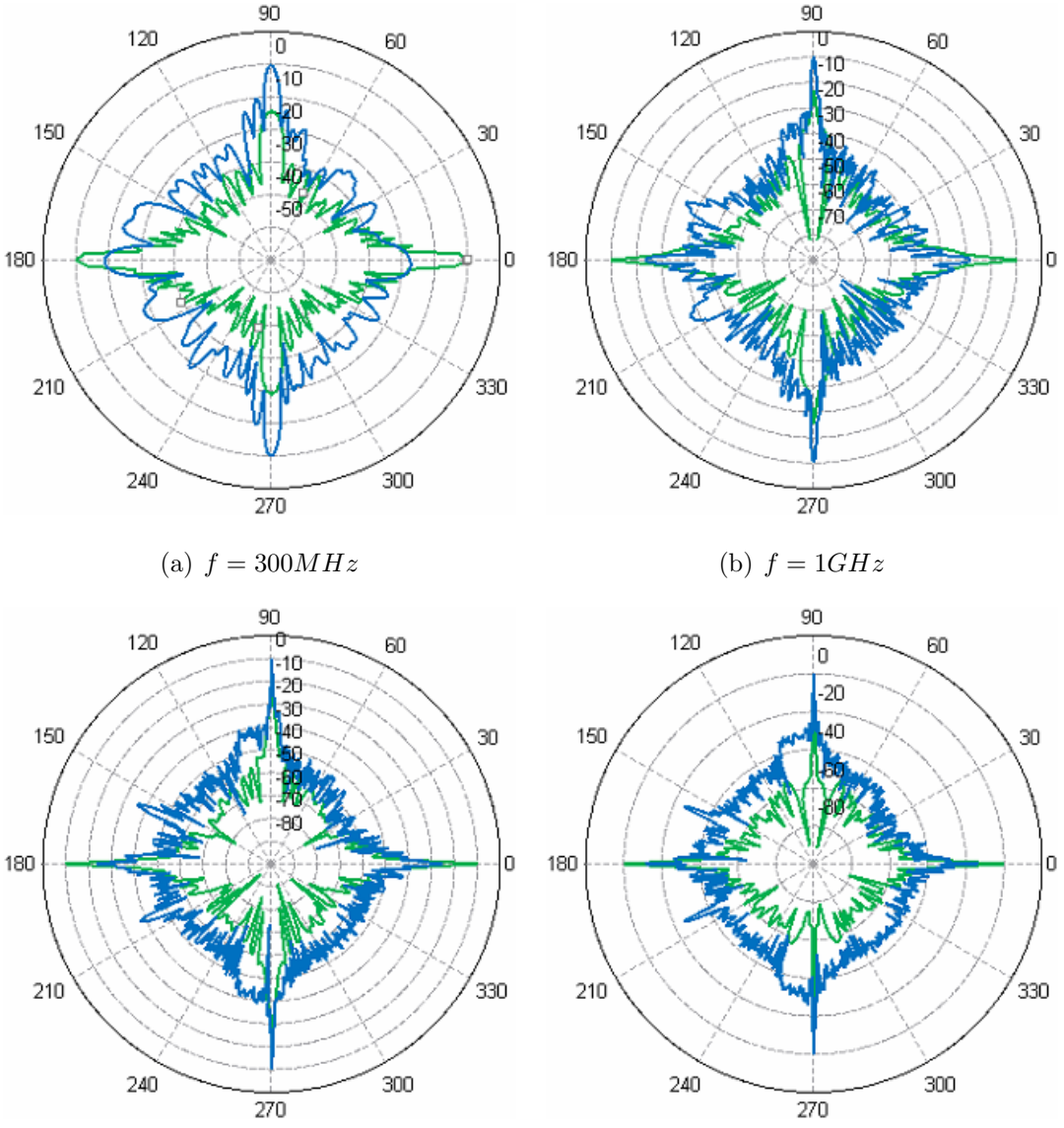

(a) $f = 300MHz$ (b) $f = 1GHz$

(c) $f = 3GHz$ (d) $f = 5GHz$

Figure 2.43: Normalized Polar Plots of monostatic radar cross section values ($dBsm$) of the base and the simplified model ($dBsm$). Blue and green lines represent the base model and the simplified model, respectively, $\theta = 90°$, $\phi = 0 : 2 : 360$

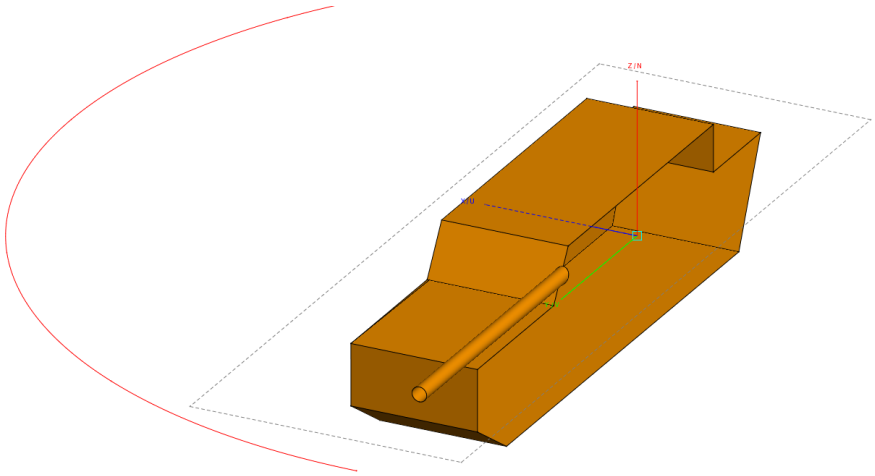

Figure 2.44: Side Part of the Simplified Model. The red curve indicates the solution loop is covered the angles $\phi = 0 : 2 : 60$ and $0 : -2 : 300$.

into three models with different points of view (from side, front, and back).

Dividing the simplified model lowered the need of computational resources required. However it also has a trade off as causing false calculations at the angles near the dividing parts of the divided models which are shown in Figures 2.44 to 2.46. To avoid this problem, calculations have been created by narrowing the solution loops by 30° from both beginnings and ends of divided models (the solution loops are shown in the same figures with red color).

In Figure 2.47, the values of the left side is the symmetrical of the right side's. The results at angles which have values from both side and front or from side and back are quite overlapping. To obtain overlapping results like this solution loops are narrowed by 30°. Also the values at the normal angles of the surfaces causes higher values as expected, because of using single large plates instead of fine detailed several parts.

Considering the needed computational resources for the calculation of radar cross section of the tank at $35GHz$ or the higher frequencies, the necessary resources will become unobtainable and more simplified models or other techniques will be required. It is still doable, but the model used for this will become very unreliable and the

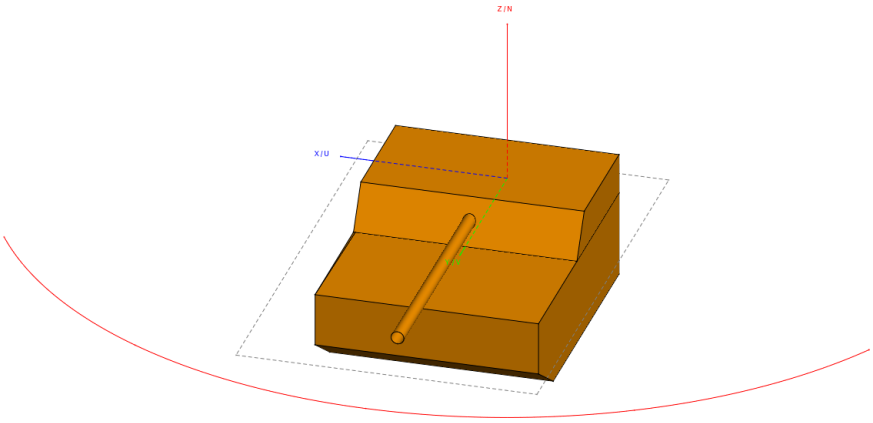

Figure 2.45: Front Part of the Simplified Model. The red curve indicates the solution loop is covered the angles $\phi = 30 : 2 : 150$.

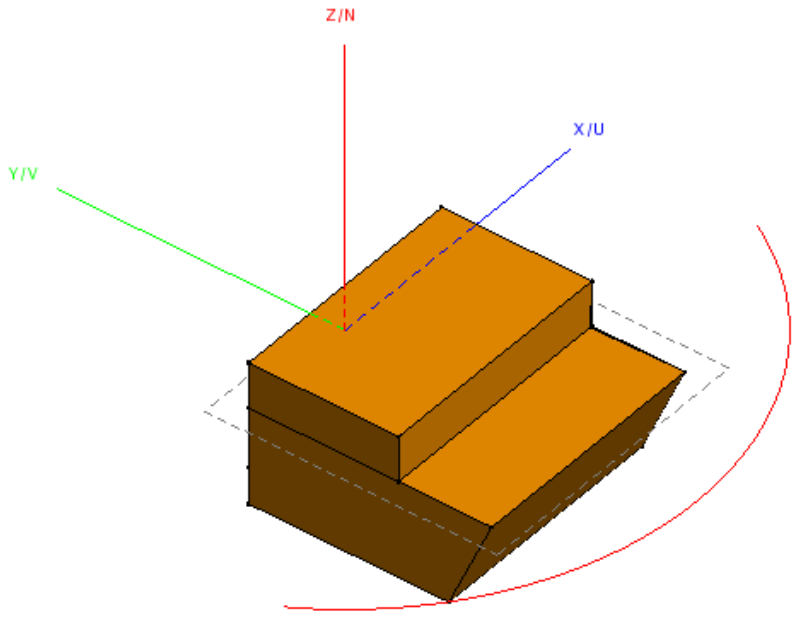

Figure 2.46: Back Part of the Simplified Model. The red curve indicates the solution loop is covered the angles $\phi = 210 : 2 : 330$.

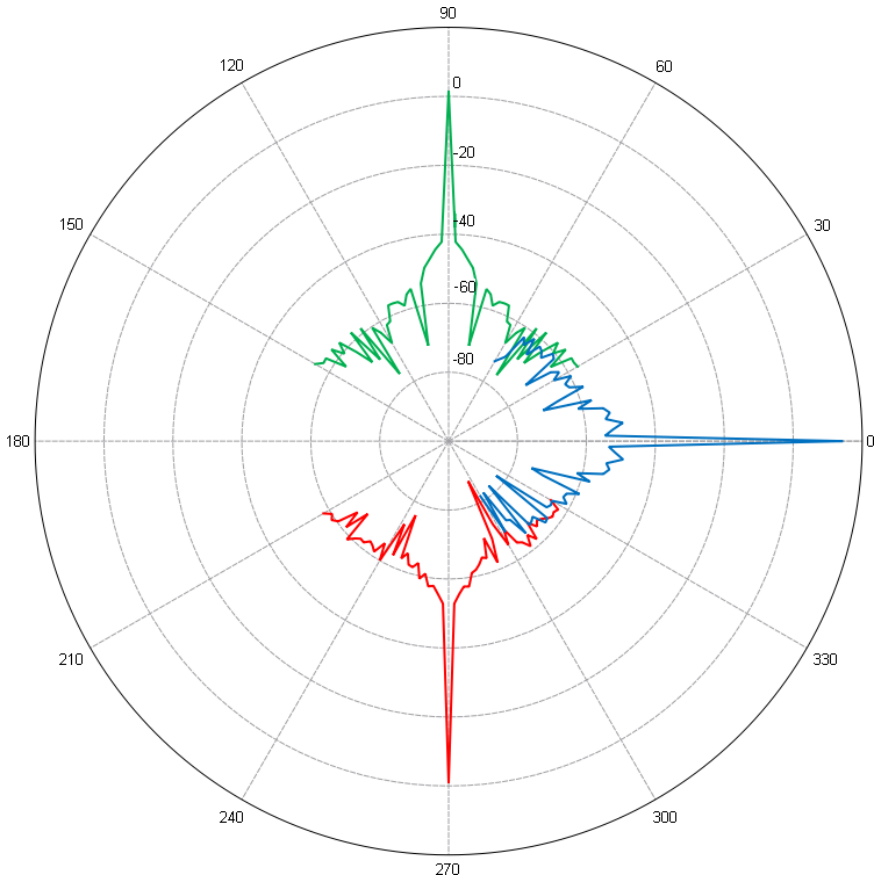

Figure 2.47: The Simplified Model, Normalized Monostatic Radar Cross Section values at $f = 35GHz$, $\theta = 90°$, $\phi = 30 : 2 : 150$ for front part, $\phi = 0 : 2 : 60$ and $0 : -2 : 300$ for side part, and $\phi = 210 : 2 : 330$ for back part.

time requirement will be quite long. Also the reliability of FEKO at longstanding simulations running is problematic.

In this section, the work done for a tank's radar cross section calculations at $35GHz$ is explained. The reliability of the simulation results at different frequencies were verified. Even though the provided results are not exact, these results can be considered as enough information for reflection behavior at $35GHz$.

2.6. Appraisal of the Results

Until now,the radar cross section behavior of a tank has been analyzed for a wide frequency range from $100MHz$ to $35GHz$. Three different tank models have been offered for particular frequency ranges and compatibility of the models has been verified.

For military vehicles, when it is wanted to calculate a tanks radar cross section values before manufacturing, it is quite not possible to access radar cross section values of other similar vehicles and compare the results with them. Considering this, in this study a sequential way has been followed for radar cross section simulations.

In the first phase, several canonical setups with already known reflection information have been investigated for their radar cross section behavior and a base has been constructed for the next simulations. Then two vessel ships with known reflection information have been analyzed as large geometries. Lastly radar cross section behavior of the tank of interest has been analyzed with the experience gained. It is still hard to expect these results to match with the possible measurement results perfectly but the exhibited results may provide a base to predict radar cross section values of the tank for different illumination scenarios.

2.6.1. Determining the Parts Causing Excessive Reflection

The radar cross section of large objects is the decisive parameter that designates how the device would be appeared on radar screen. During the design process of the device

geometry it is important to offer optimization for lowering radar cross section values. In this section for the tank geometry that we interested, the parts where the excessive reflection occurs will be discussed and in ongoing sections some optimizations will be offered.

Considering the results obtained, the highest radar cross section values are observed at the angles where normal incidence occurs on large flat plates. In Figure 2.48 the light yellow surfaces indicate potential surfaces that might cause excessive reflection.

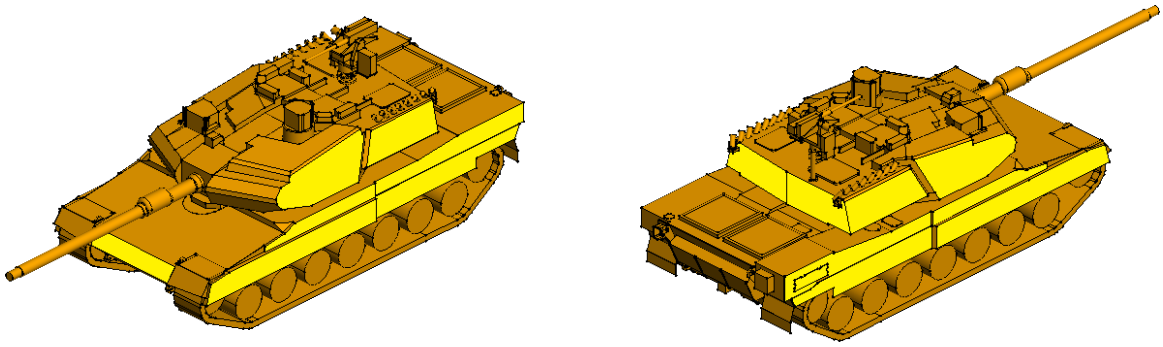

Figure 2.48: The Realistic Model of the tank indicating the potential surfaces (light yellow ones) that might cause excessive reflection.

In ongoing sections possible methods to reduce the radar cross section values of objects will be discussed and to optimizations for the tank of interest will be offered.

2.7. Radar Cross Section Reduction

It has been apparent for some time that the development of increasingly sophisticated detections systems threatens to reduce the mission effectiveness of many types of weapon platforms [13]. Even though radar detection systems are not a topic of interest for this study, increasing the survivability by reducing detectability is one of our concerns besides determining the current detectability. Complex objects like vessels and tanks may be represented as a collection of basic geometric shapes as flat plates,

cuboids and such. In preceding sections using such basic geometries, there tank models have been created and radar cross section behavior of the tank has been investigated in the light of reflection behaviors of these geometries. In proceeding sections the methods used to reduce the detectability of the tank will be discussed.

There are several techniques for reducing detectability (or radar cross section) of complex objects. In [13] four methods are offered.

- Shaping
- Radar Absorbing materials
- Passive cancellation
- Active cancellation

We have tried the first two methods for reducement in this study. Shaping optimizations are discussed in Section 2.7.1 and optimizations using radar absorbing materials in Section 2.7.2. The other two methods can also be considered but not have not been applied yet (see [13] for detailed information). Before proceed on methods applied it is important to note that, all radar cross section methods have their advantages and disadvantages, there are trade-offs for every optimization.

2.7.1. Shaping

Shaping or modifying the geometry is the first option considered for radar cross section reduction of the realistic tank model. After evaluating the radar cross section values of the current models (see Section 2.6) the parts may cause excessive reflection have been determined in Section 2.6.1. In this section several geometrical modifications will be applied to the realistic model of the tank and effects will be discussed[5].

[5]This part of the study was completed in collobaration with Dilara Bağdat who was a Senior RF Systems Eng / Team Leader at RMK Marine / Koç Bilgi Savunma Tek. AŞ .

Modifications on the Tank Geometry

When the realistic model of the tank and its radar cross section values (see Section 2.5.2) are considered, the sponson[6] of the tank would be a good point to start with. In this section several modification cases on the sponson of the tank based [19] will be investigated.

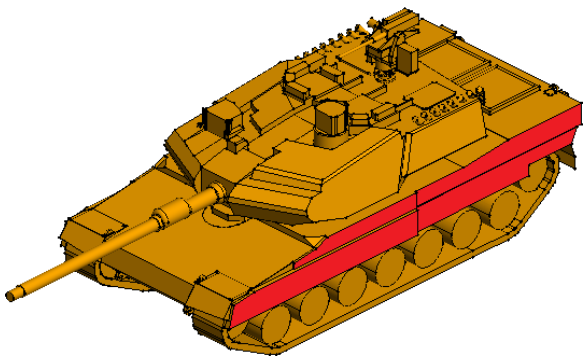

Figure 2.49: Sponson of the realistic tank model, red faces indicate sponson of the tank.

As the first modification upper-left part of the sponson was tilted to 5° and 7° from lower edge with an expectation to get lower radar cross section. But instead, tilting caused higher radar cross section at the angles of interest ($\theta = 90°$ and $\phi = 268 : 272$).

To investigate the reason of the increase with tilting instead of the expectation, simulations were repeated with models without chain wheels and/or tower. However, removing chain wheels did not resolve the problem but causes a shift on peak angles. Therefore, chain wheels are not the main source of the excessive reflection. Also removing the tower (see Figure 2.51) and removing both chain wheels and tower (see Figure 2.52) did not resolve the problem.

After removing chain wheels and tower of the tank, to easily manipulate the sponson geometry, minor parts ignored and a simpler geometry (see Figure 2.53 was

[6] Any of several structures that project the side of a ship, tank etc. See Figure 2.49 for the sponson of the realistic tank model.

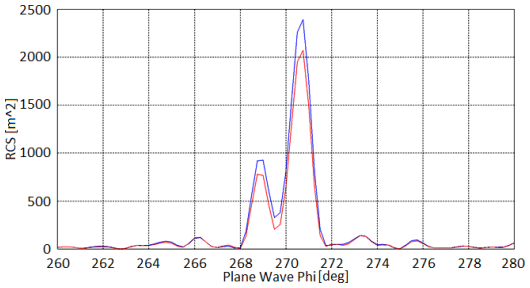

Figure 2.50: Effects of first modification on the upper-left part of the sponson without chain wheels at $1GHz$, red and green lines represent $0°$ and $5°$ of tilt, respectively. $(\theta = 90°)$

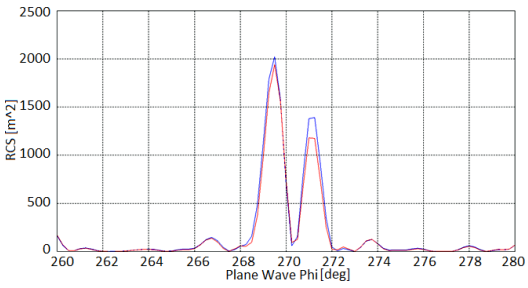

Figure 2.51: Effects of first modification on the upper-left part of the sponson without tower at $1GHz$, red and blue lines represent $0°$ and $5°$ of tilt, respectively. $(\theta = 90°)$

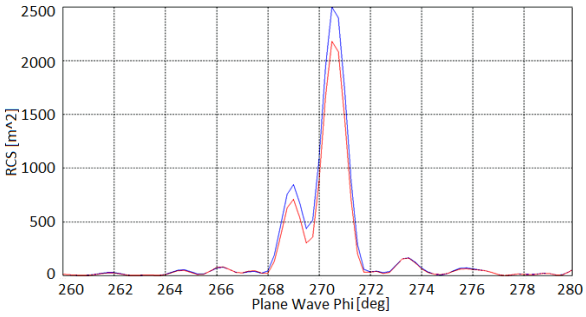

Figure 2.52: Effects of first modification on the upper-left part of the sponson without chain wheels and tower at $1GHz$, red and blue lines represent $0°$ and $5°$ of tilt, respectively. $(\theta = 90°)$

used. Again, for this simpler geometry upper-left part of the sponson was tilted and the similar behavior (see Figure 2.55 was observed.

Afterwards as one more simplification, right side of the sponson were removed as in Figure 2.54. As might seen in Figure 2.56, with analyzing left side of the sponson alone, the peak level was lowered but the increasing with the tilt behavior remained still. And obviously difference at the depth of the parts was causing the two-peak behavior when analyzing the whole sponson.

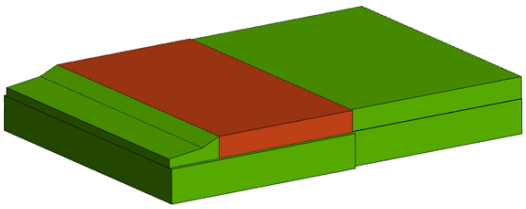

Figure 2.53: Sponson geometry of the realistic tank model without small features.

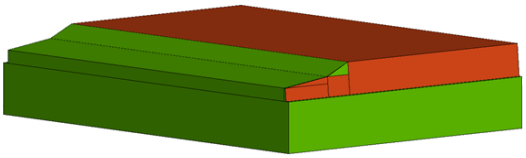

Figure 2.54: Left side of the sponson geometry of the realistic tank model without small features.

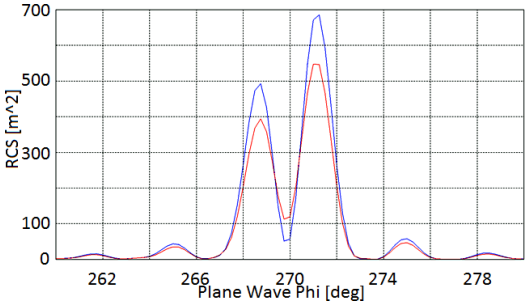

Figure 2.55: Radar Cross Section of the sponson geometry of the realistic tank model without small features, at $1GHz$. Red and blue lines represent $0°$ and $5°$ of tilt, respectively ($\theta = 90°$).

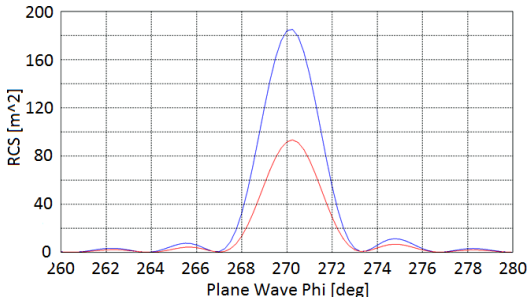

Figure 2.56: Radar Cross Section of the left part of the sponson geometry of the realistic tank model without small features, at $1GHz$. Red and blue lines represent $0°$ and $5°$ of tilt, respectively ($\theta = 90°$).

Then lower-left part of the sponson was removed (see Figure 2.57) and lower radar cross section values with tilt were observed (see Figure 2.58) as might be expected.

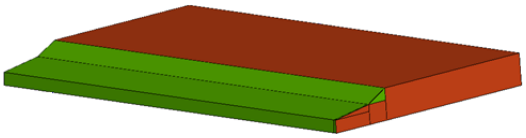

Figure 2.57: The upper-left part of sponson geometry of the realistic tank model without small features.

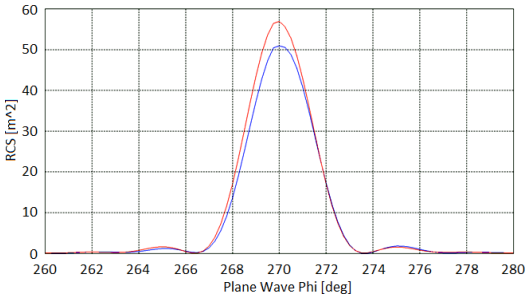

Figure 2.58: Radar Cross Section of the upper-left part of sponson geometry of the realistic tank model without small features, at $1GHz$. Red and blue lines represent $0°$ and $5°$ of tilt, respectively ($\theta = 90°$).

Lastly, lower-left part (Figure 2.59) and right side (Figure 2.60) of the sponson were added back to the upper-left part but this time in a smoother way with no indents and lower radar cross section values with tilting the upper part of the sponson were observed as desired, see Figures 2.61 and 2.62. Also similar results for $10GHz$ operating frequency can be found in Figure 2.63. At $10GHz$ operating frequency, obviously the discontinuities of the geometry are not the reason to obtain higher radar cross section values. Even though the lowest values were obtained from the smoothed and tilted geometry, the difference is comparable.

Conclusion In this section several modifications have been applied to the sponson of the realistic model of the tank and radar cross section behavior at angles modifications had been applied have been inspected. Using smooth geometries instead of original intricate geometry provides reduction with tilting the faces. But the trade-off of these modifications is obtaining much higher peak radar cross section values with specular

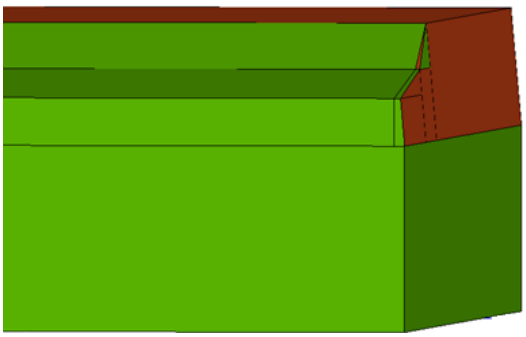

Figure 2.59: The smoothed left side of sponson geometry of the realistic tank model without small features.

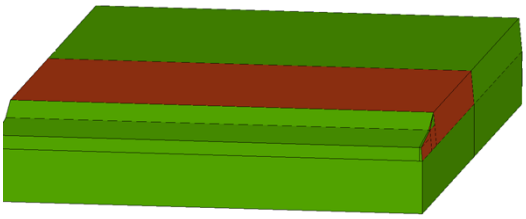

Figure 2.60: The smoothed sponson geometry of the realistic tank model without small features.

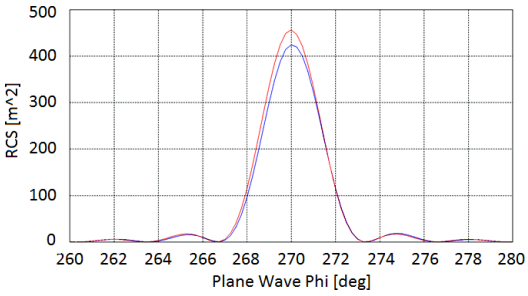

Figure 2.61: Radar Cross Section of the smoothed left side of sponson geometry of the realistic tank model without small features, at $1GHz$. Red and blue lines represent $0°$ and $5°$ of tilt, respectively. ($\theta = 90°$).

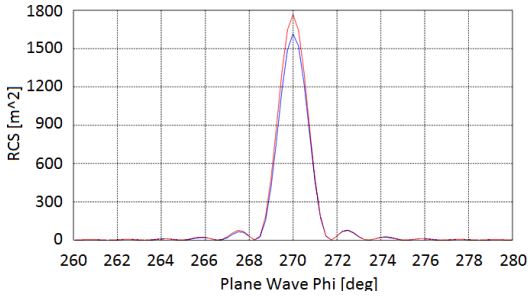

Figure 2.62: Radar Cross Section of the smoothed sponson geometry of the realistic tank model without small features, at $1GHz$. Red and blue lines represent $0°$ and $5°$ of tilt, respectively. ($\theta = 90°$).

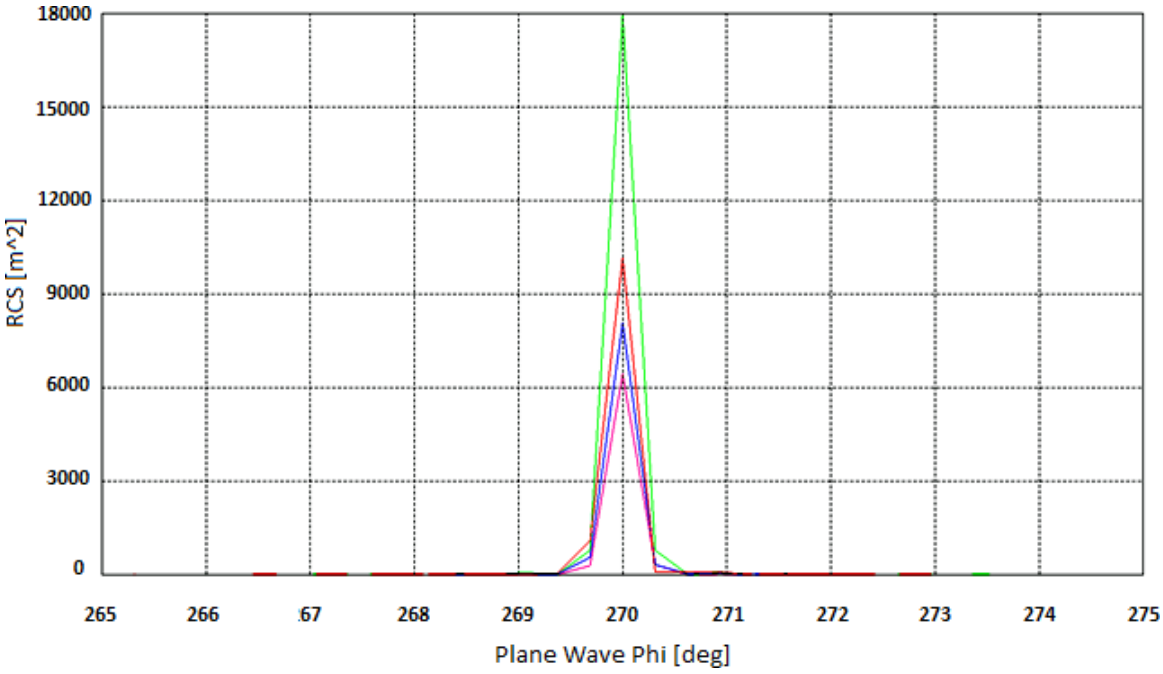

Figure 2.63: Radar Cross Section of the smoothed sponson geometry of the realistic tank model without small features, at $10GHz$. Red, blue, green and pink lines represent $0°$ of tilt for original sponson, $5°$ of tilt for original sponson, $0°$ of tilt for smoothed sponson, $5°$ of tilt for smoothed sponson, respectively. ($\theta = 90°$).

reflections on large smooth faces. Also, all the analyses in this section have been done for the illumination angle $\theta = 90^\circ$ and tilting the faces may cause higher values for illuminations angles with theta-wise elevation. In conclusion, considering these trade-off's, shaping the parts of the geometry that causing excessive reflection is not a feasible radar cross section method for the tank.

2.7.2. Coating

One of the most popular ways to reduce the radar cross section levels of large objects is coating them with various absorber materials. The idea behind of coating is increasing the attenuation rate of radar waves when they hit the object of interest. This may reduce the reflected power and therefore the radar cross section of the object. The materials which attenuate the electromagnetic energy are called absorbers in electromagnetic realm.

Absorbers are used in a wide range of applications to eliminate stray or unwanted radiation that could interfere with a system's operation [20]. Absorbers can be used externally to reduce the reflection from or transmission to particular objects and can also be used internally to reduce oscillations caused by cavity resonance. They can also be used to recreate a free-space environment by eliminating reflections in an anechoic chamber.

Absorbers can take many different physical forms including flexible elastromers or foam or rigid epoxy or plastics. There are absorbers in several forms such as magnetic, dielectric or moldable absorbers. In this section, a both magnetic and dielectric absorber will be applied to the parts of the base tank model which causes excessive reflection as coating. The mentioned parts can be seen in Figure 2.64.

Base Model with Coating

In this section, the base tank model with coatings on the surfaces pointed in Figure 2.64 will be analyzed for its radar cross section behavior and the effects of the coating will be investigated. The coating material will be used is both magnetic and dielectric

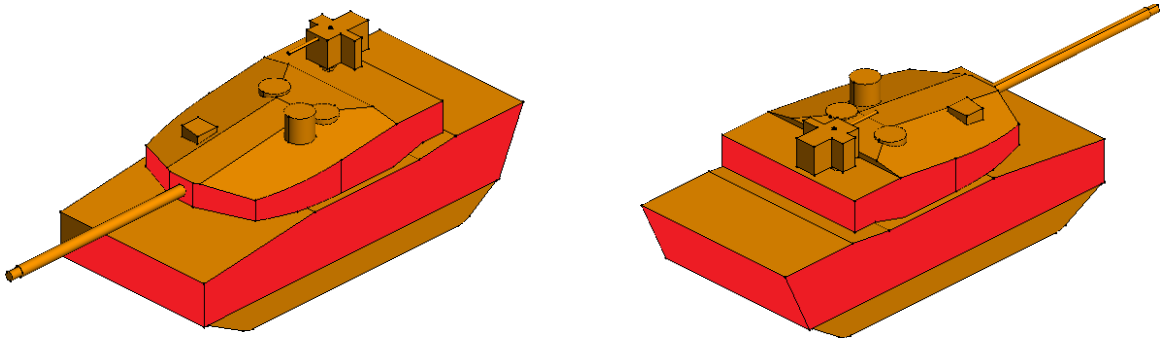

Figure 2.64: The Base Model of the tank indicating the potential surfaces (red ones) that might cause excessive reflection.

with relative permittivity of $\epsilon_r = 8.2$, loss tangent of $\tan\delta_e = 0.2$, relative permeability of $\mu_r = 1.5$, and magnetic loss tangent of $\tan\delta_\mu = 0.4$. These material properties are originated from publication [6]. However, for our simulations material properties will be rougher and assumed to be frequency-independent. It is normally quite frequency-dependent. The thickness of the material will be $5cm$ at simulations.

The reflectivity of the original material is given in the Figure 2.65 as it is available at [6]. Nevertheless, the given reflectivity of the material is ambiguous.

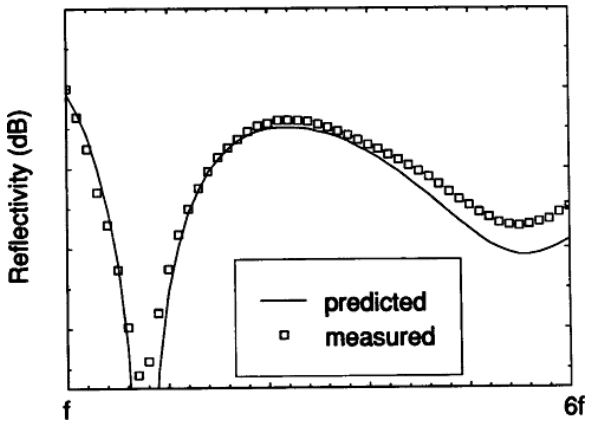

Figure 2.65: The reflectivity of the original material from [6] which is used as a coating material for the base model.

In Figures 2.66 to 2.68, the radar cross section levels of coated and non-coated

versions of the base model can be seen. The highest RCS values have been observed at the angles where normal incidence occurred ($\phi = 90°$) and noticeable reduction has been observed for ($\phi = 90°$,$\theta = 90°$) case. Besides this, when the illumination was elevated for 10°, RCS of the not-coated model decreased halfway in general. However, coating could not provide reduction in a wide-band fashion.

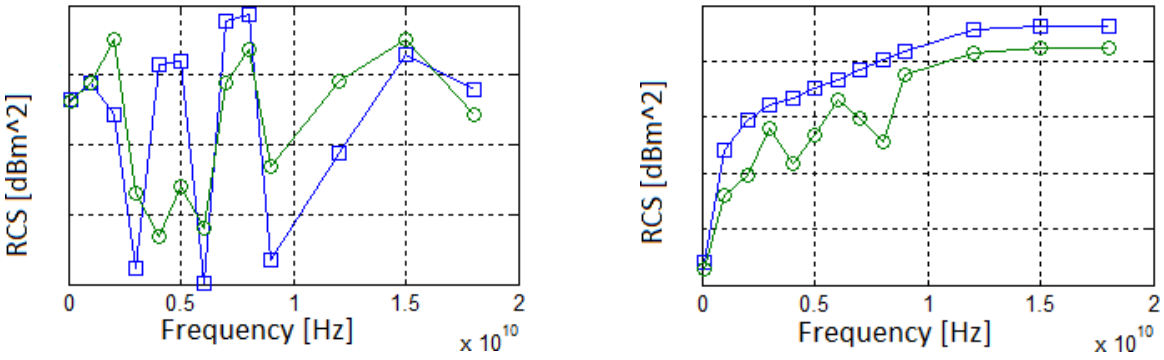

Figure 2.66: The Monostatic RCS levels of the base model with (green lines) an without (blue lines) for illumination angles $\phi = 90$ and $\theta = 80$ (Fig. on the left side), $\theta = 90$ (Fig. on the right side).

For the illumination case where $\phi = 60$, RCS levels have not changed noticeably with both illumination angles. Even though, at that range this slight difference is not significant, for $\theta = 90°$ case RCS level with coating was even higher than not-coated case.

Lastly, for the last illumination case where $\phi = 30$, with both of the elevation angles RCS levels of the coated case was in a decreasing fashion. On the other hand, the difference was still not significant.

Conclusion

In this section, as an example of RCS reduction with radar absorber materials on large platform, a tank with and without coating applied has been investigated for its radar cross section behavior. Even though, the material properties were ambiguous and just a few of the possible illumination angles were simulated, reductions in radar cross

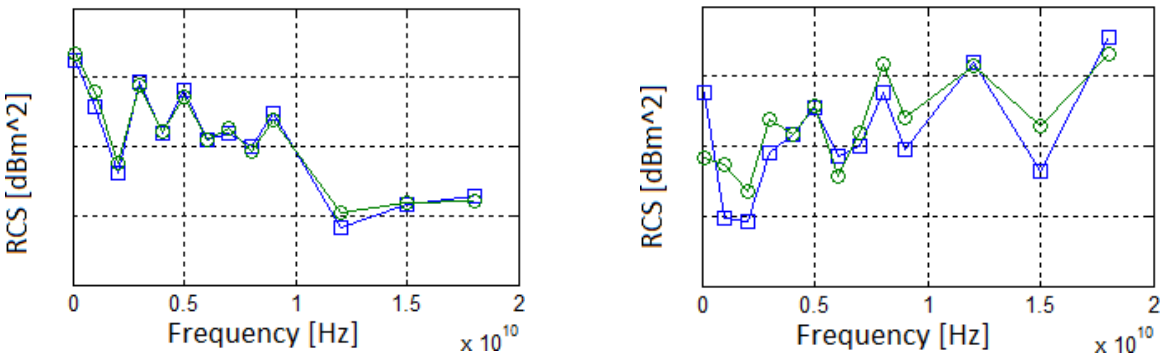

Figure 2.67: The Monostatic RCS levels of the base model with (green lines) an without (blue lines) for illumination angles $\phi = 60$ and $\theta = 80$ (Fig. on the left side), $\theta = 90$ (Fig. on the right side).

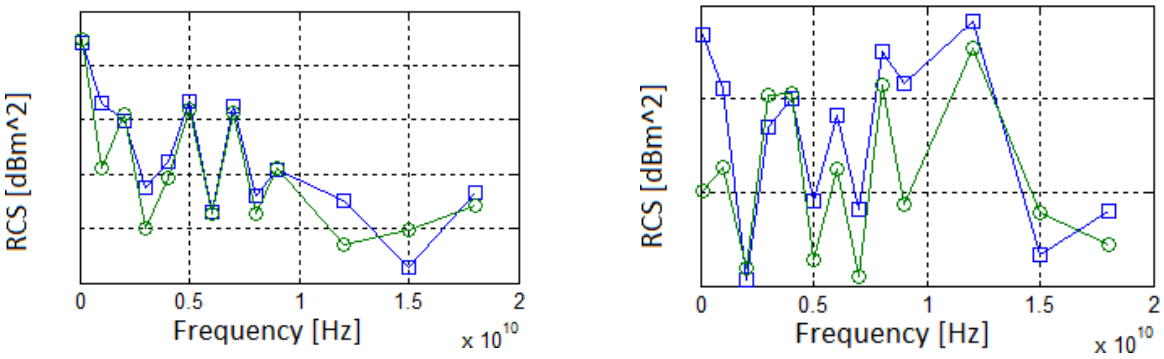

Figure 2.68: The Monostatic RCS levels of the base model with (green lines) an without (blue lines) for illumination angles $\phi = 30$ and $\theta = 80$ (Fig. on the left side), $\theta = 90$ (Fig. on the right side).

section levels has been observed. It was shown that using proper coating materials with known electrical and magnetic properties, it is possible to reduce radar cross section levels at large platforms such as the tank we analyzed.

Chapter 3

Antenna Analyses

This chapter presents simulations of a broadband Very High Frequency antenna, which is manufactured by Comrod Communication ASA, called VHF30512CEF. Firstly, to understand general properties of dipole antennas some simulations on basic linear wire dipole antennas will be held to provide a path to create a realistic model and to make results of the simulations accurate. After that, linear wire antenna models will be created and simulations with these models have been done. For simulations software, EMSS FEKO, Ansoft HFSS, and CST MICROWAVE STUDIO (MWS) have been used.

3.1. Antennas

3.2. Linear Wire Dipole Antennas

In this section, to understand the behavior of dipole antennas at different configurations, several properties such as current distributions of different wire lengths, the relation between currents and radiated fields, the affects of moving the source position will be investigated.

3.2.1. Current Distributions on Linear Wire Dipole Antennas

Considering the fact that an antenna is an electrical device which converts electric currents into electromagnetic radiation, and vice versa. It is convenient to start with investigating the currents on a basic antenna. The behavior of currents distributed on a linear wire dipole antennas at free space can be found in Figure 3.1 from [7].

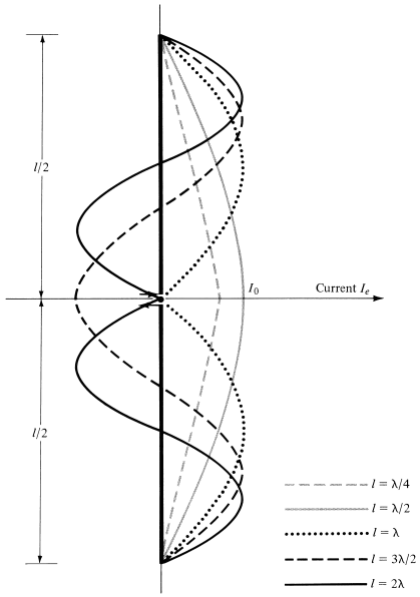

Figure 3.1: Current distributions along the length of a center-fed linear wire antenna from [7]

3.2.2. Radiation Patterns at Different Wire Lengths

An antenna radiation pattern is defined as "a mathematical function or a graphical representation of the radiation properties of the antenna as a function of space coordinates". Radiation properties could include power flux density, radiation intensity, field strength, directivity, phase or polarization [7].

In this section we wanted to examine radiation patterns of electric fields for dipole antennas at various lengths to obtain a reference for simulations for a realistic antenna

model. To acquire the radiation patterns, instead of changing the wire length, we fixed the length of the wire and made the simulations in a frequency range suitable to lengths we wanted to observe.

Firstly, simulations have been performed at the same frequency with different lengths, but different length plots of the current distributions did not have the same spatial intervals along z-axis which the wire antenna lies. To obtain results with the same intervals as in Figure 3.1, Simulation frequencies were changed instead of changing the wire length. $l = 3m$ was selected as the wire length and simulations were performed between $25MHz$ to $200MHz$ to obtain current distributions on wire at specific wire lengths which are shown in Table 3.1. Also, wire segment radius was selected as $1cm$ which is assumed to be proper for simulations.

Simulation frequencies were changed instead of changing the wire length. $l = 3m$ was selected as the wire length and simulations were performed between $25MHz$ to $200MHz$ to obtain current distributions on wire at specific wire lengths which are shown in Table 3.1.

Table 3.1: Lengths as wavelengths at different frequencies for a $l = 3m$ center-fed wire dipole

l	f (MHz)
$\lambda/4$	25
$\lambda/2$	50
λ	100
$3\lambda/2$	150
2λ	200

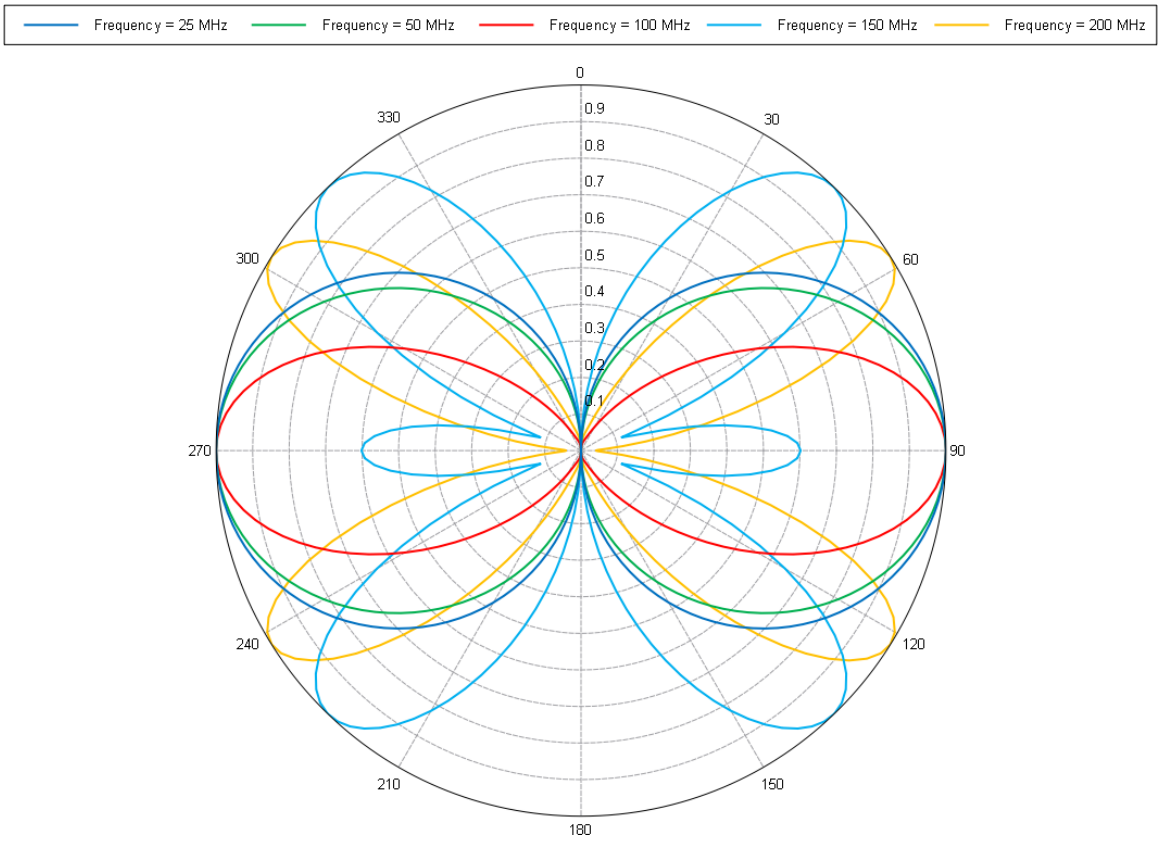

Figure 3.2: Electric Field Radiation patterns of a center-fed $l = 3m$ long wire dipole antenna, lying along z-axis, with different wire lengths, polat plot with normalized values and $\phi = 0$.

3.2.3. Changing the Source Position and its Effects on Current Distribution and Radiation Pattern

In the previous sections I used a center-fed dipole antenna which means the source point was in the middle of the wire. For this section I made simulations with antennas fed at different points and tried to observe changes in radiation patterns. I have used the same wire antenna for this section too, but changed the source placement on the wire in the range from bottom to center.

To observe the difference at radiation patterns I plotted directivity patterns (Fig-

ures 3.3(a) to 3.3(f)) at $f = 200MHz$ for each placement. Considering the directivity patterns, to obtain a higher directivity at a certain direction it would be a good practice to move the source on wire at the opposite direction at z-axis.

3.3. Simulations of COMROD VHF30512CEF

In this section a VHF/UHF antenna named COMROD VHF30512CEF which is planned to be placed on the tank of interest is investigated. The manufacturer data which can be found in [8] does not provide enough information to design the antenna model and run simulations. Therefore, with the information provided in previous section and available manufacturer data a linear wire antenna model will be created and investigated in proceeding sections. In modeling phase of the antenna simulations will be done with FEKO and verified with HFSS and CST MWS[6].

3.3.1. Generating the Antenna Model

COMROD VHF30512CEF antenna has two operation modes; for UHF mode ($116 - 512MHz$) it works as a center-fed dipole and for VHF mode (225-400MHz) it is a tip-fed monopole. The gain to frequency curve from [8] can be found in Figure 3.4.

The gain values in Figure 3.4 are not in dBi's, which is the conventional way. Instead of a isotropic antenna, provided gain is relative to a quarter-wave monopole. Therefore, the superposition of the gain of a quarter wave monopole on an $3m \times 3m$ ground plane (available in Figure 3.5) and provided gain would be equal to the antenna gain relative to an isotropic antenna or in dBi.

At manufacturer datasheet it is also not clear that if the provided antenna gain is directive or realized gain. When directive gain includes the impedance mismatch, realized gain does not. Considering the voltage standing wave ratio for the antenna (see Figure 3.6) is also provided with antenna gain, the provided gain will be considered

[6]This part of the study was completed in collaboration with Dr. İbrahim Türer who works at OTOKAR AŞ and based on his work [21].

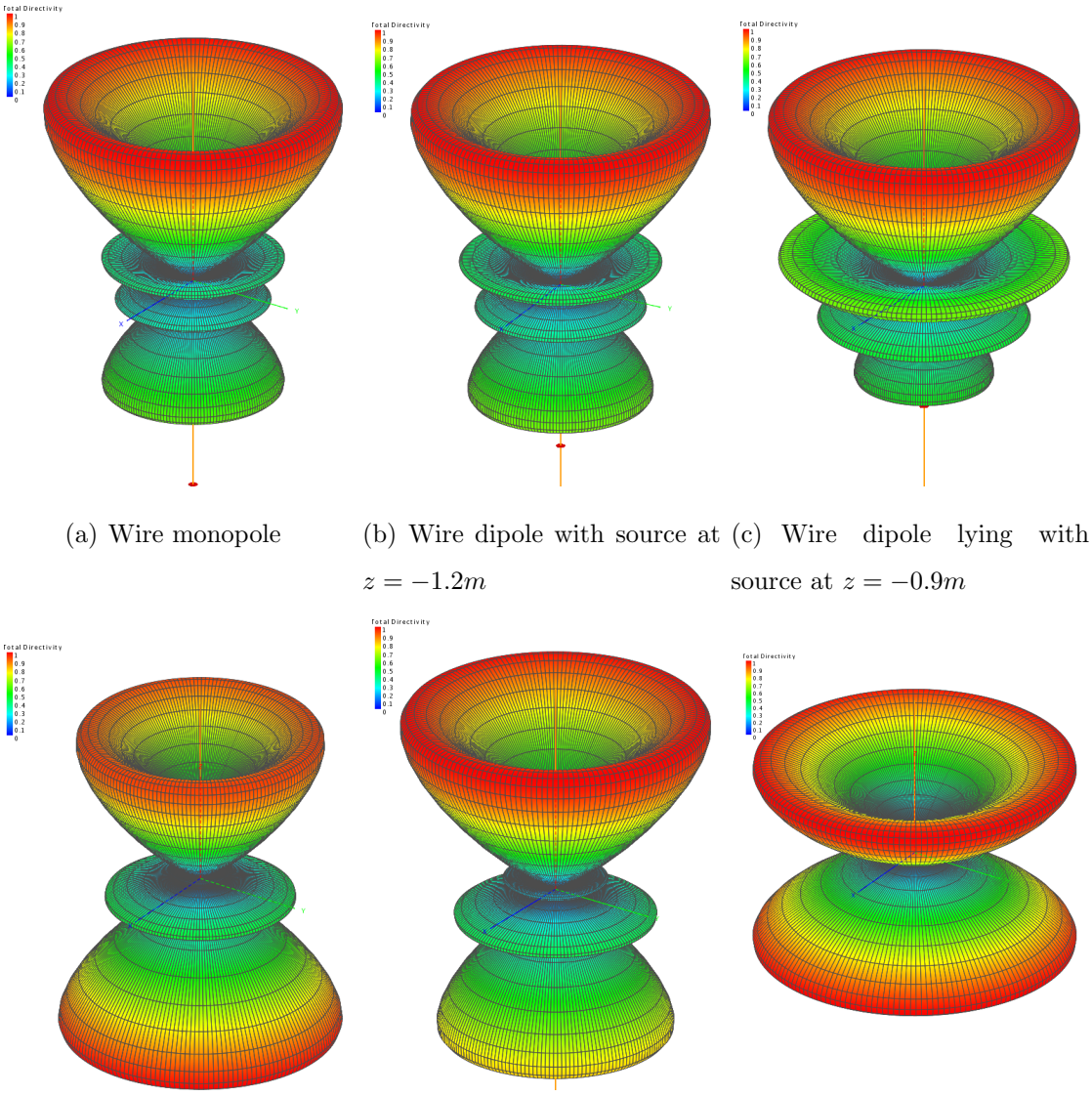

(a) Wire monopole

(b) Wire dipole with source at $z = -1.2m$

(c) Wire dipole lying with source at $z = -0.9m$

(d) Wire dipole with source at $z = -0.6m$

(e) Wire dipole with source at $z = -0.3m$

(f) Center-fed wire dipole

Figure 3.3: Directivity Patterns of $l = 3m$ long wire monopole and dipoles lying along z-axis at $f = 200MHz$

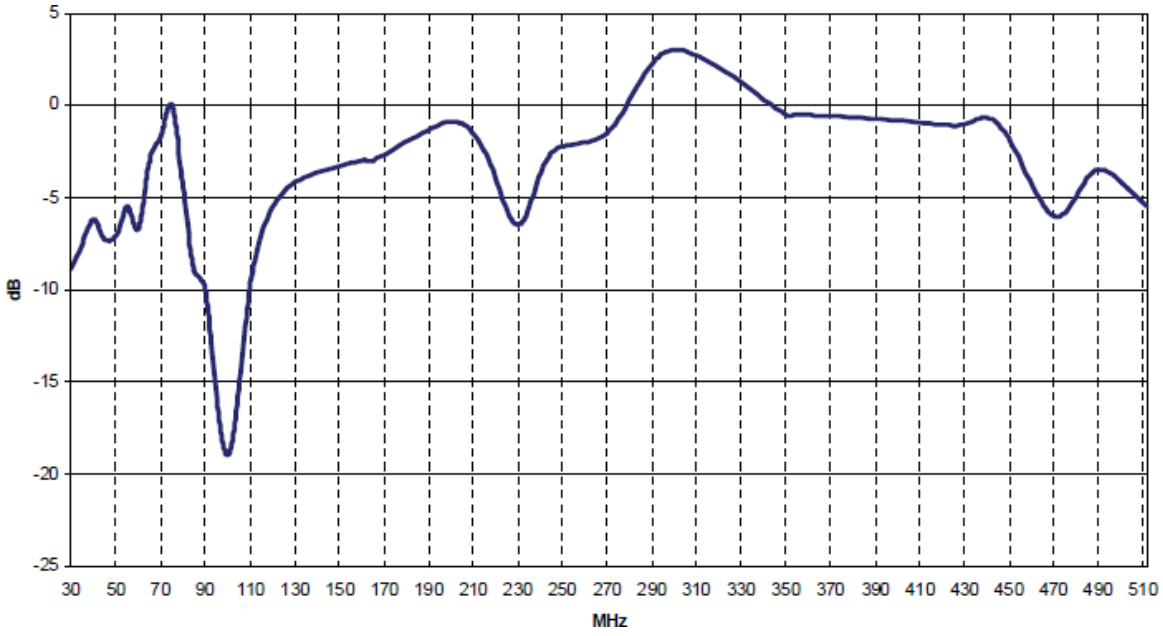

Figure 3.4: Antenna gain relative to 1/4 whip provided by the manufacturer for COMROD VHF30512CEF Antenna from [8]. Antenna is said to be installed in the center of a $3m \times 3m$ ground plane

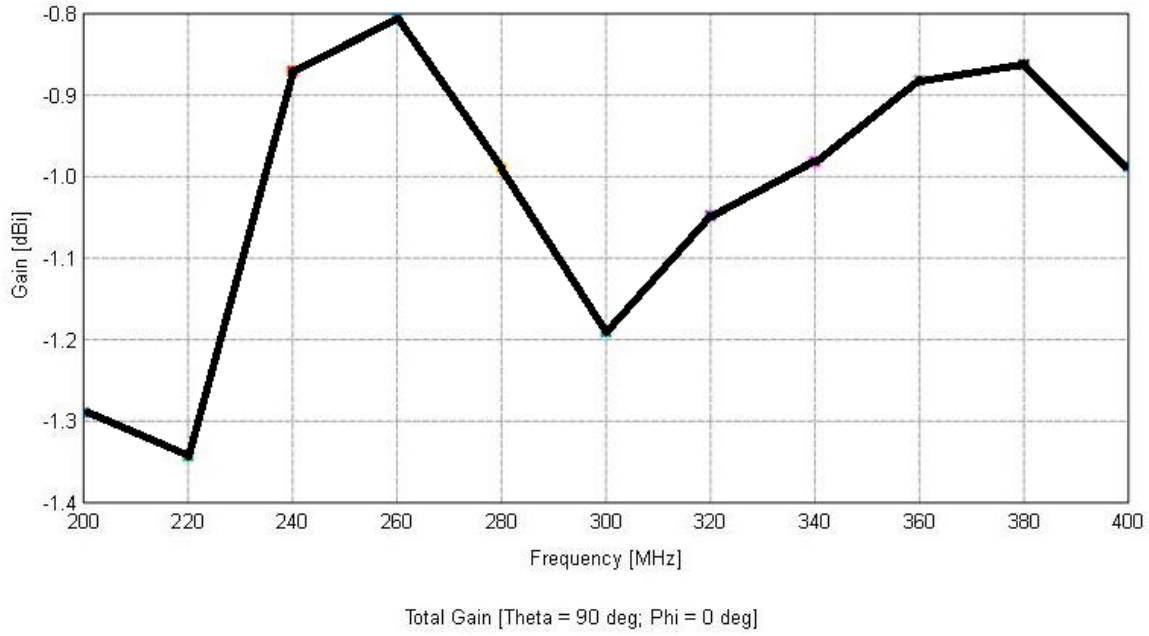

Figure 3.5: The gain of a quarterwave monopole antenna on $3m \times 3m$ ground plane simulated using FEKO

as directive gain.

The realized gain of the antenna can be calculated with the following equation:

$$G_R = G_{\lambda/4} + AF_{\lambda/4} - TL \tag{3.1}$$

where G_R, $G_{\lambda/4}$, AF and TL are realized gain in dBi, gain relative to quarter wave monopole in dBi, adjustment factor (the gain of quarter-wave monopole on $3m \times 3m$ ground) and transmission loss (obtained from VSWR curve), respectively.

$$TL(dB) = 10 \log 1 - \Gamma^2 \tag{3.2}$$

$$\Gamma = \frac{VSWR - 1}{VSWR + 1} \tag{3.3}$$

The calculated realized gain values using Equations 3.1, 3.2 and 3.3 can found in Table 3.2.

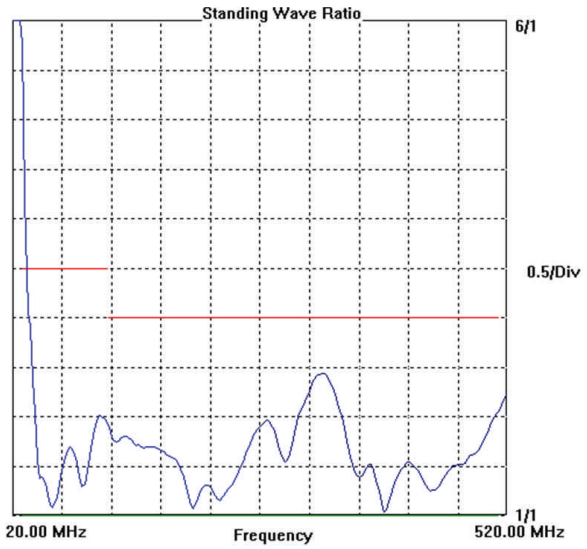

Figure 3.6: VSWR Curve provided by the manufacturer for COMROD VHF30512CEF Antenna from [8].

Table 3.2: The realized antenna gain values of COMROD VHF30512CEF Antenna obtained using Equation 3.1.

Frequency (MHz)	$G_{\lambda/4}$	G_i	TL	G_R (dBi)
225	-4	$-4-1.3$	0.9	-6.2
250	-2.4	$-2.4-0.85$	0.3	-3.55
300	3	$3-1.2$	0.18	1.62
350	-1	-1.95	0.51	-2.46
400	-2	$-2-1$	0.9	-3.9

In preceding sections linear wire dipole antennas have been investigated for several properties to construct a base for designing the antenna model. With this experience, a linear wire dipole antenna which has similar gain pattern with Figure 3.4 designed by trial and error. Firstly, a linear wire antenna on a $3m \times 3m$ ground plane has been modeled as in Figure 3.8 with CAD interface of FEKO then a similar model has been created with CAD interface of HFSS and CST MWS. In Figure 3.7 the realized gain of the designed antenna models on $3m \times 3m$ ground plane from both FEKO and HFSS can be seen.

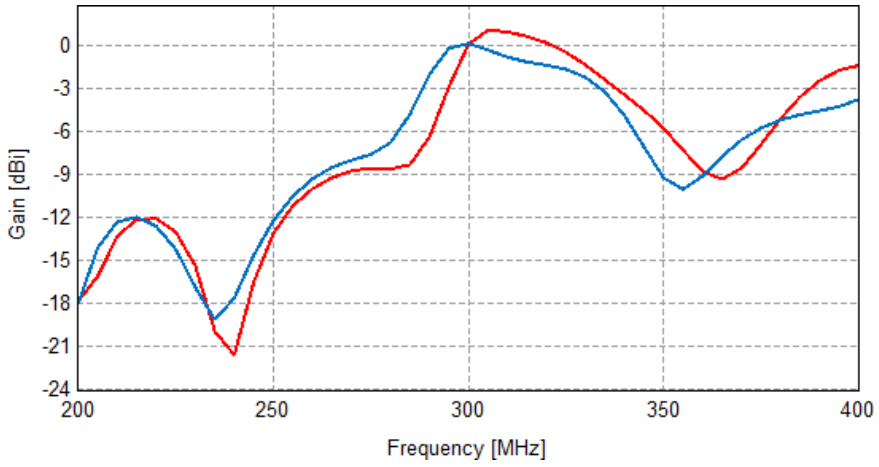

Figure 3.7: The realized gain of the models of COMROD VHF30512CEF antenna on $3m \times 3m$ ground plane. Blue and red lines represent the results from FEKO and HFSS, respectively. ($\theta = 90°$ and $\phi = 0°$)

The results in Figure 3.7 are similar to the ones the manufacturer provided in pattern but have lower gain values. In Figure 3.9 the realized gain of the designed antenna models on infinite ground plane from both FEKO and HFSS can be found. As might be expected the gain values in Figure 3.9 are relatively higher this time.

Considering the simulated gain and the gain which manufacturer provided are quite similar in pattern for $\theta = 90°$ case -which is the only data the manufacturer provided-, the gain patterns might be obtained from the models. In Figures 3.11(a) to 3.12(c) the normalized gain patterns and in Figures 3.10(a) to 3.10(c) the normalized

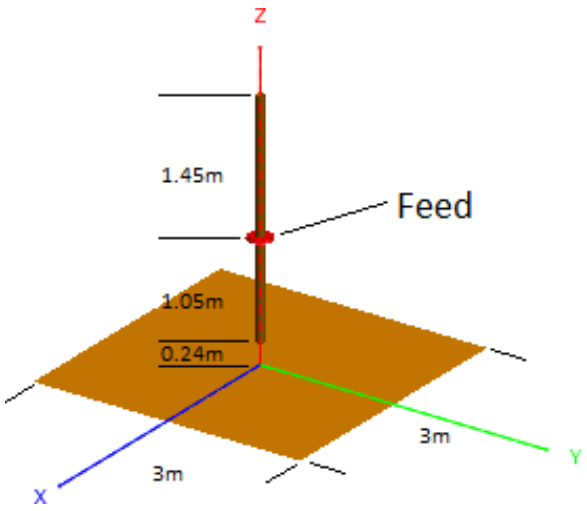

Figure 3.8: The FEKO model used to simulate COMROD VHF30512CEF antenna with dimensions. Wire radius is $1cm$ and the source is placed %42 upwards from the bottom.

electric field patterns at three frequencies can be found, respectively. Because, in Figures 3.7 and 3.9, results from FEKO and HFSS were overlapping, after this point just the results from FEKO will be provided in this section.

As can be seen in Figure 3.10, because the ground plane is finite, there is electric field radiation under the ground plane. If an infinite ground plane has been simulated a pattern with higher values on the upper side of ground plane would have been obtained and there would not be any radiation under the ground plane, (see Figure 3.13)

To calculate the electric field values of the antenna at far field region properly, it is necessary to consider the difference between the simulated gain values and the gain provided by the manufacturer at the operation frequency of interest. As mentioned before the gain values provided by the manufacturer are realized gain values which matching losses are already considered. The electric field at far field region can be calculated via Equation 3.4

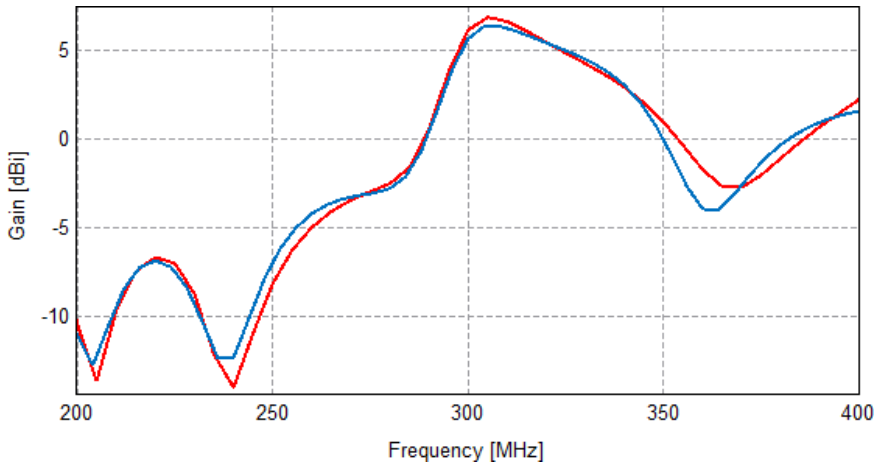

Figure 3.9: The realized gain of the models of COMROD VHF30512CEF antenna on infinite ground plane. Blue and red lines represent the results from FEKO and HFSS, respectively. ($\theta = 90°$ and $\phi = 0°$)

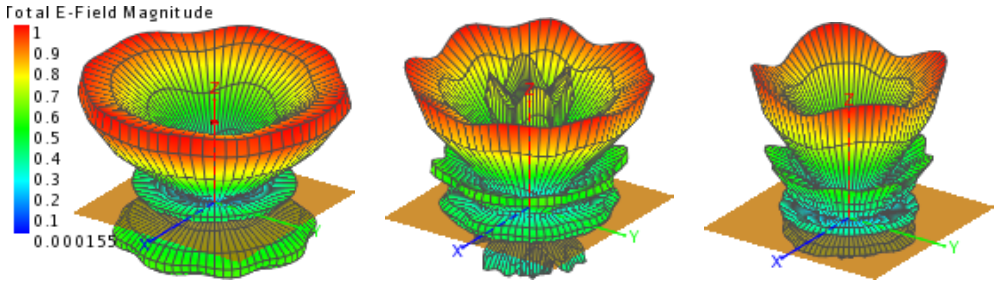

(a) $225MHz$ (b) $300MHz$ (c) $400MHz$

Figure 3.10: Normalized electric field patterns of COMROD VHF30512CEF models on $3m \times 3m$ ground plane.

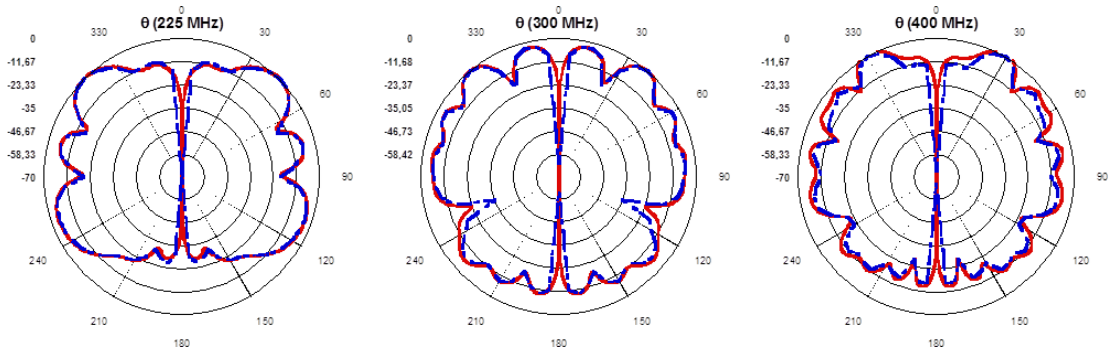

(a) $225MHz$ (b) $300MHz$ (c) $400MHz$

Figure 3.11: Normalized gain patterns of COMROD VHF30512CEF models on $3m \times 3m$ ground plane. ($\phi = 0°$). Red and blue lines represent results obtained using CST MWS and FEKO, respectively.

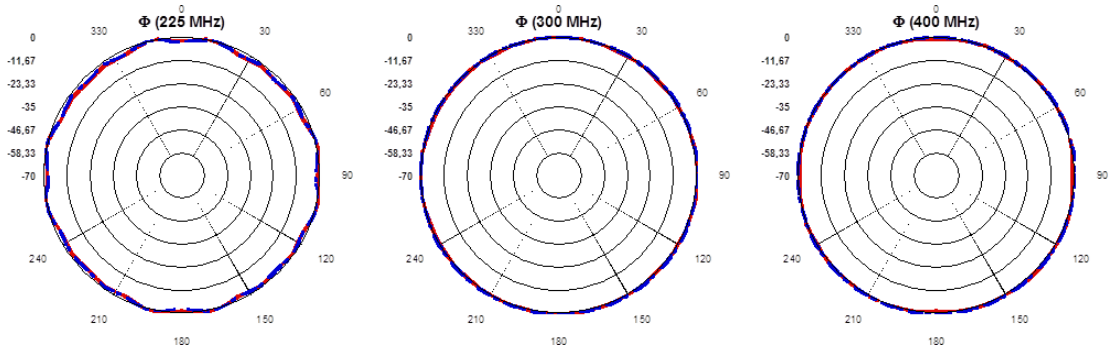

(a) $225MHz$ (b) $300MHz$ (c) $400MHz$

Figure 3.12: Normalized gain patterns of COMROD VHF30512CEF FEKO model on $3m \times 3m$ ground plane. ($\theta = 90°$). Red and blue lines represent results obtained using CST MWS and FEKO, respectively.

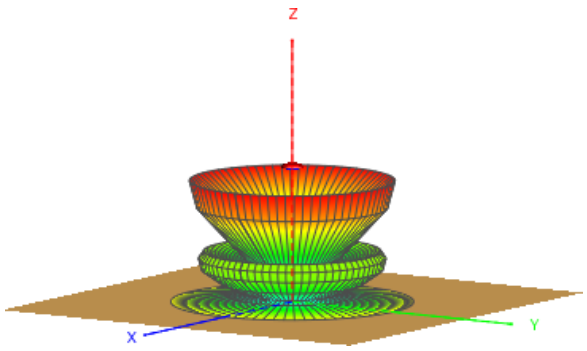

Figure 3.13: Normalized electric field pattern of COMROD VHF30512CEF FEKO model on infinite ground plane at $300MHz$.

$$E(\theta,\phi) = \frac{\sqrt{30P_{in}G(\theta,\phi)}}{r} = \frac{\sqrt{30P_{inc}G_0(\theta,\phi)}}{r} \tag{3.4}$$

where $E(\theta,\phi)$ is electric field at far field region (V/m), P_{in} is feeding power (impedance mismatch is considered), P_{inc} is feeding power (impedance mismatch is not considered), $G(\theta,\phi)$ is directive gain from simulation, $G_0(\theta,\phi)$ is realized gain from manufacturer and r is the distance from antenna. If we feed the antenna with $10W$ and $50W$, we would expect a $10\log 50/10 = 7dB$ difference with same patterns, see Figures 3.14 and 3.15. In cases where realized gain and simulated gain values are different, to calculate valid electric field values feeding power must be increased this way.

3.3.2. Simulations of Antenna Placed on the Tank

In this section electric field patterns for far field region and electric field distributions for near field region of the antenna placed on the tank for two placement scenario will be analyzed. Simulations will have been done at $225MHz$, $300MHz$, and $400MHz$ operating frequencies and to obtain valid electric field values the difference between realized gain and simulated gain values will be considered. In the first placement scenario antenna will be placed on the rear-right corner of the tower with $5cm$ off-set

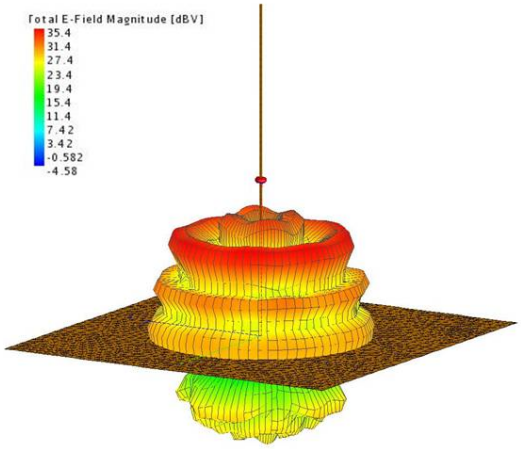

Figure 3.14: Electric field pattern of COMROD VHF30512CEF on $3m \times 3m$ ground plane at far field region with $10W$ feeding power, no mismatch.

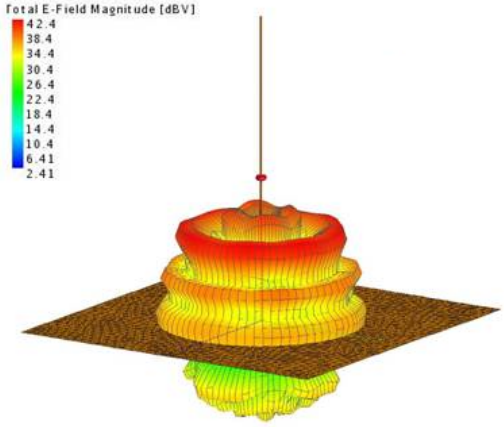

Figure 3.15: Electric field pattern of COMROD VHF30512CEF on $3m \times 3m$ ground plane at far field region with $50W$ feeding power, no mismatch.

both on x and y direction and in the second scenario antenna will be placed on the rear-left with same off-set.

Antenna Placed on the Rear-Right Corner

225 MHz Operation Frequency The simulated gain of the antenna with no mismatch on a $3m \times 3m$ ground plane at $225MHz$ is $-14.1dBi$, (see Figure 3.7) and the realized gain is $-6.2dBi$, (see Table 3.2). To obtain valid electric field values via simulations these difference ($7.9dB$) must be considered by increasing the feeding power to $308W$ from $50W$ which is the maximum feeding power of the antenna in practice. In Figures 3.16(a) to 3.16(c) simulation results a $225MHz$ can be found. It is important to note that the tank model is placed on an infinite ground plane to emulate the real scenario.

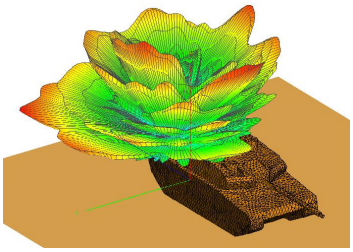

(a) Far field region electric field pattern.

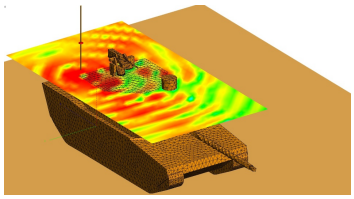

(b) Near field region electric field distribution (at the top plane of the tower).

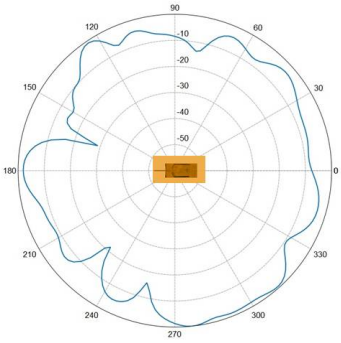

(c) Normalized polar plot of the far field region electric field pattern, $\theta = 90°$.

Figure 3.16: Antenna placed on the rear-right corner of the tower, $f = 225MHz$.

300 MHz Operation Frequency The simulated gain of the antenna with no mismatch on a $3m \times 3m$ ground plane at $300MHz$ is $0dBi$, (see Figure 3.7) and the realized gain is $1.62dBi$, (see Table 3.2). To obtain valid electric field values via simulations these difference ($1.62dB$) must be considered by increasing the feeding power to $72.6W$ from $50W$ which is the maximum feeding power of the antenna in practice. In Figures 3.17(a) to 3.17(c) simulation results a $300MHz$ can be found. It is important to note that the tank model is placed on an infinite ground plane to emulate the real scenario.

400 MHz Operation Frequency The simulated gain of the antenna with no mismatch on a $3m \times 3m$ ground plane at $400MHz$ is $-3.9dBi$, (see Figure 3.7) and the realized gain is also $-3.9dBi$, (see Table 3.2). Because there is no difference, the antenna feed will be $50W$ which is the maximum feeding power of the antenna in practice. In Figures 3.18(a) to 3.18(c) simulation results a $400MHz$ can be found. It is important to note that the tank model is placed on an infinite ground plane to emulate the real scenario.

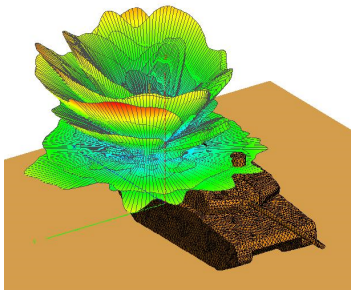

(a) Far field region electric field pattern.

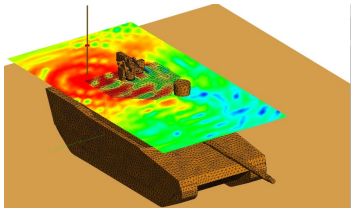

(b) Near field region electric field distribution (at the top plane of the tower).

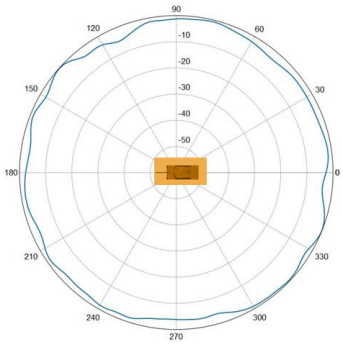

(c) Normalized polar plot of the far field region electric field pattern, $\theta = 90°$.

Figure 3.17: Antenna placed on the rear-right corner of the tower, $f = 300MHz$.

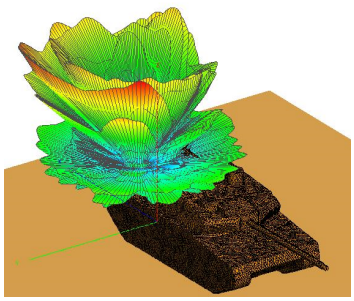

(a) Far field region electric field pattern.

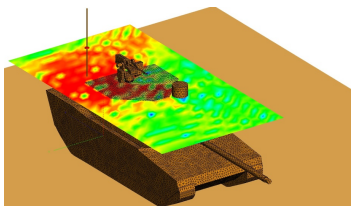

(b) Near field region electric field distribution (at the top plane of the tower).

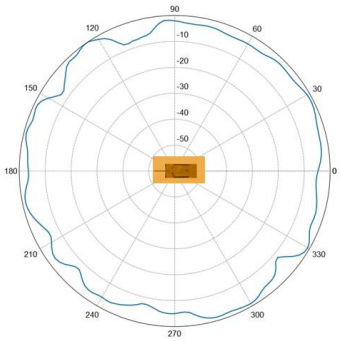

(c) Normalized polar plot of the far field region electric field pattern, $\theta = 90°$.

Figure 3.18: Antenna placed on the rear-right corner of the tower, $f = 400MHz$.

Antenna Placed on the Rear-Left Corner

225 MHz Operation Frequency The simulated gain of the antenna with no mismatch on a $3m \times 3m$ ground plane at $225MHz$ is $-14.1dBi$, (see Figure 3.7) and the realized gain is $-6.2dBi$, (see Table 3.2). To obtain valid electric field values via simulations these difference ($7.9dB$) must be considered by increasing the feeding power to $308W$ from $50W$ which is the maximum feeding power of the antenna in practice. In Figures 3.19(a) to 3.19(c) simulation results a $225MHz$ can be found. It is important to note that the tank model is placed on an infinite ground plane to emulate the real scenario.

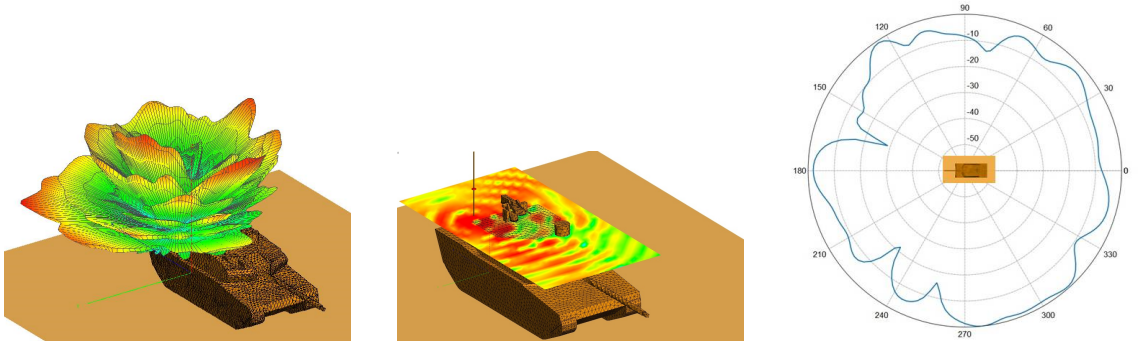

(a) Far field region electric field pattern.

(b) Near field region electric field distribution (at the top plane of the tower).

(c) Normalized polar plot of the far field region electric field pattern, $\theta = 90°$.

Figure 3.19: Antenna placed on the rear-left corner of the tower, $f = 225MHz$.

300 MHz Operation Frequency The simulated gain of the antenna with no mismatch on a $3m \times 3m$ ground plane at $300MHz$ is $0dBi$, (see Figure 3.7) and the realized gain is $1.62dBi$, (see Table 3.2). To obtain valid electric field values via simulations these difference ($1.62dB$) must be considered by increasing the feeding power to $72.6W$ from $50W$ which is the maximum feeding power of the antenna in practice. In Figures 3.20(a) to 3.20(c) simulation results a $300MHz$ can be found. It is important to note that the tank model is placed on an infinite ground plane to

emulate the real scenario.

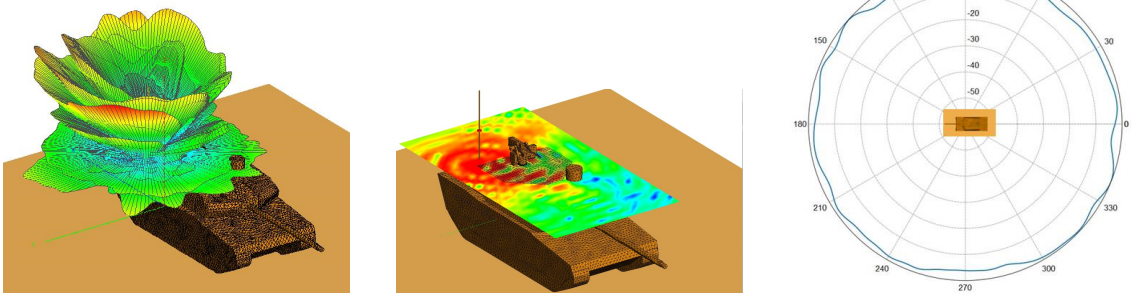

(a) Far field region electric field pattern.

(b) Near field region electric field distribution (at the top plane of the tower).

(c) Normalized polar plot of the far field region electric field pattern, $\theta = 90°$.

Figure 3.20: Antenna placed on the rear-left corner of the tower, $f = 300MHz$.

400 MHz Operation Frequency The simulated gain of the antenna with no mismatch on a $3m \times 3m$ ground plane at $400MHz$ is $-3.9dBi$, (see Figure 3.7) and the realized gain is also $-3.9dBi$, (see Table 3.2). Because there is no difference, the antenna feed will be $50W$ which is the maximum feeding power of the antenna in practice. In Figures 3.21(a) to 3.21(c) simulation results a $400MHz$ can be found. It is important to note that the tank model is placed on an infinite ground plane to emulate the real scenario.

Using the calculated near-field electric field (E) values, it is also possible to calculate power density (S) at any point around the antenna with Equation 3.5.

$$S(W/m^2) = \frac{E^2(V/m)}{377} \tag{3.5}$$

In Table 3.3 electric field and power density values $1m$ away from the antenna can be found for both placement scenarios.

Table 3.3: Electric field and power density values $1m$ away from the COMROD VHF30512CEF antenna placed on the tower of tank model for both placement scenarios.

Placement	Frequency (MHz)	Direction	$E(dBV)$	$S(dBm)$
Rear-Right	225	Front	40.8	45
		Rear	35.3	39.5
		Right	34.3	38.5
		Left	41.4	45.6
	300	Front	41.1	45.3
		Rear	40.8	45
		Right	42.3	46.5
		Left	39.7	43.9
	400	Front	35.3	39.5
		Rear	34.1	38.3
		Right	36.8	41
		Left	33.9	38.1
Rear-Left	225	Front	16.4	20.6
		Rear	29.8	34
		Right	39	43.2
		Left	40.6	44.8
	300	Front	43	47.2
		Rear	40.7	44.9
		Right	40.2	44.4
		Left	42.2	46.4
	400	Front	33.8	38
		Rear	38.4	42.6
		Right	33.8	38
		Left	38.4	42.6

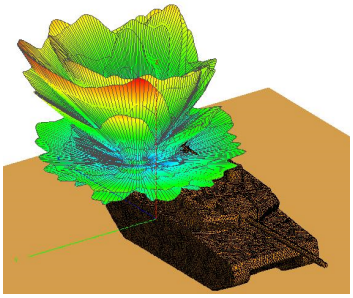

(a) Far field region electric field pattern.

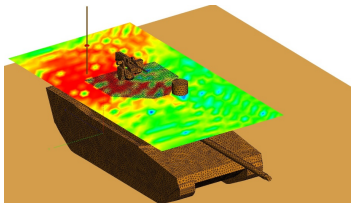

(b) Near field region electric field distribution (at the top plane of the tower).

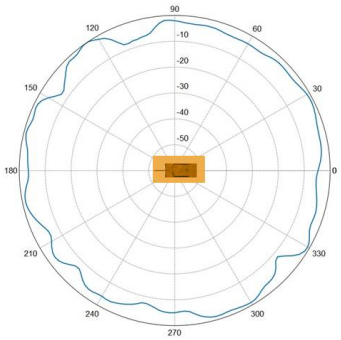

(c) Normalized polar plot of the far field region electric field pattern, $\theta = 90°$.

Figure 3.21: Antenna placed on the rear-left corner of the tower, $f = 400MHz$.

3.3.3. Maximum Antenna Operation Range

To calculate the maximum operation range of the antennas Equation 3.6 will be used

$$P_r = P_t + G_t + G_r - L_g - L_{other} \tag{3.6}$$

where P_r is power at the receiver input (dB), P_t is power at transmitter output (dB), G_t is realized antenna of the transmitting antenna (dB), G_r is realized gain of the receiving antenna (dB), L_g loss from ground wave, and L_{other} is losses from the receiver of the receiving antenna and the transmitter of the transmitting antenna. To calculate L_g, considering the tank is placed on the earth, earth must be modeled properly. The signal radiated from the antenna propagates as ground wave which consist of there components; direct wave, reflected wave, and surface wave [9]. All these components and the polarization must be taken into consideration for realistic earth modeling. Besides these, after $10km$ distance also the roundedness of the earth must be considered. Because the tropospheric scattering starts after $100km$, it is not necessary to take it into consideration. Using the curves in Figure 3.22 which are calculated using Burrows-Gray Model [9], L_g values at frequencies of interest might

be obtained roughly. Weather conditions are ignored in this analysis and not expected to effect distinctively.

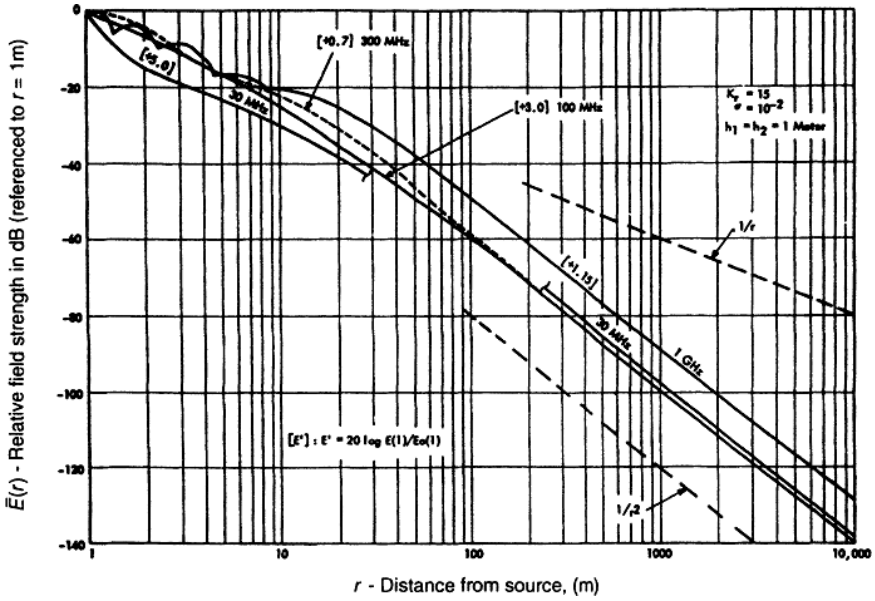

Figure 3.22: Loss curves for realistic earth modelling for vertical polarization from [9].

As can be seen from Figure 3.22, for frequencies 225, 300, and $400MHz$, a loss of $-120dB$ consists at distances 4000, 4500, and $5000km$, respectively. and interested curve decreases inversely proportional with the square of the distance. Maximum operation range was calculated for a $-90dBm$ of receiver sensibility for these there frequencies taking other losses as $2dB$, see Table 3.4.

It can be seen from the Table 3.4 that the maximum operation range of the antenna on the rear-left at $225MHz$ is very low than others especially in front direction. To investigate this problem periscope and/or the remote controlled weapon system (RCWS) were removed and simulations were repeated for these cases, results can be seen in Figure 3.23 and 3.24.

In Figure 3.23 which shows electric field pattern through θ values, all of the lines are very similar. But in Figure 3.24 where electric field pattern was drawn around

Table 3.4: Maximum operation range values of the COMROD VHF30512CEF antenna placed on the tower of tank model for $50W$ feed, $-90dBm$ of receiver sensibility, and both placement scenarios.

Placement	Frequency (MHz)	Direction	Range (km),(isotropic receiver antenna)
Rear-Right	225	Front	14.2
		Rear	10.4
		Right	9.8
		Left	14.6
	300	Front	16.3
		Rear	16.0
		Right	17.4
		Left	15.0
	400	Front	12.9
		Rear	12.1
		Right	14.1
		Left	11.9
Rear-Left	225	Front	3.5
		Rear	7.4
		Right	12.9
		Left	14.1
	300	Front	18.1
		Rear	15.9
		Right	15.5
		Left	17.3
	400	Front	11.9
		Rear	12.3
		Right	11.9
		Left	15.5

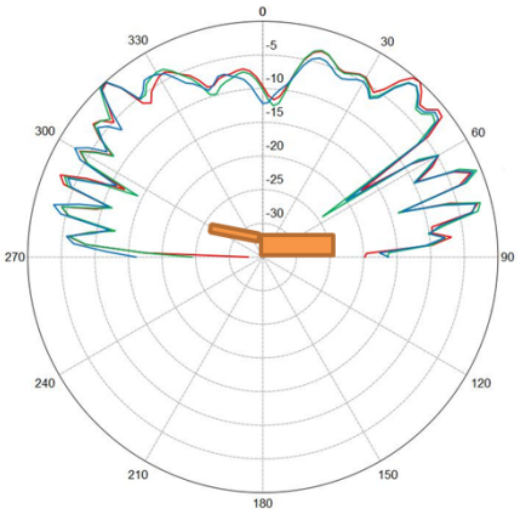

Figure 3.23: Normalized polar plot of the electric field pattern of COMROD VHF30512CEF placed on rear-left corner of the tower at $225MHz$, $\phi = 0°$ and $\theta = 90° : 270°$. Red, Green, and Blue lines represent cases with both periscope and RCWS are available, just RCWS removed, and both removed, respectively.

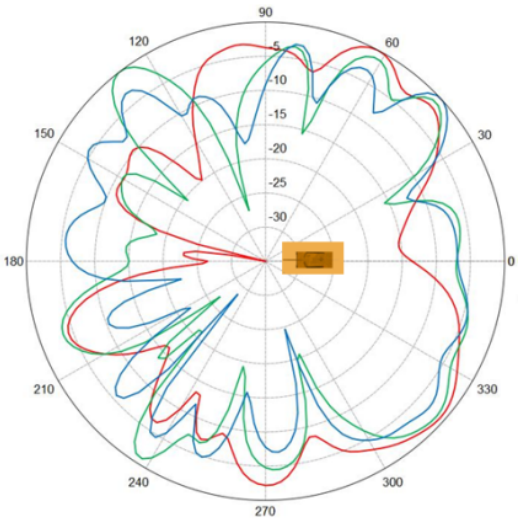

Figure 3.24: Normalized polar plot of the electric field pattern of COMROD VHF30512CEF placed on rear-left corner of the tower at $225MHz$, $\theta = 0°$. Red, Green, and Blue lines represent cases with both periscope and RCWS are available, just RCWS removed, and both removed, respectively.

the azimuth, especially RCWS has distinct destructive effect on electric field pattern. Replacing the antenna or not using this one for longer distance communication would be good practices.

3.3.4. Mutual Coupling

Until now COMROD VHF30512CEF Antenna has been investigated for its design parameters and its placement on the tank model for two cases. In tank design it is planned to place two of this antenna. In this section firstly the mutual coupling between two of our antenna of interest will be investigated and then the most suitable placement scenario on the tank model will be inquired. In this section and proceeding sections simulations will be done with both FEKO and CST MWS software, verified by each other.

When two antennas are positioned near each other, and one or both of them are excited, some energy tends to end up at the other antenna. This interchange of energy is called mutual coupling and is a mechanism of great significance for antenna system performance. It depends on radiation characteristics of the antennas, relative separation between them and their orientation [22].

Mutual Coupling and Scattering Parameters

In a two antenna setup as in Figure 3.25 where the left-antenna has an active source and the right-antenna has a passive source, the left-antenna produces an electromagnetic wave that propagates into free space and a fraction of the radiated energy received by the right-antenna, inducing a current on the element. A part of the induced energy travels toward the passive generator on right-antenna, and another part is reflected and re-radiated. Some of the re-scattered energy will be received by left-antenna again, repeating the cycle [23]. Therefore, the total energy at an observation point would come from both antennas.

Similarly, when both antennas are active, there would be induced energy at both antennas. Then at an observation point the total energy would be come from not

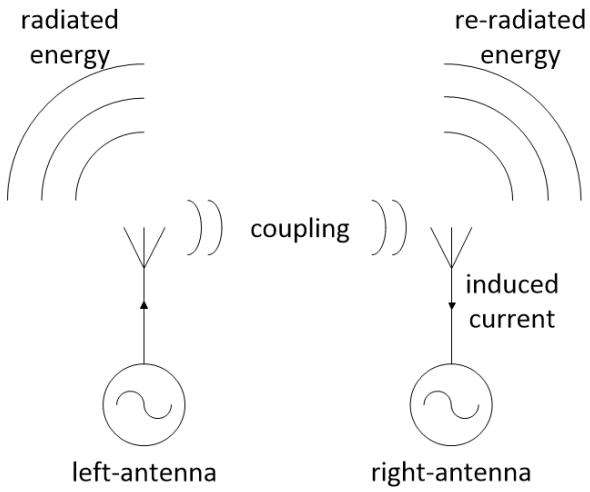

Figure 3.25: Mutual Coupling between two-antennas.

only upon the excitation furnished by active generator but also upon the parasitic excitation as well [7].

To describe the mutual coupling between antennas the Scattering Parameters (or S-parameters) are used. S-parameters explain the rate of the received energy by an antenna of an array of antennas to the energy applied to another antenna of the array. S-parameters are defined as:

$$S_{mn} = \frac{V_m^-}{V_n^+} \tag{3.7}$$

where V_m^- is the voltage received by th antenna m and V_n^+ is the voltage applied to the antenna n. So, S_{mn} denotes the portion of energy applied to antenna n, is received by antenna m. In proceeding sections, because we have a two antenna array S_{21} will be surmounted. Additionally, assuming the antennas are separated by a linear and isotropic (but not necessarily) homogeneous medium or both of them are placed in free space and using the exactly same antennas, our system is reciprocal. Therefore, S_{21} is equal and interchangeable with S_{12}.

Two Antennas at Free-Space

Before investigating the antennas on the tank, a two antenna setup at free space (see Figure 3.26) will be analyzed for mutual coupling.

Figure 3.26: Two COMROD VHF30512CEF antenna setup at free-space for mutual coupling simulations.

In analyses the same models have been used and placed at free space with different distances between. As might be guessed, the longer the distance between the antennas brought the lower coupling (S_{21}) values (except for $D = 5m$, but in general there is a lowering trend with increasing distance), see Figure 3.27.

Two Antennas on Infinite Ground Plane

This time antennas will be installed on an infinite ground plane and their coupling behavior will be investigated. In this setup antennas have a $24cm$ elevation from the infinite ground plane which is the same elevation with the tank setups, see Figure 3.28. It is expected to obtain higher coupling levels than free-space setup considering the reflections from the infinite ground plane.

As expected coupling levels (in Figure 3.29) are higher than the free-space case. Besides, similar to the free-space case, distance and coupling relation has not an exactly proportional correlation. This analysis and the one before have been done to construct a base example placement on the tank simulations. In the antennas on the tank simulations, antennas will neither be on an infinite ground plane nor at free-space.

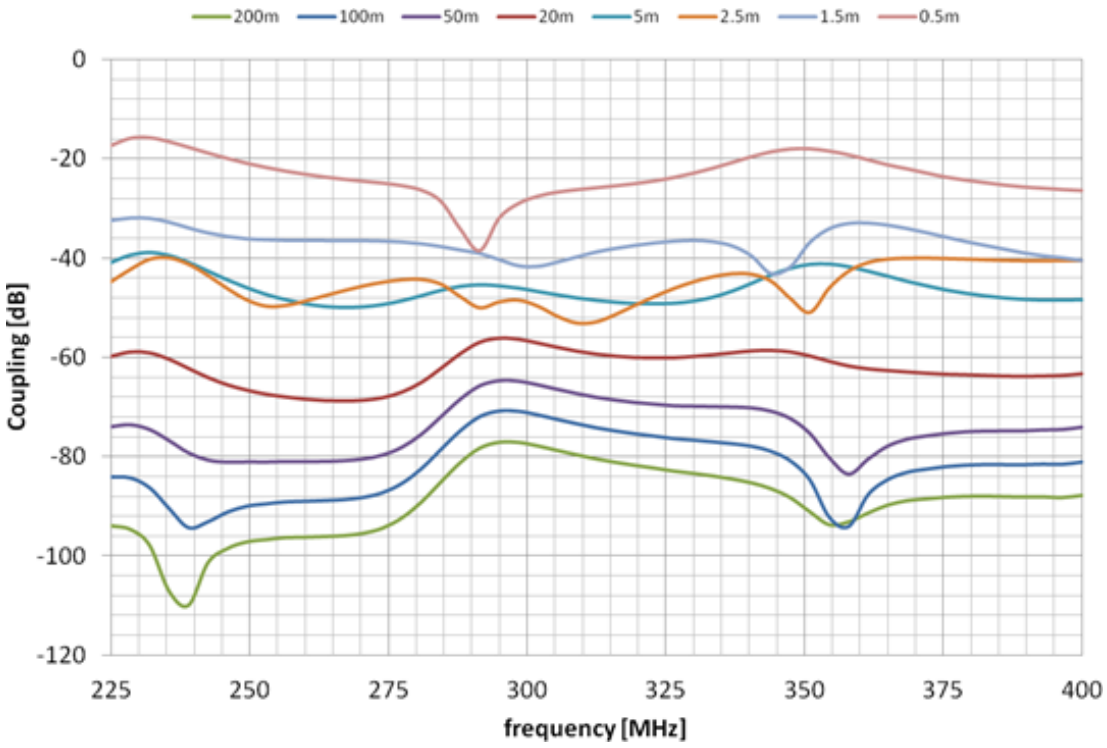

Figure 3.27: Coupling curves (S_{21}) of a two COMROD VHF30512CEF antenna setup at free-space, separated with several distances.

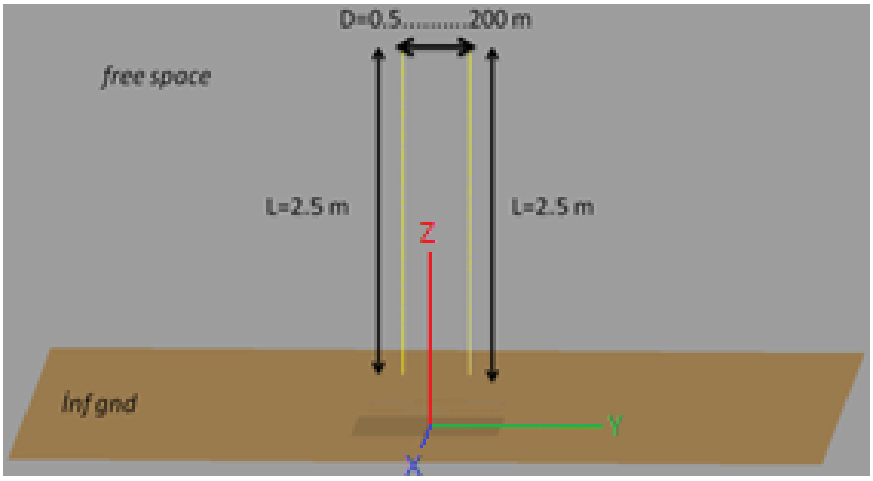

Figure 3.28: Two antennas placed on infinite ground plane.

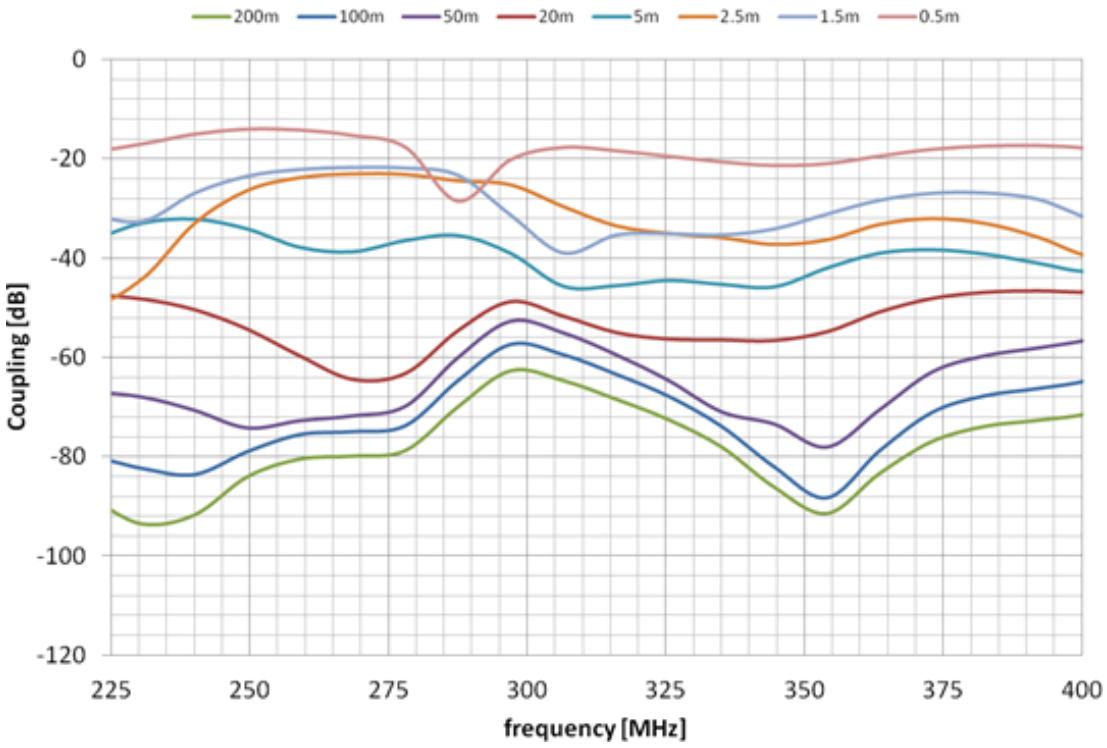

Figure 3.29: Coupling curves (S_{21}) of two COMROD VHF30512CEF antenna setup on infinite ground plane separated with several distances.

3.3.5. Antenna Placement Optimizations

Until this section, COMROD VHF30512CEF antenna has been redesigned because of the lack of information from the manufacturer and the model created has been analyzed for several properties via several scenarios. In this section and ongoing sections the most practically suitable placement scenario will be sought. In the first phase of the tank design these antennas were planned to placed near to the rear corner of the tank. But in our analyses, to interpret the antenna replacement problem widely, antennas will be placed on several locations.

Placing Antennas on the Tower with the Longest Possible Separation

The first scenario will be investigated is placing the antennas on the tower of the tank with the longest possible separation (which is $4.4m$) as in Figure 3.30. If placing the antennas on the tower of tank is the only option, this setup might provide the lowest coupling level.

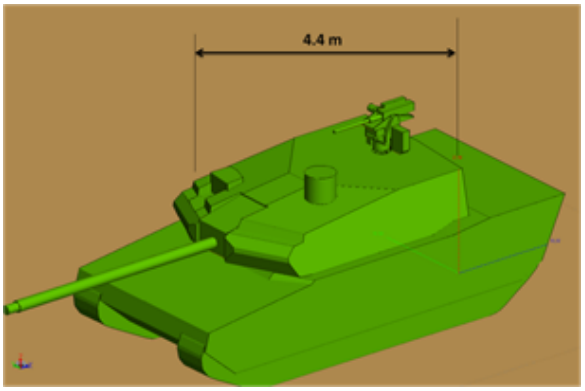

Figure 3.30: Placement of the antennas on the tower of the tank with the longest possible separation.

The simulation of this setup have been done for a frequency range between 225 to $400MHz$. The results (see Figure 3.31) are quite similar with ones from placing the antennas on an infinite ground plane scenario (see Figure 3.29). Even though this is the setup which possibly provides the lowest coupling values between on the tower placements, it is still possible obtain lower coupling levels for the setup at which antennas are placed closer considering the possible reflections from irregularly placed parts on the tower such as the RCWS or the periscope (these reflections may cause destructive interference). In ongoing sections the best placement option will be searched.

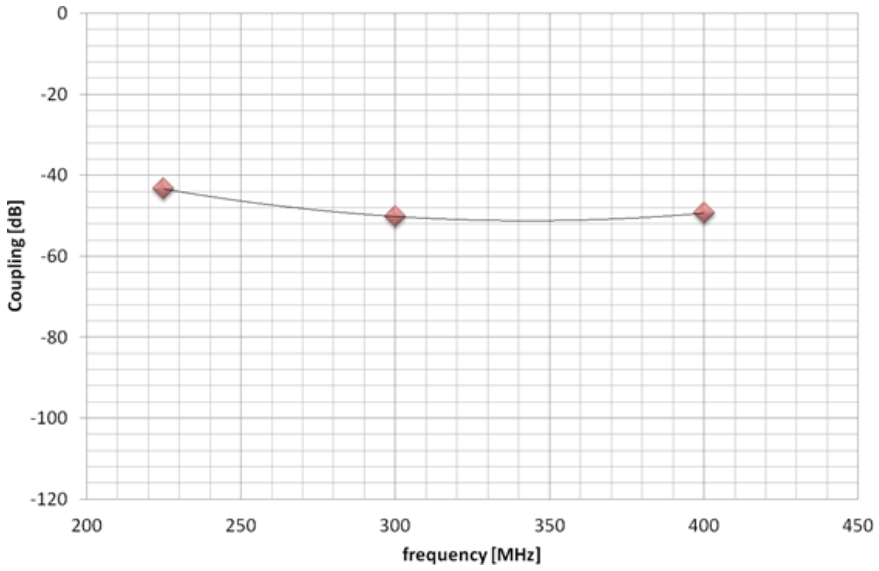

Figure 3.31: Coupling (S_{21}) curve for the antenna placement on the tower of the tank with the longest possible separation between the antennas.

Placing Antennas on the Tank with the Longest Possible Separation

Although it is planned to place antennas on the tower of the tank, it is still a good practice to see what happens when they are placed with the longest possible separation without limiting the possible locations with the tower ($8.4m$), see Figure 3.32. Again it might be expected to obtain coupling levels similar to the results from Figure 3.29.

As expected, this setup has lower S_{21} values (see Figure 3.33) than the one before but the difference is not significant enough considering the unpractical physical placement of the antennas.

Antennas on the Rear Edge of the Tower

Placing antennas on the rear corners of the tank tower is the intuitive beginning scenario for the placement optimizations. In this scenario antennas are placed on the corners with $5cm$ off-sets in both $-x$ and $-y$ axis and there is a $260cm$ gap between the antennas.

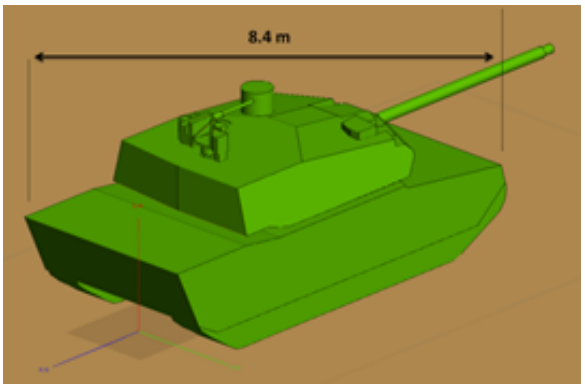

Figure 3.32: Placement of the antennas on the tank with the longest possible seperation.

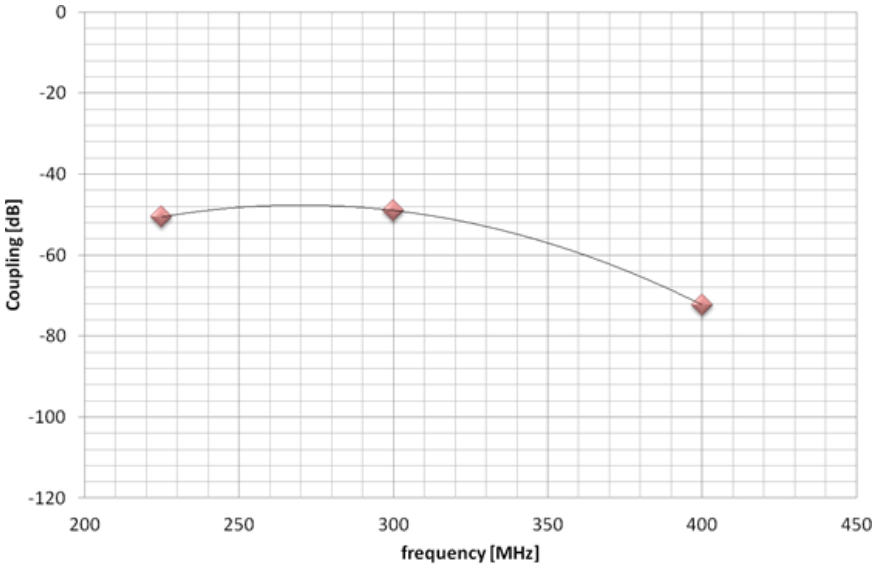

Figure 3.33: Coupling (S_{21}) curve for the antenna placement on the tank with the longest possible separation between the antennas.

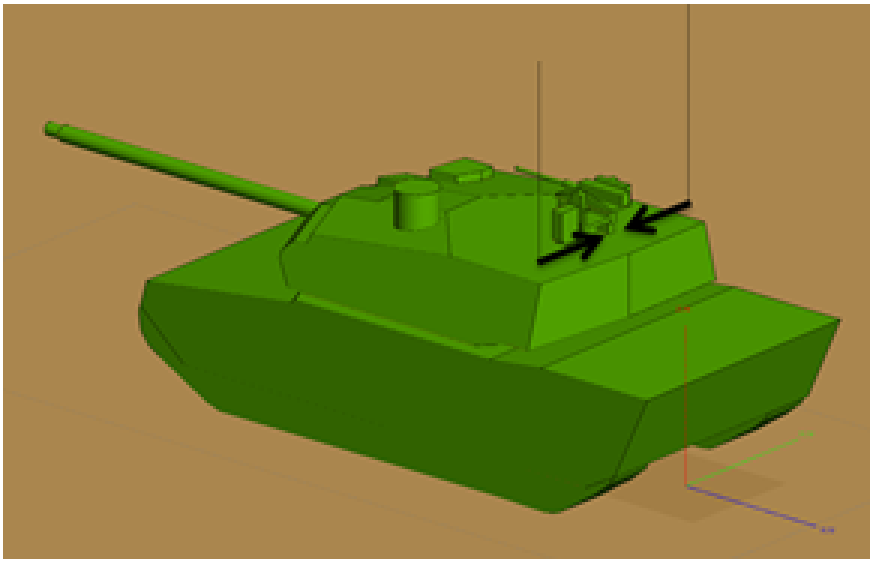

Figure 3.34: Moving the antennas on the rear edge of the tank tower closer in $-y$ axis.

The first analysis is moving the antennas closer in $-y$ axis as in Figure 3.34. The analyses have been done for frequencies $f = 225$, 300, and $400MHz$ as before. As can be seen in Figure 3.35, moving the antennas closer creates nearly $2dB$ difference to the average coupling level until a fast increase begins at the distance $180cm$.

In order to explain the variation of the coupling levels with frequency (or wavelength), same results have been plotted as the distance values in wavelength in Figure 3.36. But considering the other metallic structures on the tower such as the RCWS and periscope, it is not possible to interpret the result as explaining how wavelength effects the results.

Moving the Antennas Forward Another analyses is moving the antennas forward towards the front as in Figure 3.37. This simulation has been done only for $225MHz$ operation frequency and no significant difference has been observed for moving up to $25cm$, see Figure 3.38.

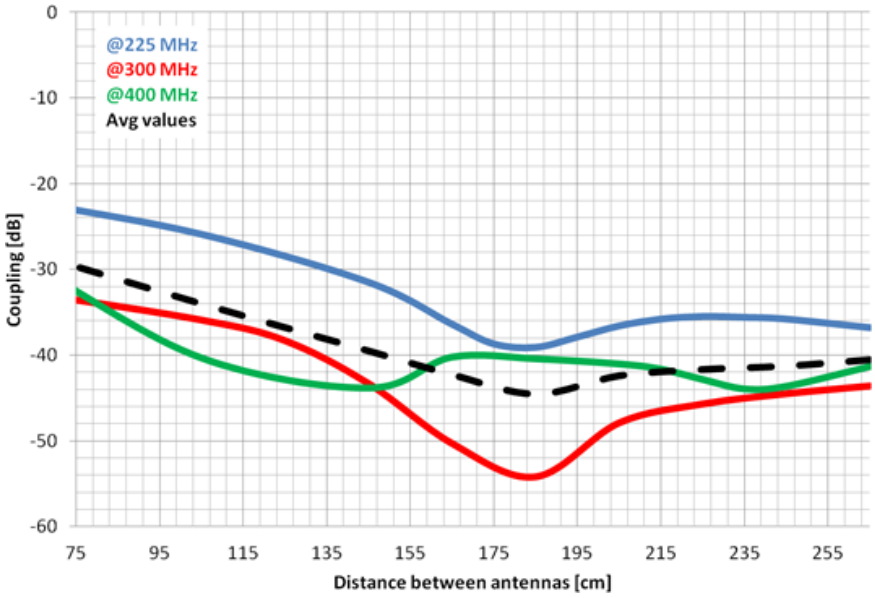

Figure 3.35: Variation in coupling levels (S_{21}) of the two antennas placed on the rear corners of the tank tower by moving them closer in $-y$ axis.

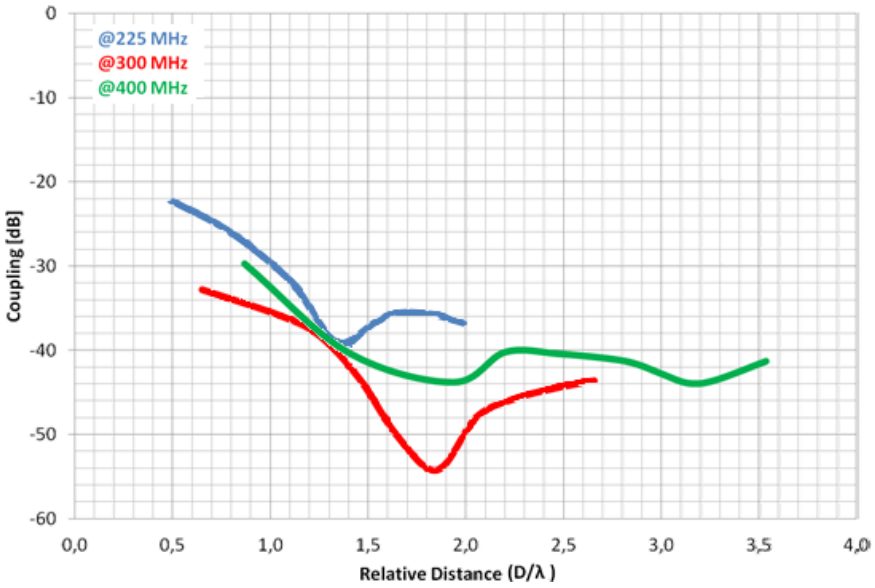

Figure 3.36: Variation in coupling levels (S_{21}) of the two antennas placed on the rear corners of the tank tower by moving them closer in $-y$ axis, distance values are in terms of wavelength.

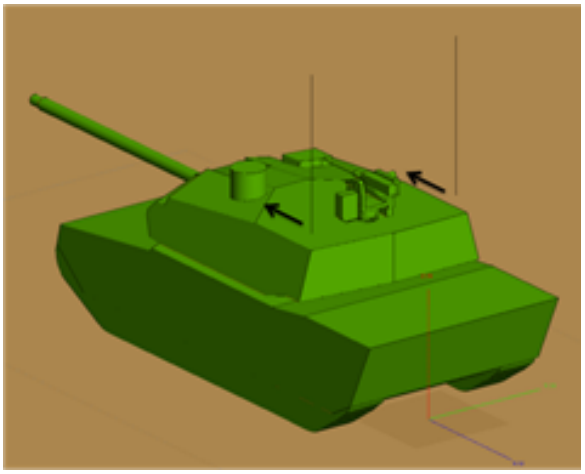

Figure 3.37: Moving the antennas placed on the rear corners of the tank tower forward.

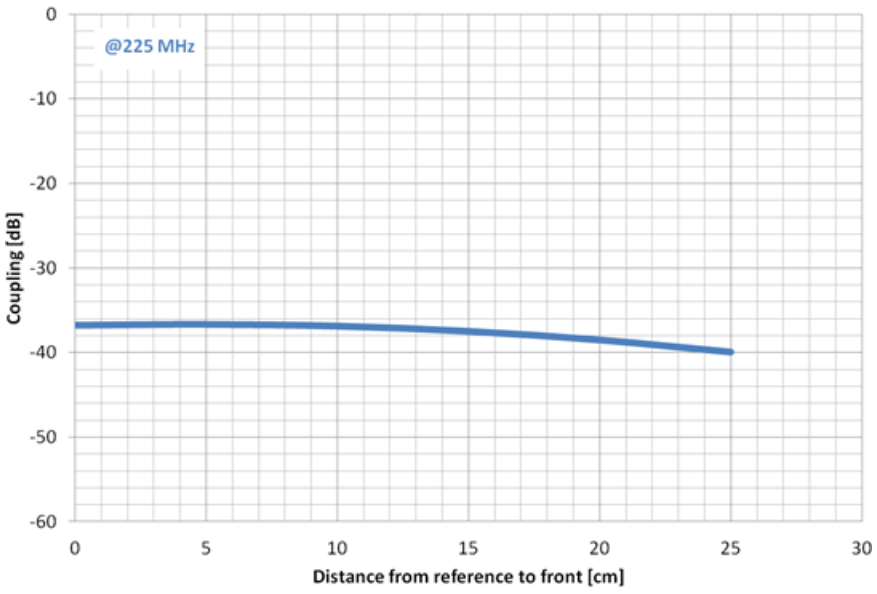

Figure 3.38: Variation in coupling levels (S_{21}) of the two antennas placed on the rear corners of the tank tower by moving them forward in $-x$ axis to the front.

Moving the Antennas Closer In this section as a further attempt the antennas which had been moved forward for $10cm$, were moved closer as can be seen in Figure 3.39.

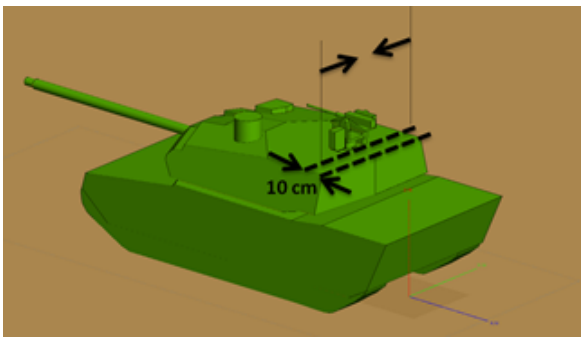

Figure 3.39: Moving the antennas which have been moved forward for $10cm$, closer.

Similarly these simulations have been done just for $225MHz$ and it was still not possible to obtain significant difference between the results, see Figure 3.40.

Effects of RCWS and Periscope on Mutual Coupling The biggest objects on the tower of the tank are the Remote Control Weapon System (RCWS) and the periscope. Now, in order to investigate their effects on coupling levels antennas will be moved closer in $-y$ axis for three cases; with both RCWS and periscope available, only RCWS removed, and both of them removed, see Figure 3.41 and 3.42.

The simulations have been done for 225 and $300MHz$ operation frequencies and as can be seen in Figures 3.43 and 3.44, when coupling levels decreasing via removing the RCWS and periscope at $250MHz$, an increase is observed at $300MHz$. Simulation for $400MHz$ have not been done for these cases but it can be intuitively said that there would be similar behavior as $225MHz$ case.

Considering these are necessary parts, in this section no further investigation has been done for the effects of RCWS and periscope on mutual coupling. In next section a set of analyses will be done around the rear part of the tower with both RCSW and periscope available.

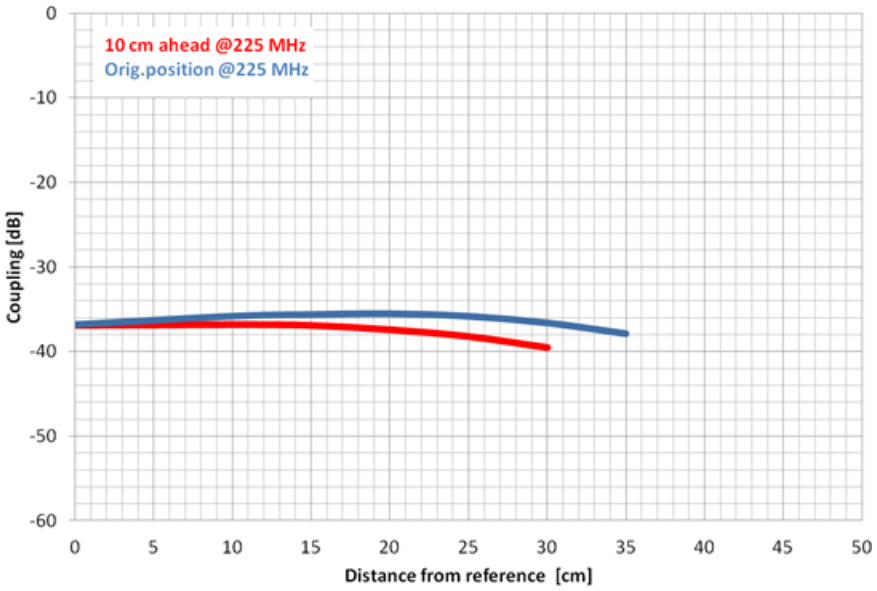

Figure 3.40: Variation in coupling levels (S_{21}) of the two antennas moved them forward in $-x$ axis $10cm$ to the front, by moving them again in $-y$ axis.

Figure 3.41: Base Model without RCWS.

Figure 3.42: Base Model without RCWS and Periscope.

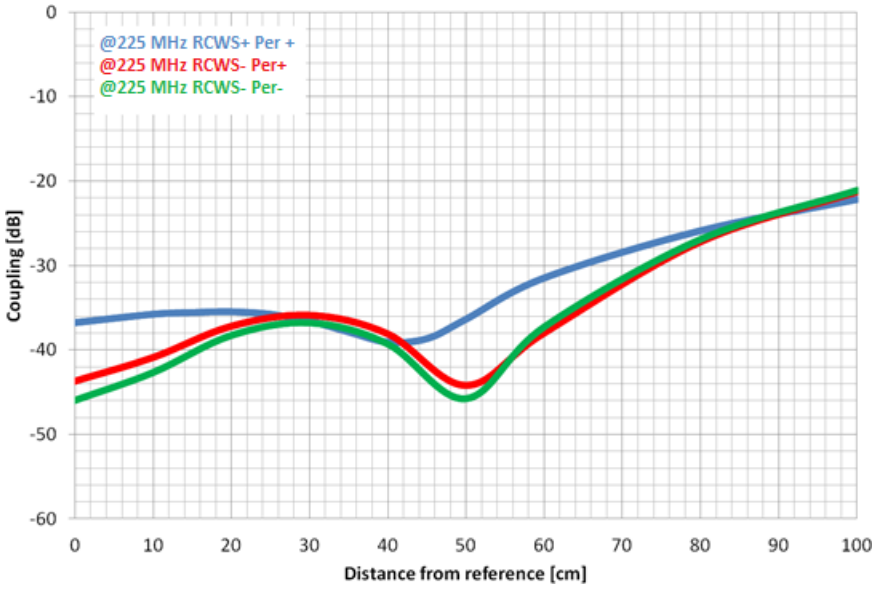

Figure 3.43: Variation in coupling levels (S_{21}) of the two antennas with and without RCWS and/or periscope removed at $f = 225MHz$.

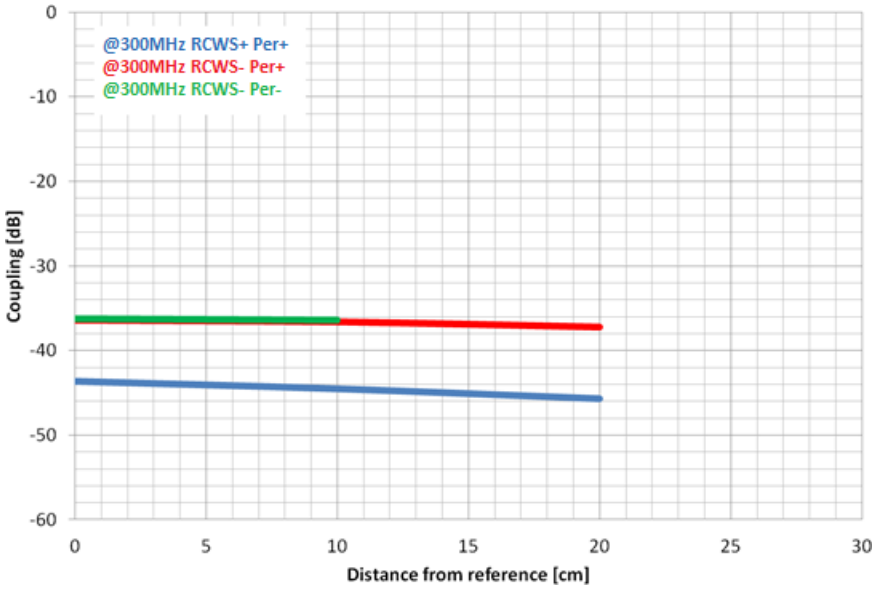

Figure 3.44: Variation in coupling levels (S_{21}) of the two antennas with and without RCWS and/or periscope removed at $f = 300MHz$.

Wide-Band Coupling Optimization Analyses for Antenna Placement Around Rear Part of the Tank Tower

In previous sections several analyses have been done to find an optimal an location pair for antenna placement. However, none of those modifications have provided drastic reduction on coupling levels so far. Additionally, most of those modification have been done without considering mechanical feasibility (as removing the obligatory parts or placing the antennas on unpractical locations).

In this section, the antennas will be placed on several locations (see the numbered optimization grid points in Figure 3.45) which are selected considering mechanical feasibility. When selecting the grid points the sight of the weapon system, advices from the mechanical designers of the tank, and such issues have been taken into account. Besides, until now analyses have been done only for three frequencies but in this section simulations will be performed with a higher frequency resolution.

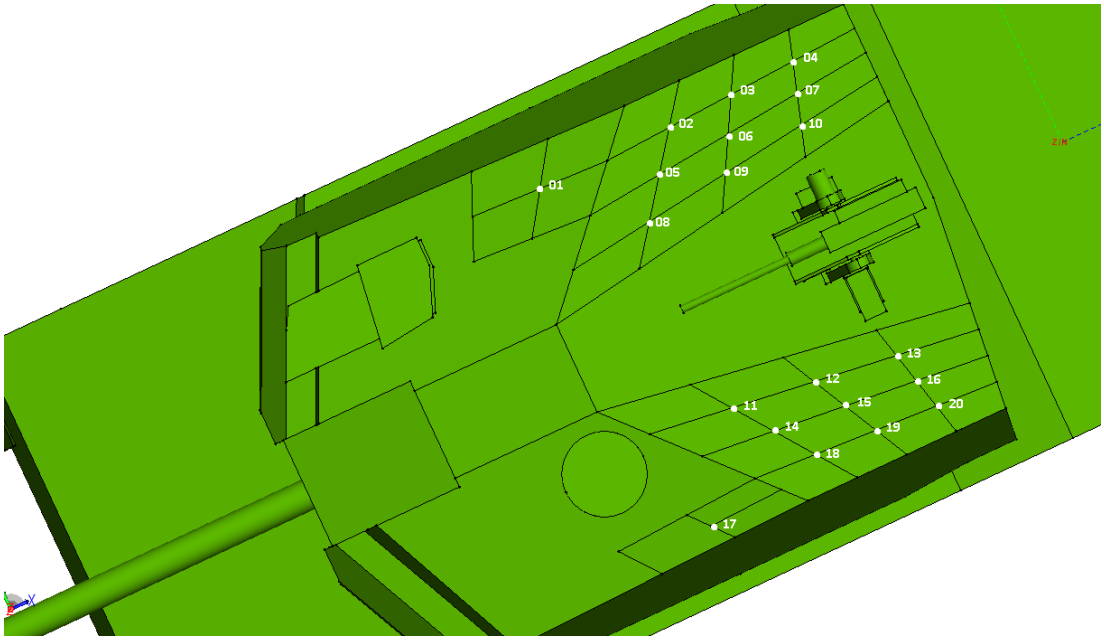

Figure 3.45: Numbered optimization grid points for wider band coupling optimization analyses for antenna placement around rear part of the tank tower.

The first set of the analyses have been done with FEKO using Physical Optics Method decoupled with Method of Moments. This way FEKO uses Physical Optics Method to simulate wave reflections but to simulate the antennas, it uses Method of Moments. As it has been discussed in several sections of Chapter 2, Physical Optics Method is not reliable enough to investigate detailed reflection behavior and one might suspect the results obtained this way. Considering the experience both with Method of Moments and Physical Optics Method, because of the lowness of required computational resources and shortness of simulations times when working with large objects, Physical Optics Method decoupled with Method of Moments was our first choice for wide-band mutual coupling simulations.

Also the second set of the analyses have been done with FEKO, but this time Multilevel Fast Multipole Method (MLFMM) has been used (instead of Method of Moments or Physical Optics Method decoupled with Method of Moments) as recommended at [14]. With MLFMM simulations take longer than Physical Optics Method decoupled with Method of Moments, but considering the advice of the software developer and experience from radar cross section analyses it might be said that it provides more reliable results. In Figure 3.46 results from both set of the simulations can be seen for $(20, 05)$ placement pair.

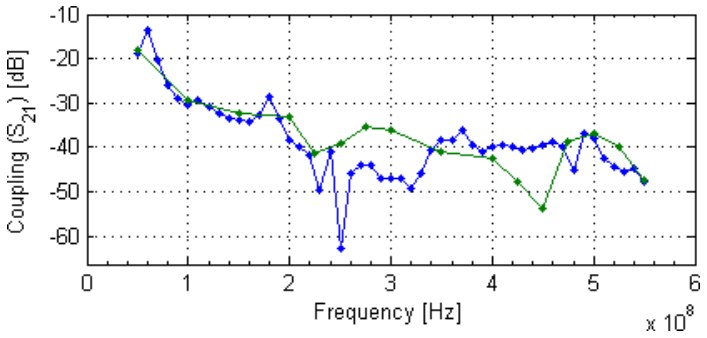

Figure 3.46: Coupling (S_{21}) levels for two COMROD VHF30512CEF antennas placed on $(20, 05)$ placement pair. Green and blue lines represent results obtained using MLFMM and PO decoupled with MoM, respectively.

The third set of analyses have been done with CST MWS to compare with the results before and determine which method was provided more reliable results. Also, because CST MWS uses a very faster solver using Finite Integration Technique (FIT) and makes it possible to obtain results with very higher frequency resolution with help of its adaptive mesher, CST MWS has been used for the rest of the simulations. In Figure 3.47 results from FEKO using Physical Optics decoupled with Method of Moments and Multilevel Fast Multipole Method and CST MWS using FIT can be seen.

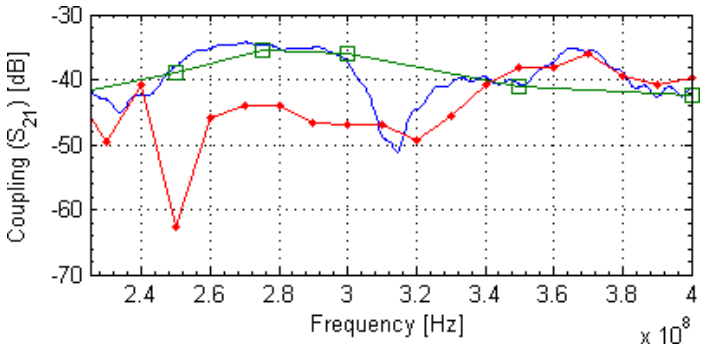

Figure 3.47: Coupling (S_{21}) levels for two COMROD VHF30512CEF antennas placed on $(20, 05)$ placement pair. Green, red, and blue lines represent results obtained using MLFMM, PO decoupled with MoM, and FIT, respectively.

Comparing the results in Figure 3.47, even with this low frequency resolution of MLFMM results from FEKO, they overlap quite perfectly with FIT results from CST MWS. With this comparison it was verified that MLFMM implementation of FEKO is preferable for mutual antenna coupling simulations on large objects. But MLFMM implementation of FEKO is still very slow and FIT implementation of CST MWS is a better choice thanks to its adaptive mesher.

Lastly with this two-way verification, we have decided to use CST MWS for the antenna placement simulations on the rear of the tank tower. The optimization grid introduced in Figure 3.45 indicates the selected locations to antenna placement. To cover most of the grid we placed antennas at there points on the left side of the grid

(points 20, 16, and 13) and moved through all points (points 01 to 10) on the right side. Considering the symmetry of the tank with a coarse look and the reciprocity of the antennas, these thirty pairs of placement is enough to decide if it is necessary to move on simulations further or not. In Figure 3.48 minimum, maximum, and average values of mutual coupling between the antennas placed on the placement pairs selected can be found.

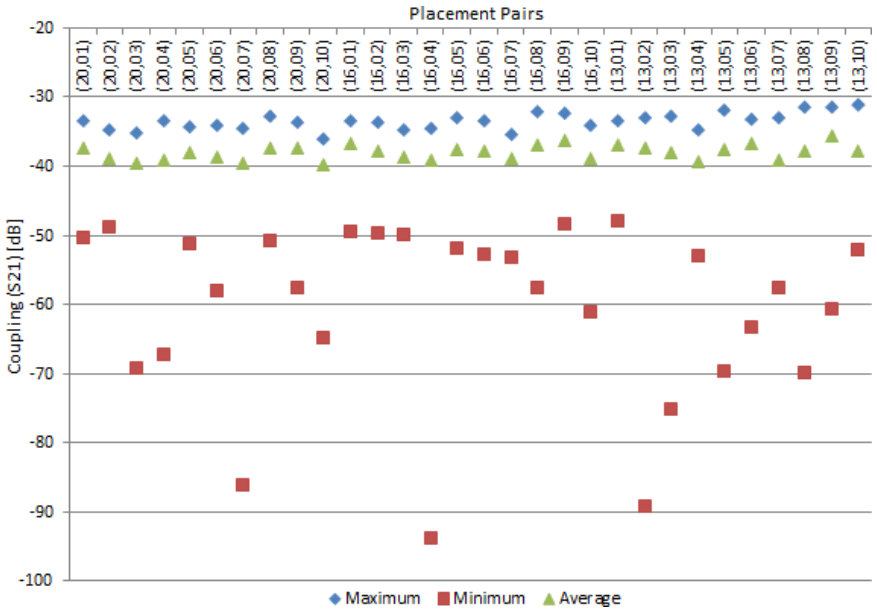

Figure 3.48: Minimum, maximum, and average values of coupling (S_{21}) levels in the frequency range of interest for two COMROD VHF30512CEF antennas placed on several placement pairs from the optimization grid at Figure 3.45. It is important to note that the average values are the averages of linear values of coupling in the frequency range of interest.

For the results at Figure 3.48, it is important to note that the average values are calculated for linear values of coupling levels between 225 to 400MHz. Using values in logarithmic unit would be misleading. In Figure 3.49, coupling levels for some of the placement pairs providing the lowest values at some frequencies can be found. But these local minima do not effect the overall results.

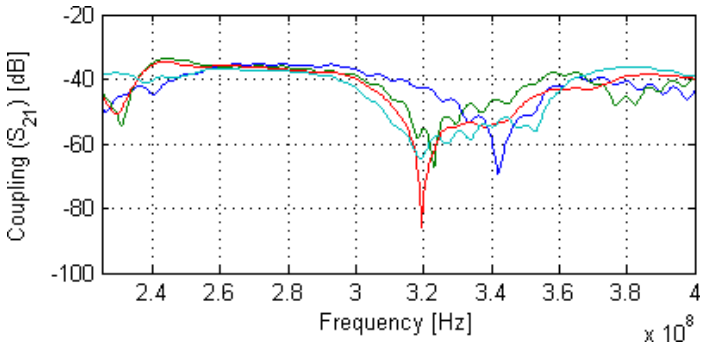

Figure 3.49: Coupling (S_{21}) levels for two COMROD VHF30512CEF antennas placed on $(20, 03)$ (dark blue lines), $(20, 04)$ (green lines), $(20, 07)$ (red lines), and $(20, 10)$ (light blue lines) placement pairs.

The lowest average value obtained from these placement pairs is at (20,10) and the highest one is at (13,09). But the difference between them is about $5dB$ and considering the mechanical ease, sticking with the first placement scenario (20,04) would be the most feasible state.

Chapter 4

Radiation Hazard Analysis

The hazards of electromagnetic radiation to fuels, electronic devices, ordnance, and personnel are described as Radiation Hazard (RADHAZ). For military applications radiation hazards are specified as:

- Hazards of Electromagnetic Radiation to Personnel (HERP)
- Hazards of Electromagnetic Radiation to Ordnance (HERO)
- Hazards of Electromagnetic Radiation to Fuel (HERF)

The subjection of a person to electric, magnetic, or electromagnetic fields or to contact currents other than those originating from physiological processes in the body and other natural phenomena is called exposure [2]. And exposure that results when radio-frequency fields are substantially nonuniform over the body is called partial-body exposure. Fields that are nonuniform over volumes comparable to the human body may occur due to highly directional sources, re-radiating sources, or in the near field region of a radiating structure. The root-mean-square and peak electric and magnetic field strengths, their squares, or the plane-wave equivalent power densities associated with these fields and the induced and contact currents to which a person

may be exposed without harmful effect and with an acceptable safety factor are called Maximum Permissible Exposure (MPE).

MPE is classified according to environments such as controlled or uncontrolled. Location where there is exposure that may be incurred by persons who are aware of the potential for the exposure is called controlled environment. But in our case we will be interested in MPE levels at uncontrolled environments which are locations where there is the exposure of individuals who have no knowledge or control of their exposure. The MPE limits for uncontrolled environments can be seen in Table 4.1.

Table 4.1: Maximum permissible exposure for uncontrolled environments from [2]. f is the frequency in MHz.

Frequency range (MHz)	Electric field strength (E) (V/m)	Magnetic field strength (H) (A/m)	Power Density (S) (mW/m^2)
$0.003 - 0.1$	614	163	
$0.1 - 1.34$	614	$16.3/f$	
$1.34 - 3.0$	$823.8/f$	$16.3/f$	
$3.0 - 30$	$823.8/f$	$16.3/f$	
$30 - 100$	27.5	$158.3/f^{1.668}$	
$100 - 300$	27.5	0.0729	2000
$300 - 3000$			$f/0.15$
$3000 - 15000$			$f/0.15$
$15000 - 300000$			10^5

In this chapter the antenna couple investigated in Chapter 3 will be examined for exposure levels at specific points of the tank geometry.

4.1. Near-Field Analysis for the Antennas Placed on the Tank

In this section Hazards of Electromagnetic Radiation to Personnel (HERP) originating from two COMROD VHF30512CEF antennas placed on the rear corners of the tank tower will be investigated. In Chapter 3 the antenna couple have already been investigated for antenna parameters and a placement scenario has been offered. In this section based on this scenario, near-field region electric and magnetic field strengths and power density will be calculated for the antenna couple placed on the rear part of the tower of the base tank model (see Section 2.5.1 for tank models) using FEKO.

Until this chapter in all analyses using the tank models, all faces of the tank have been assumed to be perfect electric conductor. However, in this section the faces of the tank model will be assumed to be stainless steel (with an electrical conductivity $\sigma = 1.45 \times 10^6 (\mho/m)$ from [24]) with a $5cm$ of thickness to obtain more realistic results via allowing electromagnetic waves propagate inside.

4.1.1. Critical Locations for HERP

At the base tank model, there are two hatches allowing vehicle personnel to open and step outside, see Figure 4.1. These are the only apertures which may allow any electromagnetic radiation to propagate inside the tank body directly when they are open.

There are three location in the tank model where the tank personnel may stand: two person under the hatches and one person under the periscope. Considering hazards of electromagnetic radiation to personnel will be investigated in this section, these three locations were selected to examine.

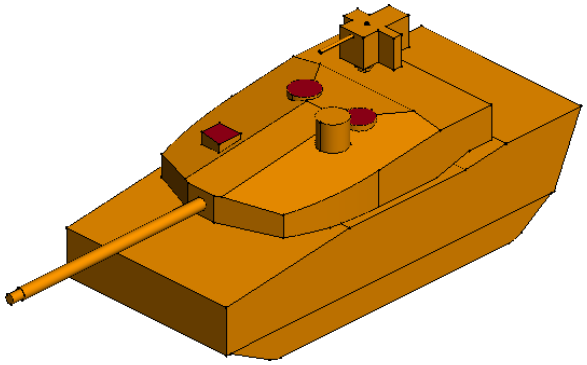

Figure 4.1: The base model of the tank which will be used in this chapter for analyses indicating the hatches and the periscope.

4.1.2. Power Density Levels at the Critical Locations

The MPE limits for uncontrolled environments which was given in 4.1 are determined as power density values for the frequency ranges which the antennas operate. As it has been done in Section 3.3.1, in this section power densities will be calculated for 225, 300, and $400MHz$ operation frequencies.

In this section, the worst case scenario will be tried to be examined to inspect if the power density level are below the limits or not. For frequencies 225, 300, and $400MHz$ the limits are 2000, 2000, and $2666,\bar{6}mW/m^2$, respectively.

To simulate the worst case scenario the antennas had been simulated separately working with the highest feeding power which is $50W$ for the antennas of interest when hatches were open and then superposition of the values were calculated. The simulations have been done for all over the tank model, in Figure 4.2 the regions including the critical locations can be seen.

To represent the exposure at critical locations, in Figures 4.3 to 4.8, cross-section views of the tank model indicating the regions which contains critical locations were given and power density levels at nearly $50cm$ below the hatches were plotted.

The results in Figures 4.4, 4.6, and 4.8 point out that inside the tank tower power density levels are below the MPE limits. Considering these values have been

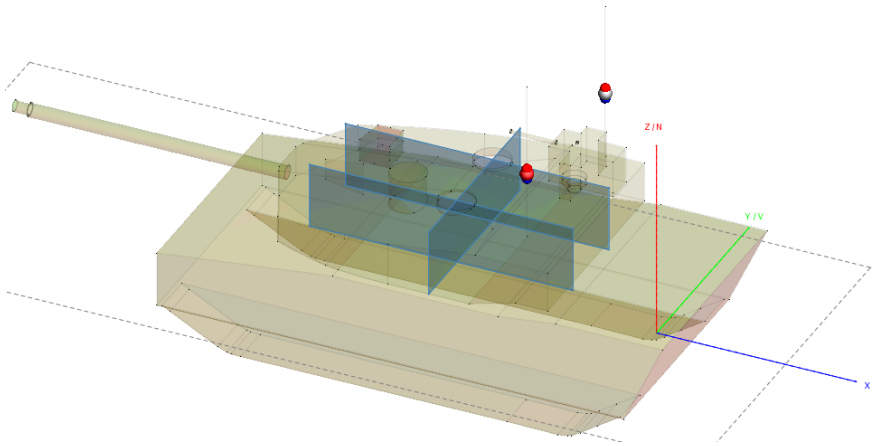

Figure 4.2: The base model of the tank indicating the regions which cover critical locations for HERP.

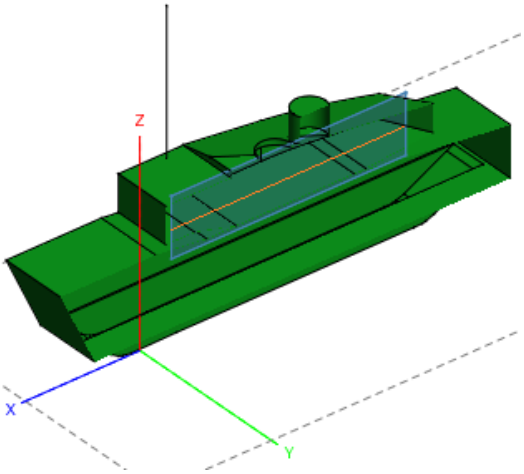

Figure 4.3: Cross-section view of the tank model representing the region below the left hatch at where the near-field region power density levels plotted in Figure 4.4. Orange line represents the coordinates which the results obtained for.

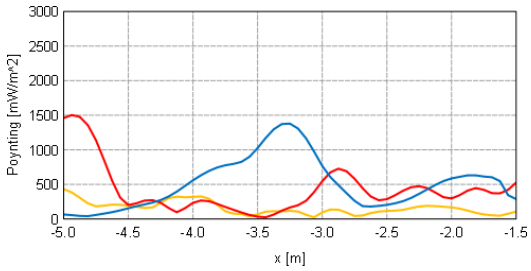

Figure 4.4: Power density levels inside the tower of the tank, $50cm$ below the hatch on the left, along $-x$ axis. Blue, red, and yellow lines represent 225, 300, and $400MHz$ operation frequencies, respectively.

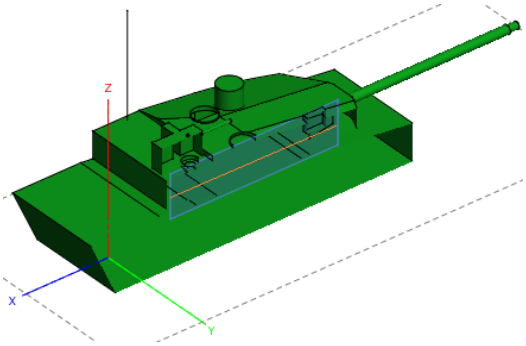

Figure 4.5: Cross-section view of the tank model representing the region below the right hatch at where the near-field region power density levels plotted in Figure 4.6. Orange line represents the coordinates which the results obtained for.

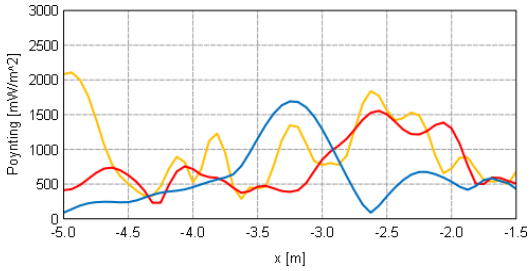

Figure 4.6: Power density levels inside the tower of the tank, $50cm$ below the hatch on the right, along $-x$ axis. Blue, red, and yellow lines represent 225, 300, and $400MHz$ operation frequencies, respectively.

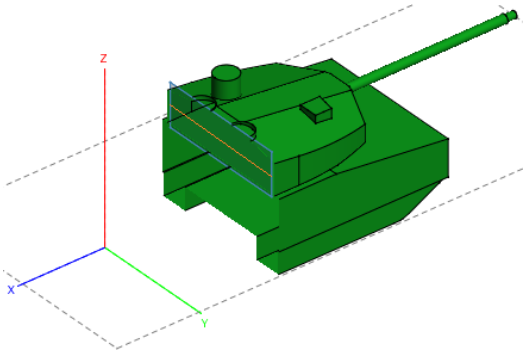

Figure 4.7: Cross-section view of the tank model representing the region below both hatches at where the near-field region power density levels plotted in Figure 4.8. Orange line represents the coordinates which the results obtained for.

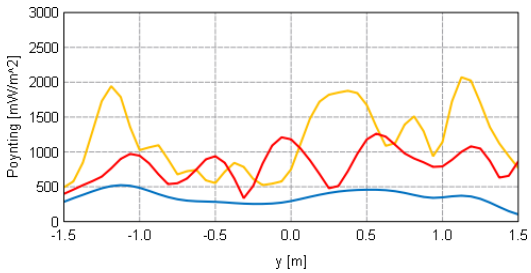

Figure 4.8: Power density levels inside the tower of the tank, $50cm$ below both of the hatches, along $-y$ axis. Blue, red, and yellow lines represent 225, 300, and $400MHz$ operation frequencies, respectively

calculated for the worst case scenario and for only $50cm$ below the hatches, it is not expected to obtain higher exposure levels inside the tank body. Therefore, no further analyses for HERP has been done, according to [2] the tank with two antennas is safe for the personnel operating it.

Chapter 5

Conclusion

The aim of this study was to develop an efficient, accurate and practical framework for electromagnetic analysis of large platforms. Radar cross section (RCS), antenna patterns, mutual coupling and radiation hazard were the topics of interest. There were mainly two approaches to tackle for such a complex problem:

- a rigorous approach - developing a custom made simulator that would answer all of the above questions;
- a practical approach - using currently available commercial simulators on a cluster environment.

In this work, we started with the latter approach and got acquainted with currently the most popular EM based simulators, EMSS-SA FEKO, Ansoft HFSS, and CST MWS. Then, depending upon the geometry and requirements of the system, a hybrid approach was developed, combining these commercial software.

In the first phase of this study, the concept of Radar Cross Section has been studied by analyzing several canonical geometries and two vessels. For RCS simulations, EMSS-SA FEKO has been used and solution methods that FEKO involves have been verified for their integrity. Followed by this initial study, RCS simulations of a tank as a large platform, for a frequency range involving radar frequency bands up to K_a

band have been performed by using the implementation of the Physical Optics (PO) Method by FEKO. In order to perform simulations at different frequency ranges a realistic model and two simplified models of the tank have been analyzed for their RCS behavior.

Moreover, some approaches to reduce RCS of large platforms have been investigated and applied to the tank. Making modifications on the tank geometry and coating the surfaces causing excessive reflection with radar absorber materials were the methods investigated for their advantages and trade-offs.

After RCS analysis, a linear antenna has been modeled with simulation software EMSS-SA FEKO, ANSYS Inc. HFSS, and CST MWS. The antenna model has been analyzed with Method of Moments (MoM), Multilevel Fast Multipole Method (MLFMM), and Finite Integration Technique (FIT) for antenna parameters. The integrity of these methods has been investigated and the reliability of these methods on different antenna parameter simulations has been compared. Lastly, after examining several placement options for a pair of the antenna of interest, an optimum placement scenario has been offered.

In the last phase of this study, the concept of Radiation Hazard (RADHAZ) has been investigated. Radiation Hazard has been introduced for military specifications. The tank with antennas had been investigated for Hazards of Electromagnetic Radiation to Personnel (HERP) and it has been observed that the tank with antennas was safe for the personnel would operate it.

With all these analyses, an efficient, accurate and practical framework for electromagnetic analysis of large platforms has been developed, essential experience on simulations software of interest has been gained and a resource for future large platform simulations has been created.

Bibliography

[1] "Ieee standard radar definitions," *IEEE Std 686-2008 (Revision of IEEE Std 686-1997)*, pp. c1 –41, 21 2008.

[2] *IEEE standard for safety levels with respect to human exposure to radio frequency electromagnetic fields, 3kHz to 300 GHz*, Institute of Electrical and Electronics Engineers, New York, N.Y, 2006.

[3] Brian Woods, "Rf radiation hazard and antenna placement analysis on electrically large military platforms,," *Technical Feature, FEKO,The Annual RF & Microwave Solutions Update*, pp. 28–38, 2011.

[4] C. Uluisik, G. Cakir, M. Cakir, and L. Sevgi, "Radar cross section (rcs) modeling and simulation, part 1: a tutorial review of definitions, strategies, and canonical examples," *Antennas and Propagation Magazine, IEEE*, vol. 50, no. 1, pp. 115 –126, feb. 2008.

[5] S.K. Podilchak, H. Leong, R. Solomon, and Y. Antar, "Radar cross-section modeling of marine vessels in practical oceanic environments for high-frequency surface-wave radar," in *Radar Conference, 2009 IEEE*, may 2009, pp. 1 –6.

[6] J.C. Bennett, B. Chambers, and G.E. Crossley, "Microwave four parameter material characterisation and its application in the design of wideband radar absorbers," in *Low Profile Absorbers and Scatterers, IEE Colloquium on*, may 1992, pp. 4/1 –4/4.

[7] C.A. Balanis, *Antenna theory: analysis and design/Constantine A. Balanis*, J. Wiley, New York, 1982.

[8] Comrod Communication ASA, *VHF30512CEF VHF/UHF Broadband Antenna Datasheet*.

[9] A.A. Smith, *Radio Frequency Principles & Applications*, Universities Press, 1998.

[10] Merrill I. Skolnik, *Introduction to Radar Systems*, McGraw-Hill, 1981.

[11] R. Gente, C. Jansen, R. Geise, O. Peters, M. Gente, N. Krumbholz, C. Moller, S. Busch, and M. Koch, "Scaled bistatic radar cross section measurements of aircraft with a fiber-coupled thz time-domain spectrometer," *Terahertz Science and Technology, IEEE Transactions on*, vol. 2, no. 4, pp. 424–431, 2012.

[12] L.L. Williams, "Physical optics theory of radar cross section," Konfluence Research Institute, January 1999.

[13] E.F. Knott, *Radar cross section measurements*, SciTech Publishing, 2006.

[14] EM Software & Systems-S.A. (Pty) Ltd, 32 Techno Avenue, Technopark, Stellenbosch, 7600, South Africa, *FEKO Examples Guide*, suite 6.0 edition, September 2010.

[15] EM Software & Systems-S.A. (Pty) Ltd, 32 Techno Avenue, Technopark, Stellenbosch, 7600, South Africa, *FEKO User Manual*, suite 6.0 edition, September 2010.

[16] A.C. Woo, H.T.G. Wang, M.J. Schuh, and M.L. Sanders, "Em programmer's notebook-benchmark plate radar targets for the validation of computational electromagnetics programs," *Antennas and Propagation Magazine, IEEE*, vol. 34, no. 6, pp. 52–56, 1992.

[17] Wikipedia, "Ccgs teleost — Wikipedia, the free encyclopedia," 2012, [Online; accessed 22-November-2012].

[18] Noyan Kinayman and M. I. Aksun, *Modern Microwave Circuits (Artech House Microwave Library)*, Artech House, 2005.

[19] D. Bağdat, "Büyük platformlarda anten analiz ve tasarım yöntemleri geliştirme projesi, case study 2," Inside Report of RMK Marine Gemi Yapım Sanayii ve Deniz Taşımacılığı İşletmesi A.Ş., October 2011.

[20] Emerson & Cuming Microwave Products, *Tech Notes: Theory and Application of EF/Microwave Absorbers.*

[21] İ. Türer, "Uhf/vhf haberleşme anten analizi ön çalişma raporu," Inside Report of OTOKAR AŞ, October 2011.

[22] V. Plicanic, "Antenna diversity studies and evaluation," *Master of Science Thesis, Lund University*, 2004.

[23] J. Van der Merwe, *The effect of mutual coupling on the noise performance of large antenna arrays*, Ph.D. thesis, Stellenbosch: University of Stellenbosch, 2010.

[24] D.R. Lide, *CRC handbook of chemistry and physics*, CRC press, 2012.

Vita

İHSAN OZAN YILDIRIM was born in Isparta, Turkey on May 26, 1988. He received his B.Sc. degree in Electronics and Communication Engineering from Yıldız Technical University, İstanbul, Turkey, in 2010. He is currently a M.Sc. student funded by OTOKAR A.Ş. Project, and working towards the M.Sc. degree in Electrical and Electronics Engineering at Koç University, İstanbul, Turkey, as a teaching and research assistant. His research interests include numerical methods for electromagnetics, antenna design, and radar applications.